ENERGY SPECTRA OF INTERACTING QUANTIZED VORTEX CONFIGURATIONS

Adrián Manuel Parrado Almoguera

Thesis submitted to the University of Strathclyde for the degree of Doctor of Philosophy

Department of Chemical & Process Engineering

2024

Declaration

This thesis is the result of the author's original research. It has been composed by the author and has not been previously submitted for examination which has led to the award of a degree.

Signed: Adrián Manuel Parrado Almoguera

Date: 02/08/24

Acknowledgments

I would like to express my deepest gratitude to supervisor, Demosthenes Kivotides for his inestimable guidance through the entirety of my research, being available every time I needed help and for trusting me for this PhD position. Thank you for your encouragement and advice, especially in the hardest moments. I also want to express my appreciation towards my second supervisor, Tim Colonius, for introducing me to many researchers and for his guidance especially at the early stages of my PhD, regardless of the vast distance between us. Their experience has been imperative for the completion of this thesis.

I am also grateful for the invaluable help given by Ke Yu and Benedikt Dorschner to get me kickstarted at the beginning of the program and for the many meetings shuffling vastly different time-zones.

I am also thankful for the help from Lorena Barba when discussing possible accelerations for my methods; without this I would have been in a difficult situation.

I would like to appreciate the feedback from Anthony Leonard regarding my results, it encouraged me to continue forwards.

On a personal note, I would like to thank my father, a mathematician that has not lost all his qualities yet (in some aspects maybe even improved), my mother, the best nurse in the world, and my family for their unconditional love and support and for always believing in me.

I would like to deeply thank my girlfriend, Jennifer, for supporting and sticking with me through my entire degree, master's and PhD. I am sure that you will do great and complete your PhD.

Lastly, I would like to acknowledge my friends Tristan, Sam, Jennifer and Jennifer No. 2 for their support and the late night conversations discussing the concerns with my research.

Abstract

By means of parallel numerical computations, I investigate the energy spectra of Kelvin wave cascade and fully developed turbulence in Schrödinger fluids. I examine the generation and dynamics of Kelvin waves generated by a single reconnection and the associated cascade of energy to smaller scales. The corresponding energy spectrum of the Kelvin wave cascade is found to have a k^{-1} scaling. By following the evolution over large times, I see evidence of statistical equilibration and tendency towards a k^2 spectrum. In the case of fully developed Schrödinger turbulence involving many reconnections and many vortex filaments, I find that the Kelvin wave cascade has a k^{-1} spectrum associated with it, although it is observed over a shorter time. Again, letting the tangle evolve over a large time, I see evidence of a tendency towards a k^2 spectrum due to energy equilibration through interactions between Kelvin waves. By employing a bundle of quantized vortices as a discrete model of Navier-Stokes vortices, I investigate the physics of vortex stretching in classical turbulence. Two configurations were attempted: a Hopf link, where I found that the counter-rotating bundles develop a sinusoidal instability that generates tight secondary structures; the corresponding energy spectra of these secondary structures shows a $k^{-5/3}$ scaling. I also tried a vortex collider configuration where it was found that due to self-stretching and without any reconnections, the energy spectra shows a $k^{-5/3}$ scaling.

Table of Contents

List of Figures

Table of Symbols

Symbol	Description
t	time
k	Wavenumber
$\hbar$	Reduced Planck's Constant
m	Mass of Particle
A	Amplitude of Wavefunction
S	Phase of Wavefunction
W	Ordinary Potential
∇^2	Laplace Operator
Ψ	Wavefunction
g	Interaction Strength
a_s	Scattering Length
$\mathbf{v}$	Velocity (Madelung's Transform)
ρ	Density (Madelung's Transform)
κ	Quantum of Circulation
$\boldsymbol{u}$	Velocity Field
$\boldsymbol{\omega}$	Vorticity
Γ	Circulation
a	Quantized Vortex Core Thickness
$\boldsymbol{X}_s$	Quantized Vortex Tangle Position
ξ_s	Position Along Vortex Tangle
$\boldsymbol{V}_s$	Quantized Vortex Velocity
h_1	Mutual Friction Coefficient
h_2	Mutual Friction Coefficient
$\boldsymbol{V}_n$	Normal Fluid Velocity
$\boldsymbol{X}_s'$	Unit Tangent Vector of Quantized Vortex

$\boldsymbol{x}$	Target Point Position on Vortex Tangle
V_{sv}	Quantized Vortex Ring Velocity
R	Quantized Vortex Ring Radius
ν	Kinematic Viscosity
T_s	Pistol Gun Stroke Time
R'	Effective Radius
b	Propagation Axis Offset
$F(\gamma)$	Functional of the Tangle Before Reconnection
$F(\eta)$	Functional of the Tangle After Reconnection
L	Tangle Length
$F(\eta, \gamma)$	Velocity Field Difference Before and After Reconnection
δ	Difference in Velocity Field
λ	Kelvin Wave Wavelength
$V_{wave}(\lambda)$	Velocity of a Kelvin Wave with a Given Wavelength
σ	Numerical Core Size
$E(k)$	Energy at a Given Wavenumber
l	Vortex Cylinder Length in Chorin's Vortex Stretching
r	Vortex Cylinder Radius in Chorin's Vortex Stretching
ε	Enstrophy
α	Stretching Factor in Chorin's Vortex Stretching
Re	Reynolds Number
T	Fluid Temperature
$\boldsymbol{X}^i$	Position of Point i Along Vortex Tangle
$\boldsymbol{X}^{i-1}$	Position of Previous Neighbour Point of i Along Vortex Tangle
$\boldsymbol{X}^{i+1}$	Position of Next Neighbour Point of i Along Vortex Tangle

δ_v	Inter-Vortex Distance
Δx_{sv}	Discretisation Length in Reconnection Model
α	Allowed Variation in Spacing Between Neighbouring Points
L	Total Tangle Length
V_{sys}	System Volume in Reconnection Model
Λ	Vortex Line Density
β	Reconnection Gauge
$Q(\rho)$	Smoothing Kernel
$svds$	Derivative of the Curve with Respect to Arc Lenth
$svdds$	Second Derivative of the Curve with Respect to Arc Lenth
C	Curvature
y_{n+1}	Future Position in Runge-Kutta Scheme
y_n	Current Position in Runge-Kutta Scheme
dt	Time Step in General Runge-Kutta Scheme
b_1	Runge-Kutta Scheme Coefficient
v_i	Velocity in General Runge-Kutta Scheme
N	Number of Particles
p_{norm}	Summation of Velocities in Every Direction
p_{diff}	Summation of Difference in Velocity Between Parallel and Serial
L_{box}	Box Size in Results
σ_{diag}	Diagnostic Core Size
ξ	Discretisation Length in Results
t_c	Characteristic Time
V_{bundle}	Vortex Bundle Velocity
$N_v(n)$	Vortices Per Layer for a Given Layer n in a Vortex Bundle

r_c	Distance Between Vortex Rings in a Vortex Bundle
D_C	Vortex Bundle Core Diameter
D_B	Vortex Bundle Diameter
r_D	Vortex Bundle Core Diameter to Vortex Bundle Diameter Ratio
t_{small}	Small Time Scale
t_{large}	Large Time Scale

1. Introduction

Turbulence is the manifestation of chaos within fluid flows, characterised by fluctuations in pressure and velocity, and the natural state of fluids. Therefore, its mathematical description is complex [1], making it extremely expensive to numerically compute the dynamics of such systems. It can also be described as a non-linear phenomenon that is characterised by its unpredictable behaviour (chaos) and the irregular patterns that arise within the fluid at different length scales simultaneously [2]. There are different types of turbulence for different types of fluids: Incompressible, compressible, polymeric and magnetohydrodynamic fluids; within the family of turbulence problems, this thesis is very much related to turbulence in Schrödinger fluids, which has repercussions on incompressible Navier-Stokes turbulence. Even though turbulence is chaos, it is dominated by vortical structures [3–5]. As vortices are so important, this work is going to study the role of vortex physics in turbulence. Turbulence occurs both in nature and in engineering applications daily [6], this is true especially for Navier-Stokes turbulence, which has been studied for a century; a form of it can be seen by smokers when they produce smoke rings by pushing air and smoke through their mouths forming a circular opening. This is also often a matter of study, so there are plenty of vortex rings that are generated in laboratories during experiments or modelled during numerical simulations. It is amazing, though, when vortex rings appear in nature without the intervention of human beings. This is exactly what happened with Mount Etna several times in history, most recently being on the years 2000 [7], 2013 and 2024 [8–10].

Fig. 1 - Two smoke rings above Mount Etna. Image taken from [11].

It is quite remarkable that such perfect rings, like the ones depicted in Fig. 1, can happen in nature, as it has nothing to do with the environment found in a laboratory where all variables are controlled to a very high level of accuracy.

In the case of Navier-Stokes fluids, the role of vortices in turbulence has been the topic of many publications [3,12–14]. Vortices also appear in Schrödinger fluids; here the fluid is inviscid and therefore flows without dissipation, and vortices are topological defects of quantized circulation where the vorticity comes in closed loops. At the T=0 limit, where the fraction of classical fluid is negligible, the dissipation of turbulence is dominated by the emission of phonons [15] (even though Schrödinger fluids are inviscid); this decay in superfluid Helium-4 homogeneous turbulence was first measured by Walmsley et al. in [16]. There are not as many works for turbulence in Schrödinger fluids, therefore there is a need to understand better the role of vorticity in Schrödinger fluids. My main topic is investigating the energy dynamics in turbulence in Schrödinger fluids. The second part of my thesis, however, is going to have serious impact on the problem of Navier-Stokes turbulence (incompressible fluid turbulence). It is important to understand this type of turbulence practically, not only foundationally; this is because the Schrödinger fluids studied in this thesis are one of the constituents of superfluids. Superfluids appear in real life in the form of quantum fluids, which at macroscopic scales are a two-component system where a superfluid (which is described by the non-linear Schrödinger equation) interacts with a classical fluid (which is described by the Navier-Stokes equation).

Another reason to study these types of fluids is for their use in cryogenics, especially their use as a coolant for superconducting magnets [17], used for example in the CERN Large Hadron Collider. Seyfert and Claudet in [17] review the use of superfluid helium as a coolant for superconducting magnets, both as a stationary fluid and as a flow, as well as the design principles of a system using superfluid helium as a coolant. Here they conclude that superfluid helium is an excellent coolant that enhances the superconducting properties of the superconducting magnet as well as their stability.

It is also important to understand superfluids because they can be found in the interior of neutron stars [18–21], this was first pointed out by Migdal in [22] and later Anderson and Itoh in [23] gave evidence that there is indeed superfluid neutrons in the outer layer of neutron stars; this can happen at temperature of around 10^7K. Baym et al. in [18] discuss the features of superfluidity states pointed out by Migdal [22] and if they have any influence on the

neutron star. They mention that due to strong forces, proton superconductivity and neutron superfluidity is possible, which could mean that due to the Meissner effect, which is the exclusion of a magnetic field from a superconductor, [24], the superconductive protons would have a great influence on the magnetic properties of neutron stars. Baym et al. later say that this is not the case because the characteristic time for the Meissner effect to take place is *comparable with the age of the universe*.

Haskell and Sedrakian in [19] mention that due to the neutron superfluidity in a neutron star, it changes its dynamics because, for example, superfluid neutrons can flow in the direction normal to the stars outer layer with no viscosity. What is most interesting is that they mention the appearance of quantized vortices with quantized circulation in the neutron condensate.

This thesis is sectioned in different chapters: there is a background research chapter regarding the physics involved with turbulence, vortex dynamics, vortex filaments, quantized vortices, quantized vortices and energy spectra and other work related to vortex stretching and vortex bundling; then there is a section where I explain the physical model used and then a section where the algorithms and numerical methods used to compute the evolution of the vortices and energy spectra are discussed. After this, I display the results of four different quantized vortex configurations: isolated vortices, chaotic tangle, and two vortex bundle configurations (vortex collider and Hopf link). For the case of quantized vortex bundles, I want to understand their dynamics to stress the similarities and differences with Navier-Stokes turbulence from a fundamental physics point of view, and therefore contribute to the physics of a much less studied part of turbulence. The quantized vortex bundles section focuses on the dynamics of bundles of quantized vortices, which has two possible interpretations; one is to see how bundles of superfluid He-4 vortices would behave (using quantized vortices with physical parameters of superfluid He-4). The other interpretation is to discretise a classical vortex ring into a number of quantized vortex rings, where the total circulation of the discretised classical vortex would be equal to the total circulation of all quantized vortex rings. This configuration is separated into two separate subsections, a vortex collider and a Hopf Link configuration, each of which favours different physics like vortex stretching and secondary vortex structure generation through the Crow instability. For the case of the isolated vortices configuration, as vortex stretching in isolated quantized vortices is not possible, I want to see the effect of Kelvin waves on the dynamics of the quantized vortices, and if there is an equilibration of energy that happens through the continuous interaction of different sized Kelvin waves. The

Kelvin waves are not forced and are generated after the vortices reconnect, through the relaxation of the tangle. I end with a conclusion discussing the results and possible future work.

2. Background

In this section I will discuss the physics that are imperative for the problem of understanding the dynamics of quantized vortices and their respective energy spectra depending on their configuration and their current position in a 3-Dimensional space. I will review Schrödinger Fluids and vortices that describe its turbulence, as well as the Biot-Savart law, Kelvin waves that result from vortex filament reconnections and the energy spectra of a vortex tangle. I will also discuss the methods and findings of several related works.

2.1. Madelung Transform of the Nonlinear Schrödinger Equation

Before reviewing other works, I will show that the Nonlinear Schrödinger equation can describe a fluid. These are called Schrödinger fluids, which are governed by the Madelung's transformation of the Nonlinear Schrödinger equation (NLSE), which is written using hydrodynamical variables. I will briefly go over the derivation of said transformations as explained in [25].

The Nonlinear Schrödinger equation is as follows:

$$-\frac{\hbar^2}{2m}\nabla^2\Psi + \mathrm{W}\Psi + g|\Psi|^2\Psi = \mathrm{i}\,\hbar\frac{\partial\Psi}{\partial t} \tag{1}$$

Start by substituting the wavefunction into the Nonlinear Schrödinger equation:

$$\Psi(\boldsymbol{x},t) = A(\boldsymbol{x},t)\,e^{iS(\boldsymbol{x},t)/\hbar} \tag{2}$$

Where A and S are the amplitude and the phase of the wavefunction respectively, m is the mass of the particle, W is the ordinary potential, g represents the interaction between particles as $g = \frac{4\pi\hbar^2 a_s}{m}$ and $|\Psi|^2 = A^2$.

$$-\frac{\hbar^2}{2m}\nabla^2\left(Ae^{iS/\hbar}\right) + \mathrm{W}\left(Ae^{iS/\hbar}\right) + gA^2\left(Ae^{iS/\hbar}\right) = \mathrm{i}\,\hbar\frac{\partial\left(Ae^{iS/\hbar}\right)}{\partial t} \tag{3}$$

Substitute equivalent expressions for $\frac{\partial\left(Ae^{iS/\hbar}\right)}{\partial t}$, $\nabla^2\left(Ae^{iS/\hbar}\right)$ and $\nabla^2 e^{iS/\hbar}$:

$$\frac{\partial\left(Ae^{iS/\hbar}\right)}{\partial t} = e^{iS/\hbar}\frac{\partial A}{\partial t} + Ae^{iS/\hbar}\frac{i}{\hbar}\frac{\partial S}{\partial t} \tag{4}$$

$$\nabla^2\left(Ae^{iS/\hbar}\right) = A\nabla^2 e^{iS/\hbar} + 2\nabla\mathrm{A}\cdot\nabla e^{iS/\hbar} + e^{iS/\hbar}\nabla^2 A \tag{5}$$

$$\nabla^2 e^{iS/\hbar} = -\frac{1}{\hbar^2}(\nabla\mathrm{S})^2 e^{iS/\hbar} + \frac{i}{\hbar}e^{iS/\hbar}\nabla^2 S \tag{6}$$

After substituting **Equations 4, 5, 6** into **Equation 3** you get the following. I separate **Equation 7** into right-hand side (RHS) and left-hand side (LHS) as the resulting expression is quite long.

$$LHS: -\frac{\hbar}{2m}\left(A\left(-\frac{1}{\hbar^2}(\nabla \mathrm{S})^2 e^{iS/\hbar}+\frac{i}{\hbar}e^{iS/\hbar}\nabla^2 S\right)+2\nabla \mathrm{A}\cdot\frac{i}{\hbar}e^{iS/\hbar}\nabla \mathrm{S}+e^{iS/\hbar}\nabla^2 A\right) + WAe^{iS/\hbar}+gA^2\left(Ae^{iS/\hbar}\right) \quad (7)$$
$$RHS: i\hbar\left(A\frac{i}{\hbar}e^{iS/\hbar}\frac{\partial S}{\partial t}+e^{iS/\hbar}\frac{\partial A}{\partial t}\right)$$

If you look closely at **Equation 7** you can cancel all $e^{iS/\hbar}$ terms:

$$LHS: -\frac{\hbar^2}{2m}\left(A\left(-\frac{1}{\hbar^2}(\nabla \mathrm{S})^2+\frac{i}{\hbar}\nabla^2 S\right)+\frac{i}{\hbar}(2\nabla \mathrm{A}\cdot\nabla \mathrm{S})+\nabla^2 A\right)+WA+gA^2(A) \quad (8)$$
$$RHS: i\hbar\left(A\frac{i}{\hbar}\frac{\partial S}{\partial t}+\frac{\partial A}{\partial t}\right)$$

You can now separate **Equation 8** into its real and imaginary parts [26]. This yields:

$$Re: \frac{1}{2m}(\nabla \mathrm{S})^2 A-\frac{\hbar^2}{2m}\nabla^2 A+WA+gA^2(A)=-A\frac{\partial S}{\partial t} \quad (9)$$

$$Im: \frac{-1}{2m}(A\nabla^2 S+2\nabla \mathrm{A}\cdot\nabla \mathrm{S})=\frac{\partial A}{\partial t} \quad (10)$$

Equation 9 and **10** can be rewritten as the momentum and the continuity equation respectively. To achieve the momentum equation from **Equation 9**, start by dividing **Equation 9** by A:

$$\frac{\partial S}{\partial t}+\frac{1}{2m}(\nabla \mathrm{S})^2-\frac{\hbar^2}{2m}\frac{1}{A}\nabla^2 A+W+gA^2=0 \quad (11)$$

Where $W_Q=-\frac{\hbar^2}{2m}\frac{1}{A}\nabla^2 A$ is the quantum potential [27]. Knowing that $\nabla \mathrm{S}=\mathrm{m}\mathbf{v}(\mathbf{x},\mathrm{t})$, **Equation 11** can be rearranged to:

$$\frac{\partial S}{\partial t}+\frac{m\mathbf{v}^2}{2}-\frac{\hbar^2}{2m}\frac{1}{A}\nabla^2 A+W+gA^2=0 \quad (12)$$

Lastly, to achieve the momentum equation change $A^2=\rho$, take the gradient of **Equation 12** [26]:

$$\nabla\frac{\partial S}{\partial t}+\nabla\left(\frac{m\mathbf{v}^2}{2}\right)+\nabla\left(W+g\rho-\frac{\hbar^2}{2m}\frac{1}{A}\nabla^2 A\right)=0$$
$$\frac{\partial \mathbf{v}}{\partial t}+(\mathbf{v}\cdot\nabla)\mathbf{v}+\frac{1}{m}\nabla\left(W+g\rho-\frac{\hbar^2}{2m}\frac{1}{A}\nabla^2 A\right)=0 \quad (13)$$

Now that the momentum equation has been derived, let's start with **Equation 10** to derive the continuity equation. Start by defining the expression:

$$\nabla \mathrm{A} = \frac{1}{2\sqrt{\rho}} \nabla \rho \tag{14}$$

By substituting **Equation 14** into **Equation 10**:

$$\frac{-1}{2M}\left(\sqrt{\rho}\nabla^2 S + 2\left(\frac{\nabla\rho}{2\sqrt{\rho}}\right)\cdot \nabla \mathrm{S}\right) = \frac{1}{2\sqrt{\rho}}\frac{\partial \rho}{\partial t} \tag{15}$$

Equation 15 can be rearranged to have all terms to one side and then multiply by $\sqrt{\rho}$, this yields:

$$\frac{\partial \rho}{\partial t} + \frac{\left(\rho\nabla^2 S + (\nabla\rho)\cdot(\nabla S)\right)}{m} = 0 \tag{16}$$

Now, exchange the relation $\rho\nabla^2 S + (\nabla\rho)\cdot(\nabla S) = \nabla\cdot(\rho\nabla S)$ into **Equation 16**. This results in the continuity equation:

$$\frac{\partial \rho}{\partial t} + \frac{\nabla\cdot(\rho\nabla S)}{m} = 0 \tag{17}$$

Note that $\nabla \mathrm{S} = \mathrm{m}\mathbf{v}(\mathbf{x}, \mathrm{t})$, therefore **Equation 17** turns into:

$$\frac{\partial \rho}{\partial t} + \nabla\cdot(\rho\mathbf{v}) = 0 \tag{18}$$

2.2. Vortex Dynamics

Here I review classical and quantized vortex dynamics to achieve a certain level of understanding before advancing as it is imperative for fully understanding turbulent flows. Vortex dynamics studies how a rotating or swirling flow evolves when it is majorly governed by inertial rather than by viscous effects [28]. We can think of vortices being frozen in the fluid, which means that the vortices are transported together with the fluid as it flows, just like material curves of fluid particles would, as mentioned by Helmholtz in [29]. The interesting thing is that even if the flow is incompressible, the vortex cores will be stretched as they are transported, which leads to a vorticity intensity increase which is one of the reasons for energy to be passed from larger to smaller scales in a process called energy cascade [30], this will be discussed later in the thesis as it is one of the central themes of discussion.

Now I will discuss further topics regarding vortex dynamics like vorticity, circulation, and their relation as well as vortex dynamics in Schrödinger fluids (quantized vortices) and the Biot-Savart law. I will also explain what vortex filaments are and how they induce velocity.

2.2.1. Vorticity

A velocity field of a fluid, $\boldsymbol{u}$, is described using its position in space, $\boldsymbol{x}$, at a certain time, t, in the following manner: $\boldsymbol{u}(\boldsymbol{x}, t)$, where $\boldsymbol{u}$ is a vector containing all three components of velocity in a Cartesian manner (u, v, w) and $\boldsymbol{x}$ is a vector that denotes position as (x, y, z). Therefore the vorticity $\boldsymbol{\omega}(\boldsymbol{x}, t)$ is the curl of the velocity field $\boldsymbol{u}(\boldsymbol{x}, t)$ [31]:

$$curl(\boldsymbol{u}) = \nabla \times \boldsymbol{u} = \boldsymbol{\omega}(\boldsymbol{x}, t) = \left(\frac{\partial w}{\partial y} - \frac{\partial v}{\partial z}, \frac{\partial u}{\partial z} - \frac{\partial w}{\partial x}, \frac{\partial v}{\partial x} - \frac{\partial u}{\partial y}\right) \tag{19}$$

The vorticity $\boldsymbol{\omega}$ is a vector resulting from the curl of a vector quantity, velocity $\boldsymbol{u}$; $\boldsymbol{\omega}$ is *proportional to the rotation rate of a small fluid element about its own axis* [32], therefore vorticity defines the rotation of the fluid flow [33], which means that a flow with zero vorticity would be referred to as irrotational flow.

2.2.2. Circulation

Circulation is the result of vorticity, and mathematically it can be defined as the line integral of a fluid velocity vector around a closed contour C [32]:

$$\Gamma = \oint_C \boldsymbol{u} \cdot d\boldsymbol{l} \tag{20}$$

Where, $\boldsymbol{u}$ is the fluid velocity vector and $d\boldsymbol{l}$ is a small element on the curve. It is known that both circulation and vorticity are closely related; this relationship is understood applying Stoke's theorem to velocity vector $\mathbf{u}$, which relates the line integral of a vector field, like the one in **Equation 20**, to the surface integral of the curl of the same vector field (in our case, the curl of the vector field is the vorticity) [34]:

$$\Gamma = \oint_C \boldsymbol{u} \cdot d\boldsymbol{l} = \iint_S (\nabla \times \mathbf{u}) \cdot d\boldsymbol{S} = \iint_S \boldsymbol{\omega} \cdot d\boldsymbol{S} \tag{21}$$

The circulation Γ around a closed contour C, and the vorticity $\boldsymbol{\omega}$ bounded by the same contour are related mathematically; this means that if vorticity is zero everywhere within the region enclosed by the closed loop, then, following Stoke's theorem, the circulation would also be zero. For Schrödinger fluids in the vortex dynamics model, the vorticity is a delta function, but the circulation has a finite value κ which is the quantum of circulation.

2.2.3. Vortices in Schrödinger Fluids

Schrödinger fluids, much like superfluids, are fluids that possess a characteristic property, they flow without any viscosity; therefore there is no dissipation of the energy related to its motion into heat [35]. Superfluidity can be achieved only in certain scenarios and under

specific conditions; for example, Helium-3 and Helium-4 can achieve superfluidity at extremely low temperatures, 0.0025K and 2.17K respectively [36]. As mentioned by Sebastien Balibar in [37], *Superfluidity is a manifestation of quantum mechanics at the macroscopic level*, because they gain importance within the several properties of fluids; some manifestations include quantized circulation, zero viscosity and quantized vortices. These manifestations provide the unique properties found in superfluid systems and will be discussed next. The presence of quantized vortices is due to quantized circulation, which as mentioned before, is a property of superfluids. Superfluid vortices have an extremely small finite core size that show properties different to those from classical fluid vortices; we can imagine them as vortex lines as mentioned by Feynman in [38].

Superfluid Helium is conformed by a superfluid and a normal component; Schrödinger fluids can be thought of as the superfluid component without the interactions with the normal component of the fluid.

2.2.4. Vortex Dynamics in Schrödinger Fluids

Quantized vortices are topological defects with quantized circulation whose vorticity can be thought of as a Dirac delta function, due to the quasi-infinitely small size. The extremely small cores of quantized vortices (of Schrödinger fluids) are empty of the fluid, and the fluid rotates around it.

Turbulence in Schrödinger fluids is composed of vortices. Here, when using Helium-4 parameters, vortices are filaments with a thickness $a \approx 1 \times 10^{-8}$ cm of quantized circulation ($\kappa = 9.97 \times 10^{-4}\ \mathrm{cm^2 s^{-1}}$), which is forced by quantum constraint [39]. Say I have a series of vortex filaments positioned in 3-dimensional space tangled together, I can then define said tangles as $\boldsymbol{X}_s(\xi_s, t)$, where ξ_s is the position along the vortex loops and t is time. I can now define the evolution of the vortex loops as it was given by Kivotides in [40,41]:

$$\frac{\partial \boldsymbol{X}_s}{\partial t} = \boldsymbol{V}_s + h_1 \boldsymbol{X}_s' \times (\boldsymbol{V}_n - \boldsymbol{V}_s) + h_2[\boldsymbol{X}_s' \times (\boldsymbol{X}_s' \times \boldsymbol{V}_n) + \boldsymbol{V}_s] \tag{22}$$

Here $\boldsymbol{V}_s$ is the superfluid velocity, $\boldsymbol{V}_n$ is the velocity of the normal or classical fluid, $\boldsymbol{X}_s'$ is the unit tangent vector which tells you the direction of the vorticity and h_1 and h_2 are the mutual friction parameters which tell you how the superfluid and the normal fluid interact, so they are used to couple both fluids. As I am working with Schrödinger fluids, there is no interaction between classical and superfluids, therefore h_1 and h_2 parameters equate to zero and **Equation 22** simplifies to:

$$\frac{\partial \boldsymbol{X}_s}{\partial t} = \boldsymbol{V}_s \tag{23}$$

, where $\boldsymbol{V}_s$ is given by the Biot-Savart integral found in **Equation 24**. After understanding how quantized vortices evolve, it is important to denote the behaviour of the vortex filaments when they approach and are in proximity with each other; what happens in this situation? As suggested by Feynman in [38], if two vortex filaments approach each other, the system becomes unstable and the filaments start to twist around each other; once the distance between the filaments becomes small enough the vortex filaments will 'snap' together which results in a new arrangement in the system. It was also mentioned by Schwarz in [42] that if two vortex filaments cross each other, they would reconnect after deforming themselves at their closest point, this would result in the reconnection points moving apart quickly after it happens. This introduces us to an interesting part of Schrödinger fluid turbulence, this reconnection described previously would give way to the generation of Kelvin waves which I explain in a later section.

2.2.5. Biot-Savart Law and Vortex Filaments

You can think of vortex filaments as an imaginary curve that produces rotation in the fluid around it; the example explained by Gudmundsson in [43] illustrates it simply, imagine the centre of a tornado with flow circulating around it. Vortex filaments have a given strength, which is determined by the circulation, Γ, which describes the ability of a vortex filament to provoke rotation in the flow around it; this circulation is constant along the entire length of the vortex filament.

According to Helmholtz' theorem, a vortex filament can have any shape as long as it either extends to infinity or loops on itself [44]. To understand how the velocity induced by the vortex filament is calculated, imagine an infinitely small vortex segment 'dl' on the vortex filament, as well as a point 'P' anywhere in space. The segment will contribute to the velocity of point 'P', which is denoted by 'V_s'; this velocity can be calculated by computing the Biot-Savart integral shown in **Equation 24** [40]:

$$V_s(\boldsymbol{x}) = -\frac{\kappa}{4\pi}\int_{\mathcal{L}_s} d\xi_s \frac{\boldsymbol{X}_s' \times (\boldsymbol{X}_s - \boldsymbol{x})}{|\boldsymbol{X}_s - \boldsymbol{x}|^3} \tag{24}$$

Here, $V_s(\boldsymbol{x})$ is the superfluid vortex velocity at point $\boldsymbol{x}$, κ is the quantum of circulation, the multiplication $d\xi_s\, \boldsymbol{X}_s'$ is the discretisation distance along the vortex length and $\boldsymbol{X}_s$ and $\boldsymbol{x}$ are the positions of the points along the vortex filament length used as source and target

respectively. Therefore, what is being done is a summation of the contribution of all vortex points to all vortex points.

2.2.6. Quantized Vortex Rings

When talking about turbulence in Schrödinger fluids, it manifests itself in the form of a series of closed-loop filaments (vortex rings) of quantized circulation, the latter being defined as:

$$\kappa = \frac{h}{m} \tag{25}$$

, where κ is the quantum of circulation, h is Planck's constant and m is the mass of a single particle of the fluid. These vortex rings have a core size (a) much smaller than their radius. If we imagine an individual circular vortex ring generated parallel to the YZ-plane and we cut it in half using a plane parallel to the XY-plane, it will look like Fig. 2:

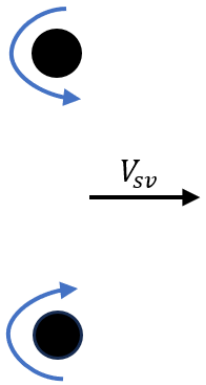

Fig. 2 – Thin slice of a vortex ring showing the vortex core as black circles (exaggerated for clarity). In this case, the vorticity direction of the top slice of the ring is coming out of the paper and the bottom slice of the ring has a vorticity direction going into the paper. This results in the vortex ring propagating to the right.

The direction of rotation of the flow around the filament helps us understand the direction of vorticity and vice versa due to the right-hand rule. The configuration shown in Fig. 2 would result in the vortex ring travelling towards the right due to its self-induced velocity; this propagation velocity V_{sv}, given that the radius R of the ring is much bigger than its core radius a, can be calculated by using the following equation [45]:

$$V_{sv} = \left(\frac{\kappa}{4\pi R}\right)\left[\ln\left(\frac{8R}{a}\right) - \frac{1}{2}\right] \tag{26}$$

, where κ is the quantum of circulation, R is the ring radius and a is the vortex core thickness. This shows that smaller vortex rings propagate faster than larger vortex rings.

As mentioned previously, my work focuses solely on quantized vortex rings, either isolated or bundled; as I work with bundles of quantized vortices in **sections 5.3** and **5.4** and they can be thought of as discretised Navier-Stokes vortices, it is important to note the differences between isolated quantized vortex rings and classical vortex rings in terms of vorticity, core thickness and robustness.

2.2.6.1. Differences Between Classical and Quantized Vortex Rings

To begin, I will note the most obvious difference between quantized vortex rings and classical (Navier-Stokes) vortex rings; this is their vortex core thickness. A quantized vortex ring with superfluid Helium-4 parameters would have a core thickness $a \approx 1.58 \times 10^{-8} cm$ that is kept constant, while a classical vortex could have a range of core sizes as shown in **Table 1** in [46]; here vortices could have a core diameter of several meters when talking about trailing vortices generated by planes or tornadoes, all the way up to several thousand light-years when talking about spiral galaxies. When talking about a classical vortex ring generated in lab conditions using a piston gun submerged in water like in [47], the initial vortex ring core size can be approximated as [45,47]: $a = \sqrt{4\nu T_s}$, where ν is the kinematic viscosity and T_s is the stroke time of the piston gun. They then measured the core size, and compared the predicted and measured core sizes and found that the prediction agrees with the experimental data; also, they found that the core radius was dependent on the stroke time and not on the stroke length of the piston gun. This core radius is dynamic and can change size and deform as it develops, this cannot happen with quantized vortices; this difference can be bridged by grouping quantized vortices into polarised vortex bundles.

In terms of the fluid density at the vortex core, a classical vortex has a finite fluid density while for a quantized vortex filament the vortex core is defined as where the superfluid density goes to zero [48].

In terms of vorticity distribution there is also a difference between classical vortices and the vortex rings that I deal with. Classical vortices can be approximated to have a Gaussian vorticity distribution inside the vortex core, this is common approach which has been used by many people [45,49–51]. Danaila et al. in [52] mention and depict a quasi-Gaussian vorticity distribution; this distribution has also been found experimentally in [53,54]. On the other hand, the vortices that I compute the dynamics for have a core diameter size much smaller than the vortex ring radius ($a \ll R$) and therefore in the macroscopic scale, the vorticity distribution of my quantized vortices is a delta function.

When comparing the two types of vortices in terms of robustness and dissipation, firstly we know that due to the viscosity of classical fluids, vortices in such a fluid would slowly dissipate until they disappear; this can be seen in many beautiful images assembled by Van Dyke in [55]. This viscous dissipation is not present when talking about quantized vortices due to their inviscid nature, but there is an acoustic energy emission every time there is a vortex reconnection; this results in these vortices being much more robust than classical fluid vortices, and therefore survive for much longer.

2.2.7. Vortex Reconnections

Reconnections of quantized vortices is a very important portion of vortex dynamics of Schrödinger fluids, and it studies how two filaments come close together, crossing each other, and break into two parts [56], this results in a change in topology of the vortices. An example of this can be seen in Fig. 3.

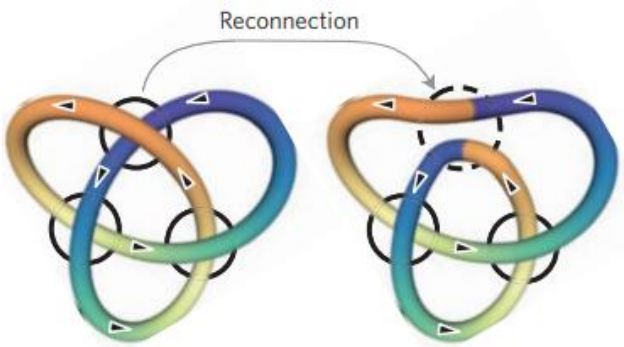

Fig. 3 - Representation of a trefoil vortex reconnection with itself separating into two distinct vortices in a hopf-link-like configuration. Image taken from [57].

Bewley et al. in [58] present the first experimental observation of reconnections between superfluid helium vortices. Reconnections create an area of large curvature that make the newly formed tangles to move in opposite directions (Fig. 4); sometimes even, the curvature could be a generation point for Kelvin waves that then propagate along the tangle length. I talk more about this in **section 2.2.9**.

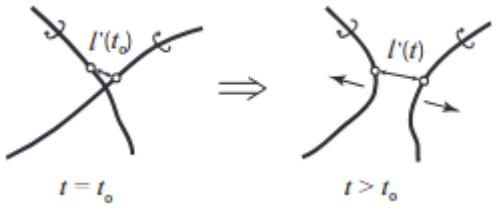

Fig. 4 - Vortex filaments reconnecting at t_0 (left) and the resulting tangle after reconnection (right). The filaments then move in opposite directions distancing themselves. Image taken from [58].

Gregory P. Bewley et al. in [58] say that the distance between two particles after vortex reconnection $l'(t)$ follows the $t^{1/2}$ law; there have been several analysis of vortex reconnections, both theoretical [59] and numerical [57,60] that have confirmed this.

The first to introduce reconnections computationally was Schwarz in [42]. In his paper, Schwarz describes very interesting vortex reconnection scenarios, like vortices reconnecting with a surface and two vortex filaments reconnection with each other; I will focus on the latter as it is directly related to my work. If two vortex rings that counter-rotate (in the same plane) come close to each other, a cusp will develop and then it will be the reconnection point between these two vortices. This reconnection creates a region of high curvature that makes the resulting vortices move away from each other. Schwarz assumes that the reconnection between two vortices happen when the vortex lines come closer than approximately 1 angstrom ($10^{-8}\ cm$). Schwarz says that for vortices to reconnect and not "dodge" around each other, the sections that come in close proximity have to be anti-parallel (counter-rotating). It is possible for near parallel vortex sections to reconnect; this happens because the sections distort and twist around to become locally anti-parallel and finally reconnect, but only the reconnection point twists around. Schwarz also mentions that most scenarios where two vortex lines cross, a reconnection will happen, with its consequent topological change in geometry.

Waele and Aarts in [61] study how two counter rotating vortex rings of ideal fluid deform. They start by setting up two symmetrical ideal fluid vortex rings on the XY plane; these vortices come closer together by developing kinks on portions of the ring closest to the other ring. Waele and Aarts show a zoomed in section of the kink that forms from the vortex interaction and show how the kinks form a symmetrical pyramid shape. They note that the symmetry of the pyramid that is formed does not depend on the initial conditions being symmetrical; asymmetrical initial conditions would still result in kinks forming a symmetrical

pyramid shape. Waele and Aarts denote a distance ‘D’ between the closest point between the vortices, the tip of the kinks, and graphically show that this distance ‘D’ is well defined in space and time and tends to zero (reconnection). They conclude that for many different initial conditions, varying the symmetry of the geometry, the route towards reconnections is universal and that this stays true to the vortex movement after reconnection happens.

Leadbeater et al. in [62] focus on measuring the energy loss in the tangle due to sound emission from vortex reconnection, they also do this in terms of vortex tangle length loss. They calculate the sound energy ejected, and therefore tangle length lost, due to the reconnection of two superfluid vortex rings; this is correct in the Local Induction Approximation (LIA) but is not exact with the description used in this thesis. In their calculations, they use the Gross-Pitaevskii equation to model the dynamics of superfluid vortices. Leadbeater et al. collide two identical vortex rings that travel in opposite directions with an offset on their centre which is varied for several different values of tangle length loss. They carry out simulations for different values of vortex ring radius, which they mentioned is limited by numerics, because too small of a vortex ring radius would be too fast to capture the sound pulse emitted by reconnection, and a vortex ring with a large radius would result in calculating the system for many vortex points. Leadbeater et al. show that for two identical, counter-rotating vortex rings colliding with an offset, the resulting vortex rings have a smaller radius (as well as showing the sound pulse), which suggests that due to the reconnection, there has been a tangle length loss and therefore energy loss. Leadbeater et al. conclude that the energy that is lost due to the reconnection is in the form of tangle length loss and that it depends on the collision angle; the tangle length lost is maximised when the vortex rings are on course for a head-on collision (all segments can be thought to be antiparallel at this point), and they note that this suggests that these reconnections could be an important energy dissipation mechanism for this kind of system. I consider these results when formulating the reconnection algorithm I use.

Zhu et al. in [63] the interaction between two isolated vortex rings that travel in the same direction. They do this by colliding two vortex rings that travel in the same direction, the radius of the vortex rings is varied for different calculations as well as their axis is offset by a variable amount b. Zhu et al. make use of the full Biot-Savart law to consider both local and long-range interactions between the vortices. The rings are discretised into about 100 vortex points and always have a minimum of 6 points (this is important when small rings appear due

to reconnections). Due to the dynamics of the system, neighbouring points in a ring can separate of come closer together, so their algorithm adds or subtracts vortex points to maintain their separation between half and double their original discretisation distance. Their reconnection algorithm also ensures that there is a small length of the vortex lost at every reconnection; this happens when two vortex points come closer than half their original discretisation distance. Zhu et al. also define an effective radius R' as the radius of a perfectly circular vortex ring that has identical impulse as a deformed vortex ring. Their simulations consist of placing two vortices of different radii travelling in the same direction in space (with the smallest ring behind as it moves faster) and offsetting their propagation axis by b. As the smaller vortex catches up it shrinks while the other vortex grows, similar to the behaviour of leapfrogging vortices, and if the values of b is appropriate the vortices would reconnect. Zhu et al. find that there are 3 different critical offset values (b_1, b_2, b_3) that mark different regimes (outcomes): When $b < b_1$, the second ring misses the first ring through the inside completely avoiding reconnection and maintaining their original radius size; the vortices also gain lateral motion. When $b_1 < b < b_2$: The vortices reconnect at two different points, this generates two deformed rings that are increasingly different in terms of their R' as b is increased; the effective radius of the second ring, R_2', tends to 0 as the value of b tends to b_2. When $b_2 < b < b_3$: The rings form one large, deformed rings through one reconnection; this is the maximum possible resulting vortex. If the value of b is close to b_2 the large ring can undergo a self-reconnection. The final regime is when $b > b_3$: Here the rings do not reconnect and dodge each other on the outside, this results in a very small variation of their size, shape and propagation direction. Zhu et al. found that if the initial vortices are very similar in size, the range of b where they reconnect is much smaller; this may seem counterintuitive but is due to the time it takes the second vortex ring to catch up with the first (their relative velocity is very small), this means that the vortices have enough time to interact, which leads them to dodge each other. If they do reconnect, it seems that most end up reconnecting at a single site, generating a single, large, deformed vortex ring. If the original vortices have a large difference in size, the opposite happens. The range of b where the vortices reconnect is larger and does not seem to show any favouring towards single or double reconnection events.

Weißmann and Pinkall in [64] have developed a different method for reconnecting approaching vortex filaments using a variational approach. They developed this method for use in special effects and videogames while maintaining the realism of fluid flow. Their

variational approach aims to match two objectives: The velocity field of the vortex tangle after reconnection should be close to the velocity field of the vortex tangle before reconnection. The other objective is that the length of the tangle after reconnection should be as small as possible, and therefore smaller than the tangle length before reconnection.

To decide whether a reconnection happens, Weißmann and Pinkall define a functional for the tangle before and after reconnection as $F(\gamma)$ and $F(\eta)$ respectively. The functional of the tangle after reconnection is given by:

$$F(\eta) = \lambda \Gamma L(\eta) + d(\eta, \gamma) \tag{27}$$

Where λ is a constant value which I will explain later, Γ is the circulation, L is the length of the tangles pre and post-reconnection and $d(\eta, \gamma)$ is the difference in the velocity field between the pre and post-reconnection tangles (this is given by the L^2-norm of the difference in velocity field). The reconnection would be only allowed to happen in $F(\eta) < F(\gamma)$, this means that they try to reduce the length of the post-reconnection tangle while trying to maintain the velocity field as close as possible to the pre-reconnection tangle. Weißmann and Pinkall also define the difference in velocity field between the post and pre-reconnection tangles as δ.

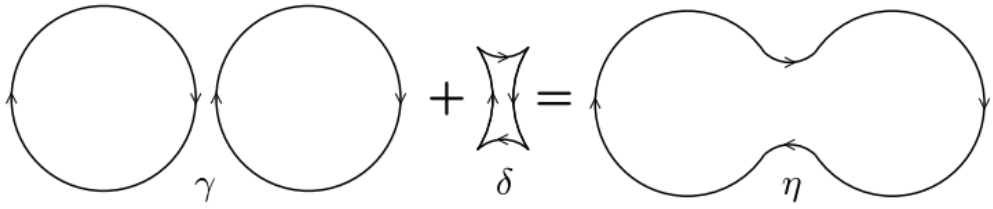

Fig. 5 - Vortex tangles pre and post-reconnection, as well as the difference in their velocity fields, showing that $\eta - \gamma = \delta$. Image taken from Weißmann and Pinkall's work [64].

Knowing this, Weißmann and Pinkall say that the reconnection happens if the following inequality is satisfied:

$$\lambda \Gamma \big(L(\delta_t) + L(\delta_b) - L(\delta_l) - L(\delta_r) \big) + \Gamma \sqrt{flux_\delta(S_a v_\delta)} < 0 \tag{28}$$

Here the subscripts of δ denote the top, bottom, left and right portions of its contour. The positive and negative symbols are because the top and bottom lengths are added to the previous tangle while the left and right lengths are removed from the tangle. The variational approach comes from the parameter λ which decides what part of the functional is most important in the reconnection, either reducing the length of the resulting post-reconnection tangle or maintaining the post-reconnection tangle velocity field as close as possible to the

pre-reconnection tangle velocity. This now poses the question on how accurate and realistic reconnections would look using Weißmann and Pinkall's variational method when dealing with systems of very dense vortex tangles.

2.2.8. Crow Instability

I review the crow instability because it is an important mechanism for the results in **section 5.4.** Two counter-rotating vortices in close proximity develop a quasi-sinusoidal instability on their core, this is called Crow Instability (CI) and was detected in aircraft wake trails by Crow in [65]. The study of this instability was very important for engineering reasons because big airliners would generate a pair of counter-rotating vortices behind them that are a danger for smaller planes that fly through that same space, therefore, it is important to know how long these vortices would last. Crow said that these vortex pairs do not decay by diffusion but they experience an instability (Crow Instability) through which they eventually reconnect and form several vortex rings [65]; an example of Crow Instability can be seen in Fig. 6.

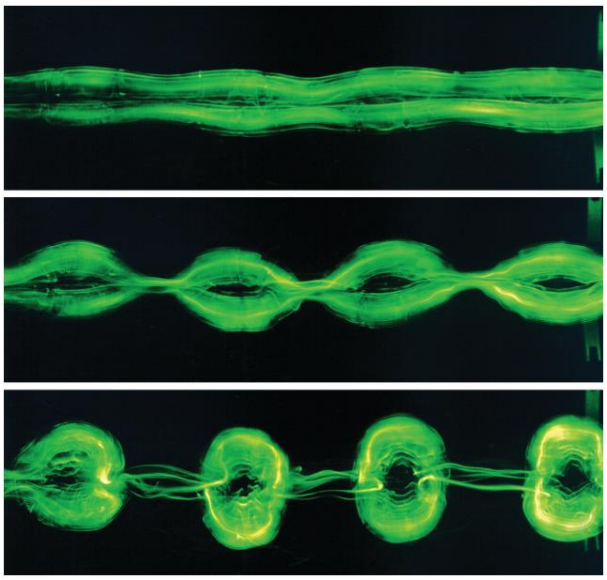

Fig. 6 - Crow Instability visualisation showing the generation of the initial perturbations (top), growth of perturbations (middle) and reconnection at the closest points between the vortices generating a number of vortex rings. Image taken from [66].

The Crow Instability has also been observed in the equatorial ring of supernovas: Wadas et al. in [67] propose that the reason behind the clumps that are formed on the equatorial ring is the Crow Instability that again generates perturbations on a pair of counter rotating vortices which grow in amplitude until they reconnect, forming the previously mentioned clumps. The Crow Instability can also appear for superfluid vortices as shown by Zuccher et al. in [68] and

Simula in [69]. Here they show in several snapshots the development of the Crow instability as the perturbations in two parallel, counter-rotating vortices grow.

2.2.9. Kelvin Waves

Kelvin waves [70] are waves that propagate along the vortex filaments, these are generated after reconnections happen; these were not discovered in experiments in superfluid Helium-4 until Hall in [71]. Svistunov [72] first mentioned that the reconnections that happen between vortex filaments create a region of increased curvature which gives place to the creation of Kelvin waves through the relaxation of the vortex tangle. It is imperative to comprehend these waves as they can lead to further reconnections and changes in the behaviour of the system, especially when Kelvin waves with different wavelengths co-exist along the same vortex filament.

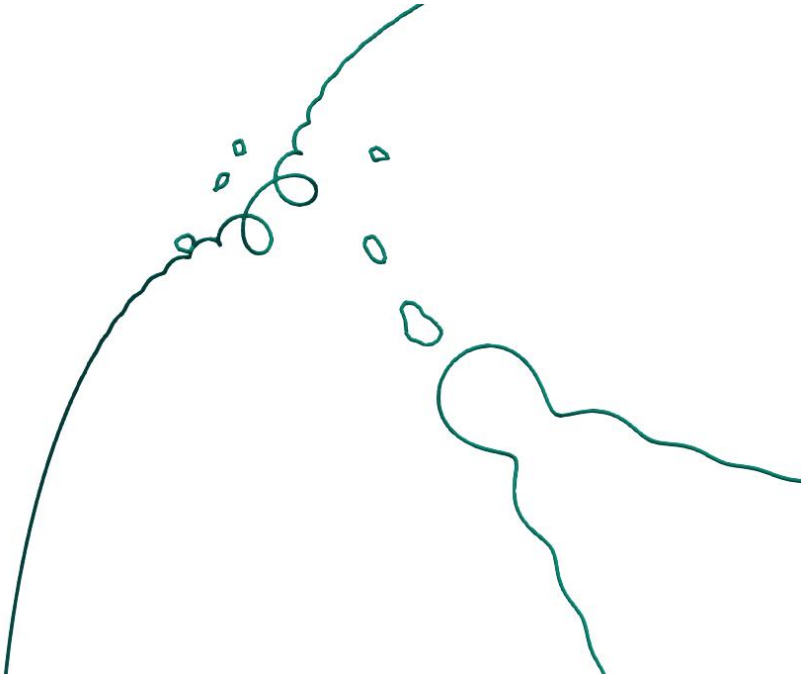

Fig. 7 - Presence of Kelvin waves of different wavelengths coexisting on a quantized vortex filament, they resulted from the reconnection of two different vortex rings. Image extracted from the results in Section 5.1.

It is also important to understand how Kelvin waves propagate and how fast they do so; smaller Kelvin waves travel faster and therefore are in front of the larger Kelvin waves. The Kelvin wave phase velocity is described by following equation [73]:

$$V_{wave}(\lambda) = \frac{\kappa}{2\lambda} \ln\left(\frac{\lambda}{2\pi a}\right) \tag{29}$$

Where $V_{wave}(\lambda)$ is the velocity of propagation of the Kelvin wave, λ is the Kelvin wave wavelength and κ is the quantum of circulation. Other references [74–76] mention the dispersion relation as:

$$\omega = \frac{\Gamma k^2}{4\pi} \ln\left(\frac{1}{ka}\right) + c \tag{30}$$

Where ω is the Kelvin wave frequency and k is the wavenumber given by $k = 2\pi/\lambda$; it is simple to get to **Equation 29** from **Equation 30** by using the relation of k previously mentioned and the relation between the frequency with the velocity of propagation V_{wave}: $V_{wave} = \omega/k$.

2.2.10. Energy Spectra

The study of the energy in a vortex tangle system gives us information about how the kinetic energy is transferred between different length scales within the system as time progresses, and where the kinetic energy resides in wavenumber space. The kinetic energy spectrum is separated into different length scales and can be calculated using equation 32, following the derivation below [77].

The kinetic energy is given by:

$$E = \frac{1}{2}\int \boldsymbol{u} \cdot \boldsymbol{u}\, d\boldsymbol{x} \tag{31}$$

And the vorticity field $\boldsymbol{\omega}$ is given by:

$$\boldsymbol{\omega}(\boldsymbol{x}) = \Gamma \int \frac{\gamma(|\boldsymbol{x} - \boldsymbol{X}_s|/\sigma)}{\sigma^3} \frac{\partial \boldsymbol{X}_s}{\partial s} ds \tag{32}$$

Here Γ is the circulation and γ regards how vorticity is distributed inside the vortex tube, used for smoothing, with radius σ and $\boldsymbol{x}$ and $\boldsymbol{X}_s$ being the target and source vortex points respectively. Taking the Fourier transform of $\boldsymbol{\omega}$ yields:

$$\widehat{\boldsymbol{\omega}}(\boldsymbol{k}) = \Gamma \hat{\gamma}(k\sigma) \int e^{i\boldsymbol{k}\cdot\boldsymbol{X}_s} \frac{\partial \boldsymbol{X}_s}{\partial s} ds \tag{33}$$

Following the derivation by Kivotides and Leonard in [77], use $e^{-i\boldsymbol{k}\cdot\boldsymbol{x}}$ and $1/2\pi$ as factors, taking the inverse transform and defining wavenumber $k = 2\pi/l$, where l is a length scale. The energy spectrum is then calculated as:

$$E(k) = \frac{1}{2(2\pi)^3}\int |\widehat{\omega}|^2 d\Omega_k = \frac{\Gamma^2[\hat{\gamma}(k\sigma)]^2}{2(2\pi)^3} \iiint e^{i\boldsymbol{k}\cdot(\boldsymbol{X}_s - \boldsymbol{X}_{s'})} \frac{\partial \boldsymbol{X}_s}{\partial s} \cdot \frac{\partial \boldsymbol{X}_{s'}}{\partial s'} ds\, ds' d\Omega_k \tag{34}$$

$d\Omega_k$ is the differential solid angle (dimensionless).

Integrating over $d\Omega_k$:

$$E(k) = \frac{\Gamma^2[\hat{\gamma}(k\sigma)]^2}{(2\pi)^2} \int\int \frac{\sin(k|\boldsymbol{X}(s) - \boldsymbol{X}(s')|)}{k|\boldsymbol{X}(s) - \boldsymbol{X}(s')|} \frac{\partial \boldsymbol{X}(s)}{\partial s} \cdot \frac{\partial \boldsymbol{X}(s')}{\partial s'} ds ds' \quad (35)$$

For the energy spectra calculations, I use a Gaussian smoothing kernel which dictates function γ; as shown by Winckelmans and Leonard in [78], the Fourier transform of function γ is simply $\hat{\gamma}(p) = \gamma(p/\sqrt{2})$, where p is a trivial variable used to show the relation between γ and its Fourier transform.

The energy distribution along different length-scales does not remain constant as time progresses, this is because as Kelvin waves propagate, they interact and superpose with each other, generating new and smaller Kelvin waves and in turn transferring energy to them; this would result in an increase in energy concentration at small scales which would become more and more apparent as time continues to progress [39]. This is what is called an energy cascade, the transfer of energy from larger to smaller scales as time progresses; this is a main topic of investigation in this thesis, together with the energy spectra signature of vortex stretching; the mechanisms through which these were studied are explained in the chapter, **"Algorithms and Numerical Methods"**. I work with two different mechanisms of energy transfer: one is vortex stretching and the other is the energy transfer related to the interaction of Kelvin waves of different wavelengths. The former is related to polarised bundles of quantized vortices and the latter is related to the reconnection of isolated vortices.

2.3. Quantized Vortex Bundles

A bundle of polarised quantized vortices can be thought of as a discretisation of a Navier-Stokes vortex, this I can use to investigate the physics of vortex stretching from the energy point of view. The purpose of the second part of the results is not as much to investigate the physics of the quantized vortices but to use this quantized vortex bundle as a Navier Stokes vortex analogue to study Navier-Stokes physics.

There are a number of publications in superfluid turbulence that say that these filaments could form a bundle of vortices [79–83], the question now is, if these vortices form bundles, do they have similar behaviour to classical vortices? There is a difference between quantized and classical fluids vortices in terms of the ability to stretch, Chorin [4] discusses this: a classical vortex when it stretches, its core size is reduced; for a quantized vortex, as the vortex

core is fixed, vortex stretching (resulting in shrinking of the core in the radial direction) cannot happen; these vortices can stretch but only in length. When quantized vortices are organised into polarised bundles, vortex stretching could be achieved by stretching the vortices lengthwise and decreasing the bundle core thickness accordingly, this results in an enstrophy increase.

Baggaley et al. [79] study how superfluid vortices in quantum turbulence form polarised bundles and then reflect on the similarities between superfluid vortex bundles and classical fluid vortices. They use the Biot-Savart equation as the governing equation and use a reconnection algorithm when individual vortices come too close to each other. Baggaley et al. also stress that these superfluid vortices, due to their fixed thickness, cannot undergo vortex stretching and acceleration-wise, they use a tree method. To check if the original superfluid vortices grouped up into bundles, they used a periodic box and a Gaussian kernel to spread the vorticity in the domain. For their initial conditions, Baggaley et al. set up a number of random straight-line vortices that align with either the x, y or z axis in a periodic box of size $7.5 \times 10^{-1} cm$ and let the calculation run for a simulation time t=0.06s. They calculate the spectrum using a 1024^2 mesh on the xy-plane at z=0 and it depends on the grid resolution and the smoothing. They claim in their results that a $k^{-5/3}$ regime appears in the spectrum at k values smaller than the intervortex spacing. The calculation that Baggaley et al. did, had very specific and possibly unphysical initial conditions, which upon inspecting, already had bundles of vortices. After a period of time, they observe a $k^{-5/3}$ law in a short range of wavenumbers within which they have 4 points. This may contradict Kivotides in [84], here Kivotides mentions that parallel vortices (same vorticity direction) repel each other while antiparallel vortices (opposite vorticity direction) attract each other. This means that to form a bundle of polarised vortices there needs to be energy transferred from the normal component to the superfluid component through mutual friction; therefore in the T=0 limit, where there is no normal component of the fluid, the generation of polarised vortex bundles, and the consequent vortex bundle stretching, seems improbable.

Another numerical study of the formation of these polarised bundles in a quantum fluid was done by Kivotides in [85], however in this study, the formation of these superfluid vortex bundles are due to the normal fluid. Here Kivotides also uses the Biot-Savart integral to compute the velocity of the superfluid vortices and then calculates the interaction between the normal and superfluid components using mutual friction parameters. Kivotides carries

out numerical calculations for helium II at T=1.3K and a quantum of circulation $\kappa = 9.97 \times 10^{-4}\ cm^2\ s^{-1}$, the normal fluid on the other hand is around 100 times stronger with a circulation $932.12 \times 10^{-4}\ cm^2\ s^{-1}$. The computational complexity of this problem is such that it was simplified to initially only computing the dynamics of the normal fluid vortices until a homogeneous turbulence has been achieved. Then, the vortices are maintained constant through time and a single superfluid vortex ring was added; the normal fluid vortices transferred energy to the superfluid ring, which eventually multiplies. Kivotides shows graphical evidence of bundles of superfluid vortices forming and then joining together forming what he calls a *vortex braid*. Kivotides also computed the same problem with different temperatures and normal fluid Reynolds number to achieve similar conclusions. It is important to note that this bundling that Kivotides shows only happens when the normal fluid vortex is kept stationary, he demonstrates in a later study [86] that when the normal fluid vortex is not stationary, the superfluid vortices do not tend to form bundles; I will review this work next.

In another study [86], Kivotides studies the interactions between superfluid and normal fluid vortex rings in helium-4 using two different methods with their own advantages and disadvantages. The first method is based on pure vortex dynamics calculations for both the superfluid and the normal-fluid vortex rings, calculated using the Biot-Savart law, and the second method is a hybrid that encompasses pure vortex dynamics for the superfluid vortices and Navier-Stokes physics for the normal-fluid. The normal and superfluid components are coupled through mutual friction, but in the first method (pure vortex dynamics) the effect of the superfluid vortices on the normal-fluid vortex ring is not considered, therefore only the effect of the normal-fluid vortex on the superfluid vortices is included in the model. The second method (hybrid) includes the effects of both the normal and superfluid vortices on each other. Using the first method, Kivotides computes 3 different configurations: 1 normal-fluid vortex ring and 25, similar sized, superfluid vortex rings placed and oriented randomly in a periodic box. Due to the difference in circulation between the normal and superfluid vortex rings, the normal-fluid vortex moves much faster than their superfluid counterpart. Another configuration is the same as the one previously described but with the superfluid vortex rings being much smaller (between 8% and 12% of the normal-fluid vortex ring radius) and there being 300 superfluid vortex rings in the system. The last configuration deals with just one normal-fluid vortex ring and a single superfluid vortex ring comparable in size to the ones in the second configuration, these vortices travel in the same direction. Kivotides results

using this method show that the normal-fluid vortex ring “swallows” the superfluid vortices and transfer energy to them, stretching them to a size similar to the normal-fluid vortex ring; the superfluid vortices, though, do not get trapped inside the normal-fluid vortex core because the normal-fluid vortex moves much faster. Kivotides, using the hybrid method, computes a configuration similar to configuration 2 of the pure vortex dynamics method; this time with 600 superfluid vortex rings and a 128^3 grid for the normal fluid. Again, the normal-fluid vortex ring “swallows” the superfluid vortex rings which are later left behind, due to the difference in velocity, after stretching them radially to a radius similar to the normal-fluid vortex ring. Kivotides concludes that the biggest effect of a normal-fluid vortex ring on superfluid vortices is that it transfers energy to them, resulting in the superfluid vortices being stretched. The superfluid vortices are not locked inside the normal-fluid vortex ring, which could mean that coherent superfluid vortex bundles that are studied in other works, like in [87], have to be inserted in the system by design and do not emerge purely by the dynamics of the system.

Baggaley in [82] discusses the existence of polarised bundles of vortices and how they are important towards the classical Kolmogorov scale and energy transfer; they mention that these bundles can also form in the T=0 limit and that they are needed for a Kolmogorov scaling. As mentioned before, as superfluid vortices are quantized and have a fixed core, they cannot experience vortex stretching in the same way as classical fluid vortices; for this reason, bundles of such quantized vortices are needed for vortex stretching and energy transfer. Baggaley makes a very interesting comment about the similarities between superfluid vortex bundles and classical fluid vortices; bundles of superfluid vortices allow them to act like classical vortices. Baggaley models vortex lines in the following way: the filament is discretised into a large number of vortex points which can vary as the simulation advances, and the distance between neighbouring points is maintained somewhat constant by adding or removing vortex points when points get too far or too close respectively. Baggaley computes the Biot-Savart integral to calculate the velocity of the superfluid vortices and uses a tree algorithm to accelerate the computation. Regarding the energy spectra calculation, Baggaley calculates the spectra on a 512^2 grid that aligns with the xy-plane at z=0, this method depends on the grid resolution and the smoothing. Baggaley computes a system of pure superfluid vortices with 3 different configurations: 100 random vortex rings with 0.0095cm radius, this yielded a k^{-1} scaling in the energy spectra and no vortex bundles; Baggaley points out that this is because there was not enough energy at large scales. The

next simulation involves 10 random loops with 0.095cm radius, in this case again, there is no Kolmogorov scale, and no coherent structures were present, a k^{-1} scaling is shown again. Lastly, a simulation with 15 straight vortex lines (plus 3 more with the same vorticity direction and offset by an intervortex spacing value) that aligned with the x, y and z axis randomly was done, Baggaley claims a Kolmogorov scaling ($k^{-5/3}$) is present at wavenumbers smaller than the intervortex spacing, and therefore the individual vortices grouped up into bundles. First, the initial conditions set by Baggaley are very specific and possibly unphysical which also present bundles of vortices by placing 15 groups of 4 vortex lines each in space. Therefore, I have no reason to believe that the bundling that Baggaley claims does not come from the bundles that are already present at the initial conditions; furthermore, Baggaley says that if the spacing between the vortices in the bundle is very large, there would be no evidence of bundling.

Rusaouen et al. [80] also discuss polarised bundles of superfluid vortices comparing them to classical vortices, but this time they compare them experimentally to quantum fluids with different fractions of superfluid component, ranging from 0% up to 83%. Their purpose for this was to experimentally detect these vortex bundles and compare the distribution magnitude and occurrence of these two types of vortices. For their experiment, Rusaouen et al. use liquid helium-4 contained in a vessel at different temperatures and pressures to achieve different superfluid component fraction in the quantum fluid; this fluid is stirred by 2 discs (at the top and bottom of the container). If the discs rotate at the same and opposite rates, there would be a mixing layer in the mid-point between the discs, Rusaouen et al. vary the rotation rates of the two discs to move this mixing layer up or down. They use pressure probes to detect pressure drops inside cohere vortex structures, but these probes can also pick up mechanical and acoustic noise. To overcome this, two near pressure probes were monitoring the pressure, if only one of the probes detected a pressure drop, this would rule out the possibility of the pressure drop being generated by external noise. There could be times where a pressure drop captured by both probes with a delay that is comparable to the direction of the flow inside the container, Rusaouen et al. say that this would confirm that the pressure drop recorded would be from a coherent vortex structure. Rusaouen et al. conclude that their apparatus could not resolve individual quantum vortices but could detect coherent structures; they found that the occurrence and strength of the coherent structures that they recorded were indiscernible when the superfluid component fraction was between 19, 79 and 83%.

It would be interesting to review Navier-Stokes vortices, focusing on vortex stretching. Chatelain et al. in [88] present results from a direct numerical simulation regarding vortex pairs generated by wakes from aircraft wings; they do this by running parallel calculations of vortex particles methods with a separate mesh for the velocity field and the particles, these two exchange quantities using interpolation schemes. Chatelain et al. set up initial conditions to simulate the appearance of instabilities on the vortices, one of which is the Crow instability. When waves developed by the crow instability grow, they eventually reconnect to form vortex rings; this can also be seen in the work by Wadas et al. [67]. The vortices are undisturbed at first, but a white noise was added to initiate the instability. Chatelain et al. use an open-source library called Parallel Particle Mesh [89] together with Message Passing Interface (MPI) to parallelise their vortex particle methods algorithm.

Kivotides and Leonard in [90] create a turbulence model where Navier-Stokes fluid vortices have quantized circulation; the system consists of a number of vortex filaments with dynamic cores of quantized circulation, therefore the filaments have finite cores that can change locally in time but cannot experience any vortex core torsion. Kivotides and Leonard would like to know if this model is useful to better understand turbulence theory. In their calculations the governing equation is the Biot-Savart law, which describes the motion of the vortices. When dealing with superfluid vortices, the vorticity is a delta function, but as Kivotides and Leonard are working with classical fluid vortices, their vorticity is distributed using a high-order algebraic kernel found in [78]. Their vortex cores can shrink radially as they stretch longitudinally which follows the conservation of volume of vortex tubes and if two vortices come close enough together, they reconnect, which generates a series of Kelvin waves. Their calculation consists of 192 vortex rings randomly sized and oriented in 3-dimensional space with periodic boundary conditions with a $Re = 5000$. The tangles evolve from the initially smooth, perfect circle shape into a more corrugated tangle due to the reconnections that happened. After t=0.14 Kivotides and Leonard claim to see a $k^{-5/3}$ at large wavenumbers k and say that the stretching happening in the vortices helps to understand the Kolmogorov scaling. Kivotides and Leonard conclude that when dealing with superfluid turbulence, the $k^{-5/3}$ scaling is missing because the vortex filaments in this case have no core size.

2.3.1. Vortex Stretching During Vortex Reconnection

As individual quantized vortices are able to reconnect, bundles of these vortices can also undergo reconnection, this is studied by Alamri et al. in [91], where they do calculations studying the behaviour of vortex bundles at T=0 and T=1.65K; I will only review what is directly related to my work, that is the T=0K case. They mention that when vortices are organised into bundles, they can stretch by reducing the spacing between each filament. Alamri et al. use two bundles of straight-line vortices while inside a periodic box, they note that when only one bundle is present the vortices forming the bundle would rotate because they rotate in the same direction. They see in their calculations that when the bundles collide, Kelvin waves are generated due to the high curvature of that section. After repeating the calculation for different number of vortices forming the bundles (5, 7, 9 and 11), they did these calculations using both a vortex filament method (Biot-Savart) and the Non-Linear Schrödinger Equation (NLSE) and they conclude that the vortex bundles resisted the reconnections and that they survive for enough time to travel a distance longer than their bundle core; these results were the same for both methods used. Their NLSE method is computed on a much smaller system size: their Biot-Savart calculation was done on a box size of $2\,cm$ while their NLSE method was done on a much smaller box size, approximately $4.7586 \times 10^{-7} cm$; I approximated this by estimating 17 grid points they use to discretise a vortex core at 1.0 density level and spread that over the 256 grid points that define their box size. This is a rough approximation of their box size but shows that their NLSE method is computed in a box size around 6 orders of magnitude smaller than their vortex filament method. Alamri does not focus on the vortex stretching aspect of reconnections and my interest is not the bundles of quantized vortices but mostly I want to make connections with Navier-Stokes physics; therefore, I will review classical fluid vortex stretching and reconnection works.

Vortex stretching happen, as its own name indicates, when a vortex tube is elongated or stretched. This, for Navier-Stokes vortices results in a thinning or shrinking of the vortex tube core radially, which would in turn mean an intensification of the vorticity in that area due to the circulation having to stay constant along the vortex tube length; as Tabak explains in [92], you can compare it to how fluid accelerates when it passes through a radially smaller portion of a tube to follow the conservation of mass. Imagine a vortex cylinder that has length l, core radius r and vorticity ω; such vortex cylinder can be seen in Fig. 8. As mentioned by Chorin in

[4], a cylinder vortex as seen in Fig. 8 has an enstrophy $\varepsilon = \int_T |\omega|^2 \, dV_T = \pi r^2 l |\omega|^2$. Where T is the vortex cylinder of vorticity ω, radius r, length l and volume dV_T.

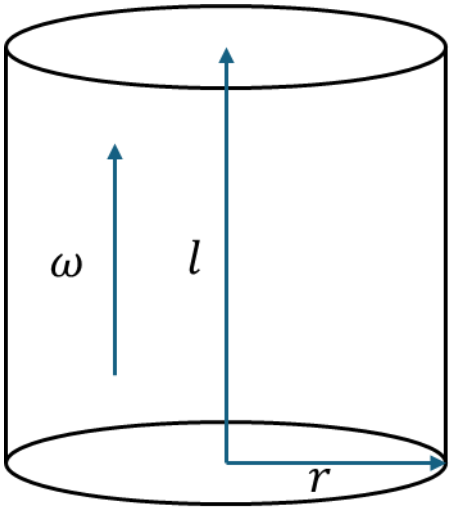

Fig. 8 - Vortex cylinder with radius r, length l and vorticity ω. This example was inspired from Chorin's book [4].

Chorin explains that if the vortex cylinder found in Fig. 8 were to be stretched by a factor α in the direction of its main axis, its new length would be $l' = \alpha l$. Then, following the conservation of volume, the corresponding radius after stretching would be $r' = r/\sqrt{\alpha}$ and the new vorticity magnitude would be $|\omega'| = \alpha|\omega|$; due to the stretching, the enstrophy was amplified and now has a value $\varepsilon' = \alpha^2 \varepsilon$. Therefore, for incompressible flows, the lengthening that happens in the direction of vortex tube due to a difference in velocity at different portions of the vortex, it is accompanied by shrinking in the direction perpendicular to the stretching direction (radially with respect to the vortex tube core). This thinning is only present for Navier-Stokes vortices and not in quantized vortices, this is due to the quantized vortices having extremely thin vortex cores of constant size.

Ashurst and Meiron in [12] study the dynamics and reconnections of two identical classical vortex tube rings with dynamic vortex cores using a “Hybrid” method for the dynamics of said vortices. They start by calculating the dynamics of two vortex tube rings that are co-planar in the y-z plane and move in the positive x-direction using the Biot-Savart law; the ring parameters are as follows: Ring radius = 1 unit, core radius = 0.1 units, circulation = 4π and a separation between the ring centres = 2.5 units. Given their position and their direction, the closest points between the vortices are anti-parallel. This calculation shows how the rings deform especially in the portions of the rings that are closest to each other; these portions are stretched longitudinally, and their core experience a corresponding shrinking in the radial

direction (vortex stretching). Continuing this calculation results in a continuous core shrinking and the generation of fractal patterns on the vortex tube. Ashurst and Meiron then restart their calculation with the incompressible Navier-Stokes equation (Re = 1000) when the distance between the two rings is 0.14 units (the final Biot-Savart calculation data is used as the initial conditions for the incompressible Navier-Stokes calculation). This calculation, instead of continuously stretching and shrinking the vortex core, results in a vortex reconnection (topological change) with a minimal change in the vortex core sizes. At the beginning of the Navier-Stokes calculation, the vorticity has a positive and negative z-direction at the closest section between the vortices; this vorticity is slowly rotated from the z-direction (positive and negative) to the y-direction (positive and negative). Ashurst and Meiron also calculate the same system for other Reynolds number (10, 100, 1000 and 5000) and they found that the results for Re = 1000 and 5000 did not have any apparent difference; when Re = 100 the reconnection still happens but the vortex cores are more diffused. When Re = 10, the diffusion is so great that the vortices do not reconnect. Ashurst and Meiron also state that the time needed for the reconnection to happen depends on the local shape of the vortex cores; for this they started a Navier-Stokes calculation with perfectly circular vortex rings at the same distance as in the previous case and compared the time taken for the vortex rings to reconnect. They found that for the perfectly circular vortex rings at t = 0.048, the reconnection was not completed yet, while in their previous case, the reconnection was finished at 0.024; this difference in time could come from the larger local curvature at the closest sections between the vortex rings, which moves these sections together.

Kida and Takaoka in [13] describe a different mechanism for vortex reconnections called bridging. They compute direct numerical simulations of the Navier-Stokes equation; in the initial conditions they have a vortex tube with the shape of a trefoil and a Gaussian vorticity distribution. They carry out the calculation at viscosity values $\nu = 0.001, 0.002$ and 0.005. Kida and Takaoka point out important features of their simulation configuration: The trefoil knot moves and rotates together in a counterclockwise manner. Soon after the calculation starts, because the tangle is unstable, the vortex tube starts to twist and fold in such a manner that sections that are in close proximity have anti-parallel vorticity direction. Lastly, Kida and Takaoka observe high vorticity parts of the vortex tubes coming out of the main structure; their calculation show that the portions that come out of the tubes are stretched and become connected to a different part of the tube further along the tangle, these are called ‘bridges’ by Kida and Takaoka. The bridges are initially thinner than the main vortex tubes, but as the

calculation continues, they grow to be comparable in size. They show results of vorticity lines forming a hairpin vortex at the bridges, and a vortex line that goes through a bridge to be at different parts of the vortex tube. They conclude by quickly comparing the bridging mechanism in vortex reconnection to the vorticity cancellation mechanism that is studied by Ashurst and Meiron [12]; the bridging mechanism results in a change in topology that is slower than the reconnection through vorticity cancellation.

Melander and Hussain in [14] study the reconnection of two anti-parallel vortex tubes to get an understanding of the dynamics involved in the process and to ultimately generate a model. They use a Gaussian vorticity distribution that they force to zero outside of the vortex tube core. To encourage the reconnection, they disturb the vortex tubes with an identical but opposite sinusoidal instability which are tilted towards each other. As they move towards each other the vortex tubes are deformed by flattening and experience vortex stretching. When they are close enough, Melander and Hussain notice a drastic topological change where there is vorticity annihilation, and two small tubes appear to connect the resulting two main vortex tubes. As the vortex tubes pull apart, the remaining parts of the original vortex tubes are stretched into pairs. They use the value of circulation Γ_z (the same direction as the vorticity in the initial conditions) to determine three distinct regimes: i) core deformation and stretching – This happens while the vortices are moving towards each other and results in vortex stretching and core flattening or sheetification; here Γ_z is maximum. ii) Vorticity annihilation and bridging – This is where the vortex tubes are reconnecting. Γ_z decreases rapidly as it is being transferred to Γ_x (the direction of vorticity in the closest portion of the resulting vortex tubes) due to the change in topology. iii) Decay and threading – Here the main vortex tubes are moving away from each other, and the remaining parts of the original vortex tubes are being stretched; here Γ_z decreases slowly. Melander and Hussain also calculate the same configuration with asymmetrical sinusoidal instabilities, and they found that it yielded the same results.

Chatelain et al. in [93] study numerically the dynamics of the reconnection of two vortex rings, they do this by solving the Navier-Stokes equation for an incompressible fluid with a Reynolds number $Re = 250$. They computed three different configurations: 2 identical rings that travel in opposite directions collide with an offset on their propagation axis, 2 dissimilar vortex rings that travel in the same direction, 2 rings forming a Hopf link with one ring's core going through the middle of the other ring and vice versa. In the first case, Chatelain et al.

observed that when the vortex rings moved closer to each other, they stretched at their closest point prior to reconnecting and formed two different vortex rings. The stretching of the vortices prior to reconnection also happens on the second and third vortex configurations, with the Hopf link configuration showing a much more pronounced stretching and a much larger anti-parallel portion of the vortices. Chatelain et al. found that the reconnections generated secondary structures that have been stretched, and secondarily they also generate a series of Kelvin waves, which according to them are constraint to a large wavelength due to the small Reynolds number used.

I am interested in vortex stretching and there are a large number of works on vortex stretching during reconnections. Indeed, my Hopf link configuration was motivated by this phenomenon, but I have a new configuration, called vortex collider, through which I will study vortex stretching which is not related to reconnections.

3. Physical Model

In this section I will explain the physical model used for all the configurations computed, this includes isolated quantized vortices and bundles of qunatised vortices. The fluid in my model is incompressible and it involves vortex filaments (ideal lines) of fixed core size which represent quantized vortices following the method developed by Leonard in [94], which uses a finite filament model that solves its dynamics exactly (it is not an ad-hoc renormalisation of the Biot-Savart law); this is excluding when calculating the self-contribution towards velocity of vortex points, here I use a method developed by Schwarz [42]. I compute the dynamics of the vortices using the full Biot-Savart equation. An advantage of using this model in contrast with the Gross-Pitaevskii equation is that my vortex dynamics model does not need a grid across the entire computational domain, but only on the vortex filaments in the form of discretisation points; this drastically reduces the computational cells/points that need to be calculated. For example, for a computational box with sides 0.1cm, a quantized vortex core size of $1.58 \times 10^{-8}\ cm$ in radius and a grid that discretises the core in 17 cells across its diameter, similar to the approximation done with the box size in [91], the box would need to be discretised in one direction into $\sim 53.8 \times 10^{6}$ cells; in my vortex dynamics model this number of computational cells/points are not reached as only the vortices are discretised without the need of a grid across the entire computational box.

3.1. Vortex Model

Knowing the differences between classical vortex rings and quantized vortex rings, one of the purposes of my work is to form a bundle of quantized vortices into a torus that resembles the shape of a standard classical vortex ring. Modelling superfluids using the nonlinear Schrödinger equation is possible through the Gross-Pitaevskii equation [95] but in my case I calculate the dynamics of quantized vortices using the Biot-Savart law. I have total freedom to apply any parameters to these vortices, in terms of core thickness, circulation etc. but I chose to use the parameters corresponding to Helium-4; this decision was made because of the abundance of experiments and numerical simulations available [77,96–98]. If I arrange my quantized vortices into bundles, my configurations can have two distinct interpretations; first, it can be interpreted as a bundle of quantized vortices and therefore it would be used to study the dynamics of quantized vortex bundles. On the other hand, the other interpretation regards the discretisation of a classical vortex ring, where the classical vortex core is discretised into the individual vortex filaments. Each of the filaments are configured to have a certain circulation (in my case being the quantum of circulation of superfluid Helium-4: $\kappa =$

$9.97 \times 10^{-4}\ cm^2 s^{-1}$), therefore the total circulation of the modelled classical vortex ring would be $\Gamma = N\ \kappa$, where N denotes the number of vortex filaments that discretised the classical vortex ring. The second interpretation has been employed by Kivotides and Leonard in [99], here they discretise a vortex tube into a bundle of vortex lines, the number of discretisation vortex lines was limited to 9 due to computational complexity. Fig. 9 shows two linked classical vortex rings that have been discretised and organised in the same manner as in [99] but with a larger number of vortex rings.

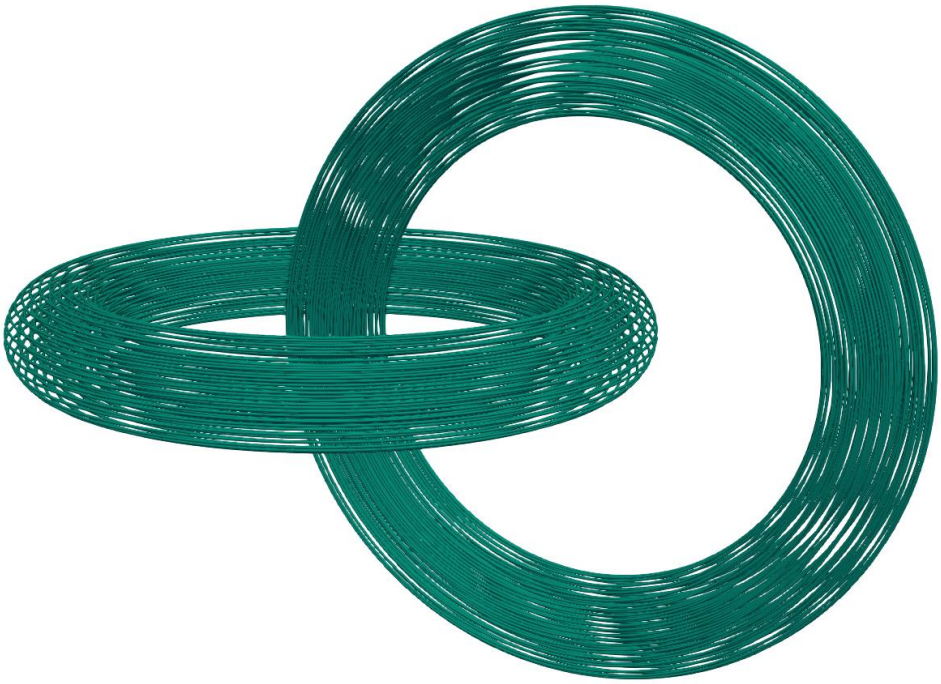

Fig. 9 - Two possible interpretations: a) two bundles of quantized vortex rings in a Hopf-link configuration and b) two classical vortex rings in a Hopf-link configuration, discretised into 81 quantized vortex rings each.

As mentioned before, the individual filaments can be configured to have different parameters, this becomes very useful when dealing with the discretised classical vortex rings interpretation. Increasing the quantum of circulation value of each individual quantized vortex ring would result in a classical vortex ring with higher circulation, and therefore would allow me to undertake calculations of classical vortices with a higher Reynolds number without the problem of increasing computational complexity. Increasing the circulation value of each individual vortex ring would introduce a numerical instability problem which can be smoothed out giving the quantized vortices a larger numerical core size and a vorticity distribution across it, which will be discussed later.

3.2. Vortex Reconnection Model

The vortex filament method that I employ in my calculation is unable to take into account reconnections of two vortex filaments or a self-reconnection, in order to account for vortex reconnections I use the algorithm explained by Kivotides in [84], which is based on Schwarz's [42] original idea. I will give an explanation on the conditions and parameters that are considered in this algorithm. Imagine two vortex filament sections that approach each other and denote 3 vortex points on each filament as $\{\boldsymbol{X}^{i-1}, \boldsymbol{X}^{i}, \boldsymbol{X}^{i+1}\}$ and $\{\boldsymbol{X}^{j-1}, \boldsymbol{X}^{j}, \boldsymbol{X}^{j+1}\}$, where the i and j indices denote 2 different vortices (therefore $i \neq j$) and the $i+1$ and $i-1$ (and $j+1$ and $j-1$) are neighbouring points of i (and j) that follow the direction of vorticity. Say the vortex points are separated by a distance δ_v which is comparable to the discretisation length of the vortex tangles Δx_{sv}; the algorithm is capable of adding or subtracting vortex points from the tangle if neighbouring points separate or come together too much respectively (this is controlled by a parameter $\alpha = 1.65$), therefore the distance between neighbouring points obeys the following inequality:

$$\Delta x_{sv}/\alpha < \left|\boldsymbol{X}^{i} - \boldsymbol{X}^{i-1}\right| < \alpha \Delta x_{sv} \tag{36}$$

The inter-vortex spacing is defined as:

$$\delta_{iv} = \sqrt{V_{sys}/L} = 1/\sqrt{\Lambda} \tag{37}$$

Where V_{sys} is the volume of the system, L is the tangle length and Λ is the vortex line density calculated as $\Lambda = L/V_{sys}$. The reconnection algorithm makes use of both the discretisation distance and the vortex line density and therefore a topological change in my calculations looks like the following [84]:

$$\begin{gathered}\{\boldsymbol{X}^{i-1}, \boldsymbol{X}^{i}, \boldsymbol{X}^{i+1}\} \wedge \{\boldsymbol{X}^{j-1}, \boldsymbol{X}^{j}, \boldsymbol{X}^{j+1}\} \wedge [|\boldsymbol{X}^{i} - \boldsymbol{X}^{j}| < \beta \min(\Delta x_{sv}, \delta_{iv})] \longrightarrow \\ \{\boldsymbol{X}^{i-1}, \boldsymbol{X}^{i}, \boldsymbol{X}^{j+1}\} \wedge \{\boldsymbol{X}^{j-1}, \boldsymbol{X}^{j}, \boldsymbol{X}^{i+1}\}\end{gathered} \tag{38}$$

Equation 34 shows how the two approaching vortices would reconnect and what the condition to reconnect is. This is what differs this reconnection method from the one proposed by Schwarz in [42], the algorithm is capable of selecting a criteria between discretisation length and inter-vortex spacing depending on which is smallest. When the system is very dense, and the inter-vortex spacing is smaller than the discretisation length, the algorithm uses the inter-vortex spacing as the criteria for reconnection in order to avoid many unnecessary reconnections [84]. In **equation 34**, β is a parameter smaller than 1 that is of great importance in the reconnection algorithm and serves as a gauge for 2 different

effects. The first is that it controls how often the reconnections happen in a system: if I increase β, the reconnection distance threshold increases and therefore the rate of reconnections increases; the opposite would happen if I decreased the value of β. The other effect is that it controls the rate at which the reconnections decrease the tangle length. Kivotides in [84] explains that this is a crucial feature because when two vortices reconnect, some kinetic energy is transformed into acoustic energy; this is mentioned by Narita and Baumjohann in [76] and Ogawa et al. in [48], Leadbeater et al. in [62] make quantitative measurements of the kinetic energy transformed into acoustic energy for different reconnection angles. My incompressible vortex filament method is not capable of modelling this sound generation, therefore decreasing the tangle length after a reconnection is a possible way of imitating the energy loss in the tangle; so the reconnection only happens if it would result in a decrease in the total tangle length. A graphical interpretation of **equation 34**, representing a vortex reconnection can be seen in Fig. 10.

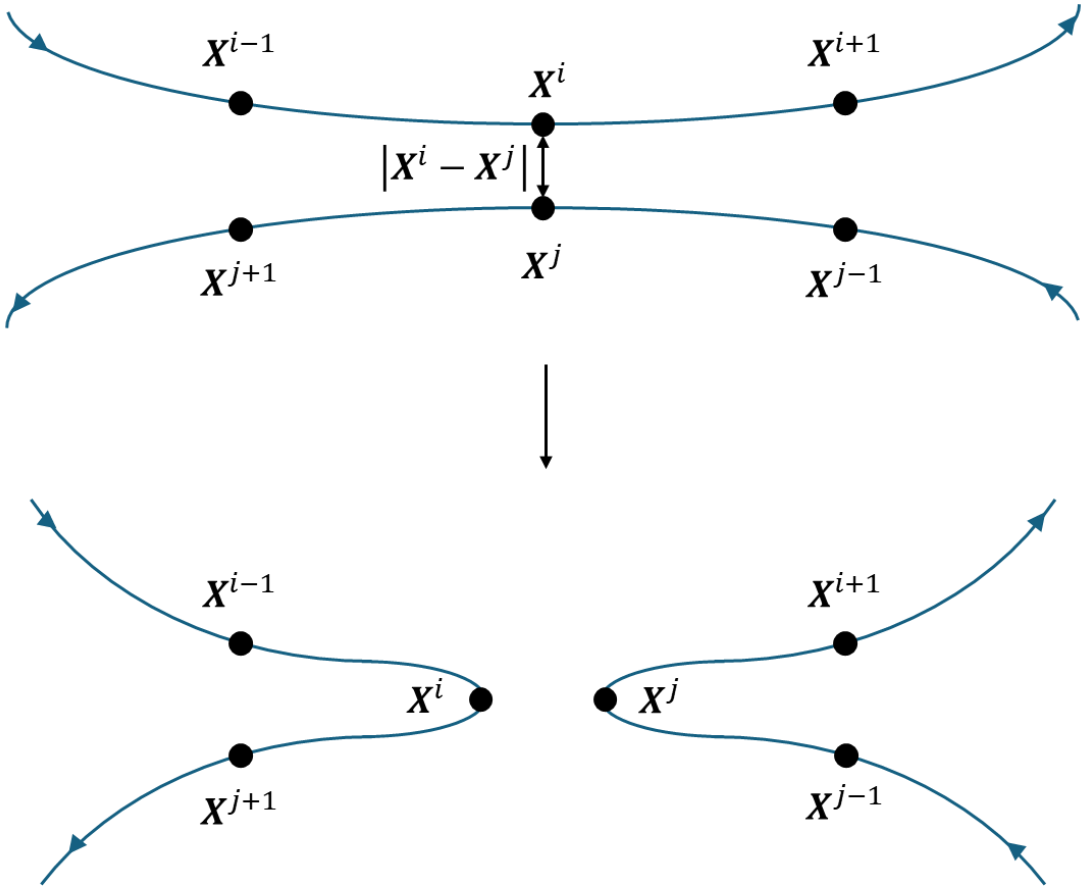

Fig. 10 - Graphical representation of a reconnection happening using the reconnection algorithm developed by Kivotides in [84].*The arrowheads denote the direction of vorticity in each tangle.*

4. Algorithms and Numerical Methods

In this section I discuss the two algorithms used for this research, these algorithms compute the Biot-Savart integral and the energy spectra of a system of superfluid vortex tangles. I also discuss which numerical method was used to evolve the superfluid vortex tangles in time and how the calculation was damped to avoid any numerical instabilities; lastly, I explain in detail how the algorithms were parallelised to achieve an acceleration in the execution time and how the acceleration of the Biot-Savart algorithm and energy spectra differ from one another.

4.1. Parallelisation

As mentioned before, both energy spectra and Biot-Savart algorithms have an $O(N^2)$ time complexity because they use a double loop over all vortex points. These algorithms are simple to implement but have poor scalability and are inefficient when the data sets are somewhat large; even when the data sets are not extremely large the algorithm would have a slow execution speed. This reduction in execution speed comes from the fact that as the number of points to be calculated increases (finely discretised superfluid vortex rings), the execution time increases at a much faster rate because the number of steps to complete the algorithm increases with the square of the number of vortex points. Therefore, the performance of the algorithm scales with the square of the number of vortex points. For example, if we had two superfluid vortex systems with 100 and 1000 superfluid vortex points, they would need 10000 and 1000000 operations to complete; the problem becomes obvious when the number of vortex points increases to tens of thousands, hundreds of thousands or even millions of points.

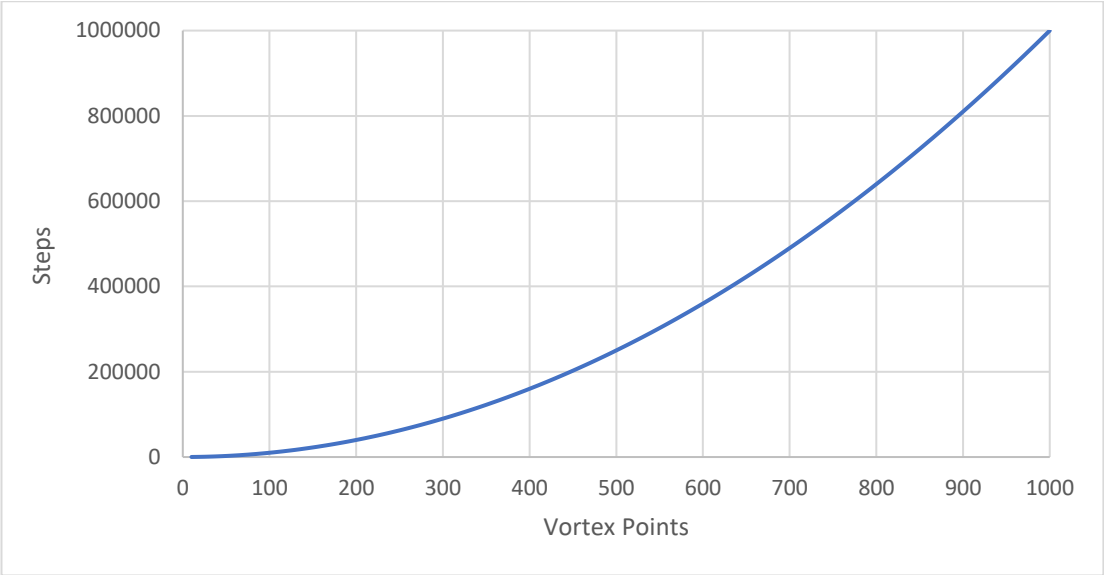

Fig. 11 - Plot showing the number of steps necessary to complete an algorithm with an $O(N^2)$ time complexity.

Here the steep curve of the plot showing how the performance of the algorithm scales with the square of the input values, which are the vortex points in my case.

Therefore, for superfluid vortex systems dealing with several tens of thousands or hundreds of thousands of points, the current serial $O(N^2)$ Biot-Savart algorithm is not efficient enough to make the calculation of the Biot-Savart velocity feasible. I decided to parallelise the Biot-Savart algorithm to accelerate the execution time enough to make its computation feasible; I did this by implementing a version of the Biot-Savart algorithm into "ExaFMM" which is "an open-source library for fast multipole algorithms" developed by Wang, Yokota and Barba in [100]. This library contained several kernels that could calculate a potential in randomly situated particles using only their position in 3-dimensional space and their charge; this is analogous to my system where I calculate a velocity, depending on the vortex points coordinates and the vorticity field. As no Biot-Savart kernel was present in their library I had to translate the Biot-Savart algorithm to fit in their library to ultimately accelerate the execution time of my code. I only utilised the parallelisation capabilities of the library using SIMD parallelisation by feeding my algorithm's variables to "ExaFMM" and then storing "ExaFMM" output values in my algorithm's variables.

The problem regarding execution time regarding $O(N^2)$ algorithms becomes more apparent when calculating the energy spectra of a given system, this is because the $O(N^2)$ algorithm is ran in a loop to calculate the energy value for a desired number of wavenumbers increasing

the number of total steps by a factor of 100-1000. I also wrote a modified version of the energy spectra algorithm to fit within “ExaFMM” library.

4.1.1. SIMD Parallelisation

SIMD or Single Input Multiple Data parallelisation improves the performance of code execution by completing the exact same operations for different data simultaneously. It achieves this by transforming a number of scalar operations into a vector instruction that completes the same operation on all of the vector elements simultaneously; this is called vectorisation [108].

The number of elements that can be calculated simultaneously depends on the number of SIMD units the system running the code has. SIMD units are the components inside computer CPUs (Central Processing Unit) that perform the operations/instructions mentioned previously; each machine, depending on its architecture, possesses a different number of SIMD units [109]. In general, a SIMD unit is given two vectors containing data, completes the required operation and outputs the data to a single vector; from this I know that each SIMD unit deals with a single vector element at a time, therefore if a system has two SIMD units, it would perform the instruction on two vector elements and ultimately calculate two output values simultaneously.

Below is a simple representation of how the data is placed in vectors to perform any given instruction.

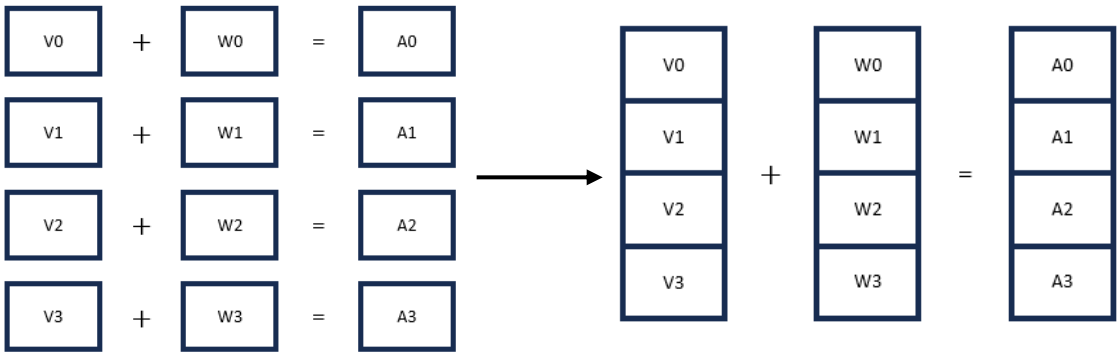

Fig. 12 - Transforming data into vectors to use in SIMD operations.

I can see from Fig. 12 how the data in each of the operations is independent from one another and are carried out individually (V0 + W0 = A0, V1 + W1 = A1, etc.). To use SIMD, I need to group the data in vectors, as shown in the right side of Fig. 12, to later use a single instruction to calculate the value of the entire vector “A”, which contains data points “A0”, “A1”, “A2” and “A3”. This simplified example illustrates a system with four SIMD units.

It is evident from Fig. 12 that I cannot perform an instruction using SIMD if the operation applied to each data point is different. This is not a problem in my investigation as all target data points follow the same operations/instructions, with exception to calculating the self-induced superfluid velocity which was cleverly excluded.

Another concern that may arise from using SIMD to accelerate several operations, is that the number of data points, let that be the number of target vortex points, may not be divisible perfectly by the number of SIMD units. When this happens, I perform as many SIMD instructions as possible, and when there is a remainder of loose data points left, I perform the operations individually, in serial. For example, if I were to perform an operation using SIMD on 150 data points using a machine that has 4 SIMD units, I would be able to carry out the SIMD instructions on 37 vectors (each containing 4 individual data points), and the remaining 2 data points would be calculated using the standard serial procedure. Therefore, I can use this method for any given number of data points, if the machine's RAM can store them that is.

4.1.2. Comparing SIMD Parallelisation to Fast Multipole Method

In this section I will briefly explain what a Fast Multipole Method (FMM) is, and I will compare it to the algorithmic accelerator that I use in my computations. A Fast Multipole Method is an algorithm that is used for computing interactions between particles inside a system with N particles [110]. The interactions that these particles experience (electrical charge, vorticity induced velocity, gravitation, etc.) depend on the kernel utilised; and some Fast Multipole Methods are kernel independent (KIFMM), which means adding new interaction kernels is simple. This method can improve the complexity of a system from $O(N^2)$ (typical of N body problems) to $O(N)$ by dividing the computational domain into quad or oct-trees (quad and oct define the number of children each node has) and, simply put, simplify many source points into one.

My method of accelerating the algorithms is capable of improving the execution time of the algorithms when the system is not very dense. The problem arises when the system has many points, in the order of millions of points, here the SIMD acceleration is insufficient to make the calculation feasible; in such systems a more advanced method like Fast Multipole Method is required. A calculation involving 1,000,000 points would need 10^{12} operations to complete, where an FMM would need as little as 10^6 operations. For the calculations in this thesis, SIMD parallelisation was sufficient to accelerate the algorithms used.

4.2. Algorithms

As was mentioned before, the two algorithms presented for this research are the Biot-Savart integral, which I discretise in Riemann sums, to calculate the velocity of vortex tangles depending on the vorticity field, and the energy spectra, which explains the distribution of energy across several wavenumbers. Now I will explain in detail how both Biot-Savart and energy spectra algorithms work, together with some more general algorithms needed for the calculations to work.

4.2.1. General Algorithm

The algorithm starts by reading an input file that sets different parameters for the calculation and its initial conditions; some of these are what vortex configuration to use, box size, vortex ring radius, quantum of circulation, numerical and diagnostic core size and if the simulation should start anew or restart from a restart point.

After reading the input file, the algorithm starts from t=0 or a restart point, if it is due to restart the algorithm reads an input file containing the necessary information to restart (vortex coordinates, boundary conditions); if on the other hand the input files determines the calculation should start from t=0, the algorithm will generate a tangle of quantized vortices according to the configuration set in the input file. Once the vortices have been generated, an output file containing the vortex points and lines is written.

Now, the decision is made if the algorithm should output data without calculations. If this is the decision, the algorithm would write the coordinates of the vortex points in a file and, if it was activated in the input file, the energy would be calculated and written to a file; more information on the algorithm regarding the energy spectra will be given in **Section 4.2.5**. If the algorithm reads from the input file that it should carry out calculations, it enters a time loop and starts by incrementing the timestep number by 1. Note that at this point in time, the algorithm does not know what is the timestep size, this is done in the next step.

Once the timestep size was calculated, the new position of the vortex points is computed, the specifics of this step are explained in **Section 4.2.3**. If the current timestep is eligible for writing output data and restart points, then this is done. The algorithm then decides if the current timestep is the last in the calculation, if it is, the execution ends, if it is not, the algorithm increments the timestep by one and continues from the start of the time loop.

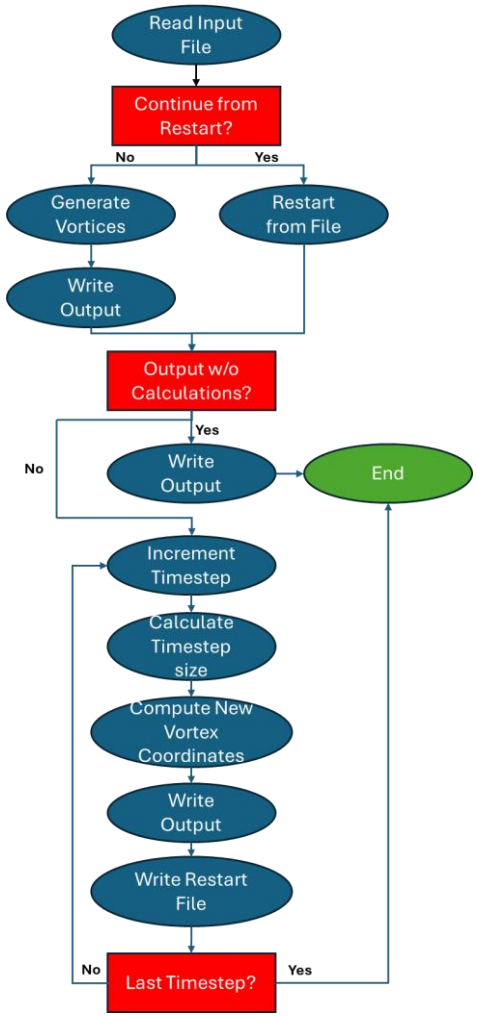

Fig. 13 - Information flow chart of the general algorithm.

4.2.2. Vortex Point Update Algorithm

In this section I will describe the algorithm in charge of updating the vortex points coordinates; this corresponds to the process "Compute New Vortex Coordinates" in the information flow chart shown in Fig. 13. The algorithm starts by defining the number of sub-steps in the Runge-Kutta scheme, in all my calculations this number is three; Runge-Kutta schemes are explained more in depth in **Section 4.5**.

After defining three as the number of sub-steps in the Runge-Kutta scheme, the algorithm stores the current data involving coordinates and vortex point velocities as previous values (if this is during the first timestep and first sub-step, the value of previous velocity would be zero). Then the algorithm calculates the time increments between the different Runge-Kutta sub-steps; it is important to note that increments from one sub-step to another are not constant. Then, the current velocity of the vortex points is calculated using the Biot-Savart

law, this is explained better in **Section 4.2.3**. Once the velocities are calculated, using the current and previous coordinates and velocities, the position of all vortex points is updated for the current Runge-Kutta sub-step, and the current velocities are copied to previous velocities.

Then, the algorithm decides if the current sub-step is the last (the third), if it is not, the algorithm increments the sub-step by 1 and returns to storing the current coordinates and velocities into the previous coordinates and velocities arrays as shown in Fig. 14. If the current sub-step is the last one, then the code checks if there are any reconnections in the vortices and re-meshes the entire length of the vortices and then exits this algorithm. The reconnections are decided if any vortex points come closer together than a parameter set in the input file, it also considers if the reconnection would result in a decrease in total vortex tangle length, as explained in **section 2.2.7**.

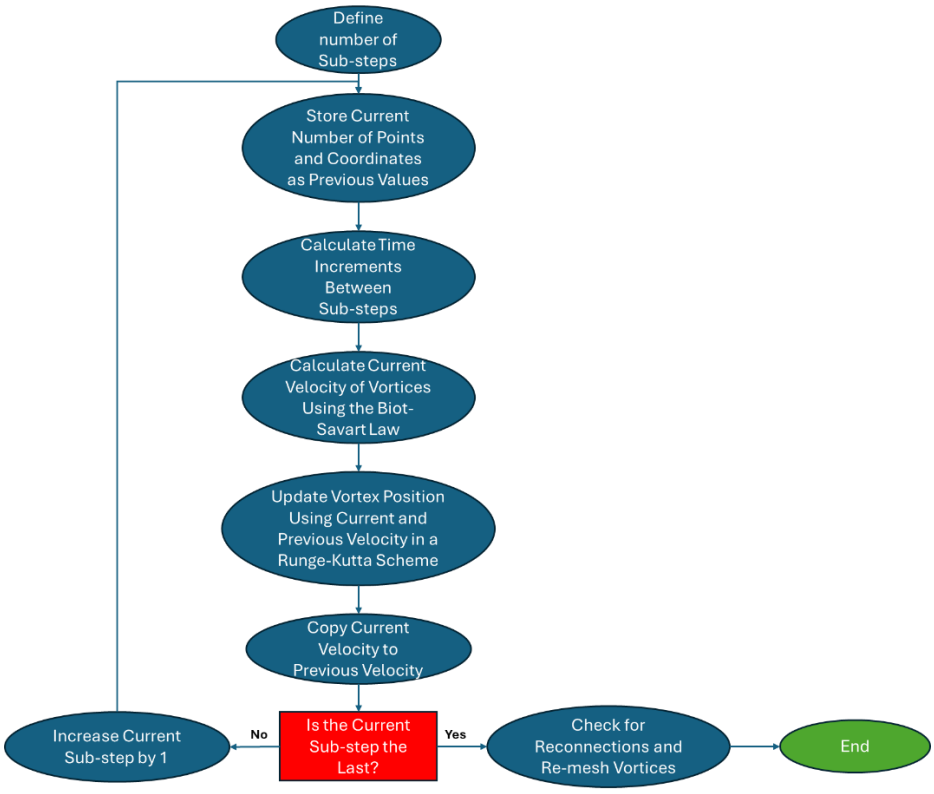

Fig. 14 - Information flow chart of the vortex points update algorithm.

4.2.3. Quantized Vortex Velocity Algorithm

Inside the process “Calculate Current Velocity of Vortices Using the Biot-Savart Law”, there is a complex algorithm that I parallelised using SIMD. To do this I used the environment and libraries found in exafmm-t developed by Wang T, Yokota R and Barba L. in [100]. Due to the

nature of the problem, all vortex points are considered target and source points at some point in the execution. To begin, the algorithm selects the first four target vortex points to calculate the velocity for and then creates and populates SIMD arrays for the coordinates and velocity of said target vortices; because of the nature of this parallelisation, the calculations to be done to one of the targets in this array are also done to the other three simultaneously. Once this is done, the algorithm selects the next source vortex point and calculates the distance magnitude between the targets and source vortex point.

The algorithm then checks if the source vortex point is the same as any of the target points using the distance calculated, if it is, the contribution of this vortex point to itself is set equal to zero; the self-contribution towards velocity is calculated in serial outside of this algorithm. On the other hand, if the source and target point are not the same, the algorithm calculates the contribution of the source point towards the velocity of the target points using SIMD instructions.

Then the algorithm checks if the current source point is the last one, if it is not, it selects the next source vortex point and redoes the process mentioned above. If it is the last source point, then it checks if these 4 target points are the last ones, if they are not then it selects the next 4 vortex points and goes through the steps mentioned above. If they are the last 4 target points, the algorithm enters its serial portion. Because this method can only do 4 target points at a time, if the total number of vortex point is not divisible by 4, then there could be anywhere between 1 and 3 loose vortex points. For these vortex points, their velocities are calculated in serial using the same steps as in the parallel portion of the algorithm, this is shown in Fig. 15.

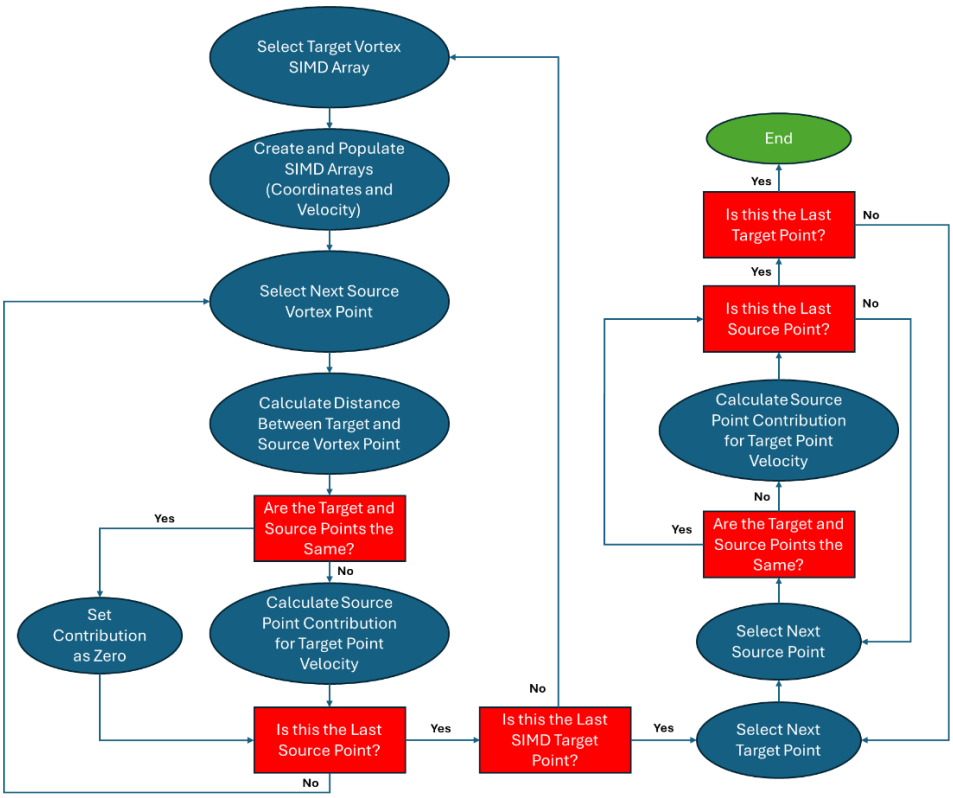

Fig. 15 - Information flow chart of the SIMD Biot-Savart algorithm.

4.2.4. General Energy Spectra Algorithm

In this section I will go over the general algorithm for the energy spectra calculation, I will go over the parallel algorithm in the next section. The algorithm starts by reading from the input file how many wavenumbers to calculate the energy for. Then it finds the largest scale in the system and expands the wavenumber range accordingly; the largest scale is the largest distance between vortex points in the system if the boundary conditions were set as infinite (infinitely large box), if the boundary conditions were set as periodic, the largest scale is the box size, which is determined in the input file. Once the wavenumber has an appropriate range, the algorithm selects a wavenumber and calculates the energy for it. Then, it checks if there are any more wavenumbers to calculate the energy for and if there are then it selects the next wavenumber and follows the process again. If the current wavenumber was the last one, then the execution exits.

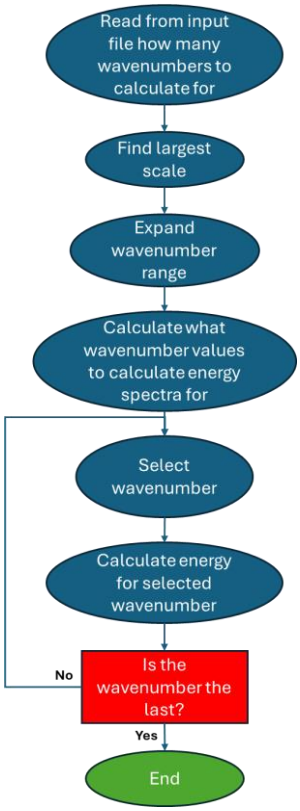

Fig. 16 - Information flow chart of the general energy spectra algorithm.

4.2.5. Parallel Energy Spectra Algorithm

The algorithm explained here corresponds to the process "Calculate energy for selected wavenumber" in Fig. 16. It starts by selecting 4 target vortex points to form a SIMD array, just like in Fig. 15, and creates and populates SIMD arrays for the coordinates and velocities of said vortex points. Then it selects a vortex source point and populates a SIMD array for the Gamma factors in **Equation 31**. The algorithm then calculates the distance between the target and source vortex points and decides if the source point is the same as any of the target points in the SIMD array, if it is, the energy contribution of the current source vortex point is calculated in serial for all target points in the SIMD array (this happens outside of the SIMD environment). This method differs from the one used for the Biot-Savart parallelisation because for the energy spectra I use a Gaussian smoothing kernel [78], which for an identical target and source point, it would result in a division by 0, therefore I have to skip the contribution of that source point for all the target points in the SIMD array. As a comparison with the parallel Biot-Savart integral, I use a High-Algebraic smoothing kernel that for identical source and target points would not result in a division by zero but in an incorrect value for the contribution of the source point to the target point; that is why I can just calculate the contribution of the source point to the target points in the SIMD array, and when one of the

targets is the source point, I can just set that contribution as zero and calculate it later in serial outside the SIMD environment.

Once this is calculated, the algorithm checks if the current source point is the last one, if it is not, it does the same process with the next source point, and if it is, it adds the contribution of energy for the current wavenumber. It then asks if the current 4 target points are the last ones, if it is not, the algorithm selects the next 4 target points, stores them in the SIMD array, and does the process again. If they are the last ones, the algorithm calculates the energy contribution of the remaining target points in serial, as show in Fig. 17.

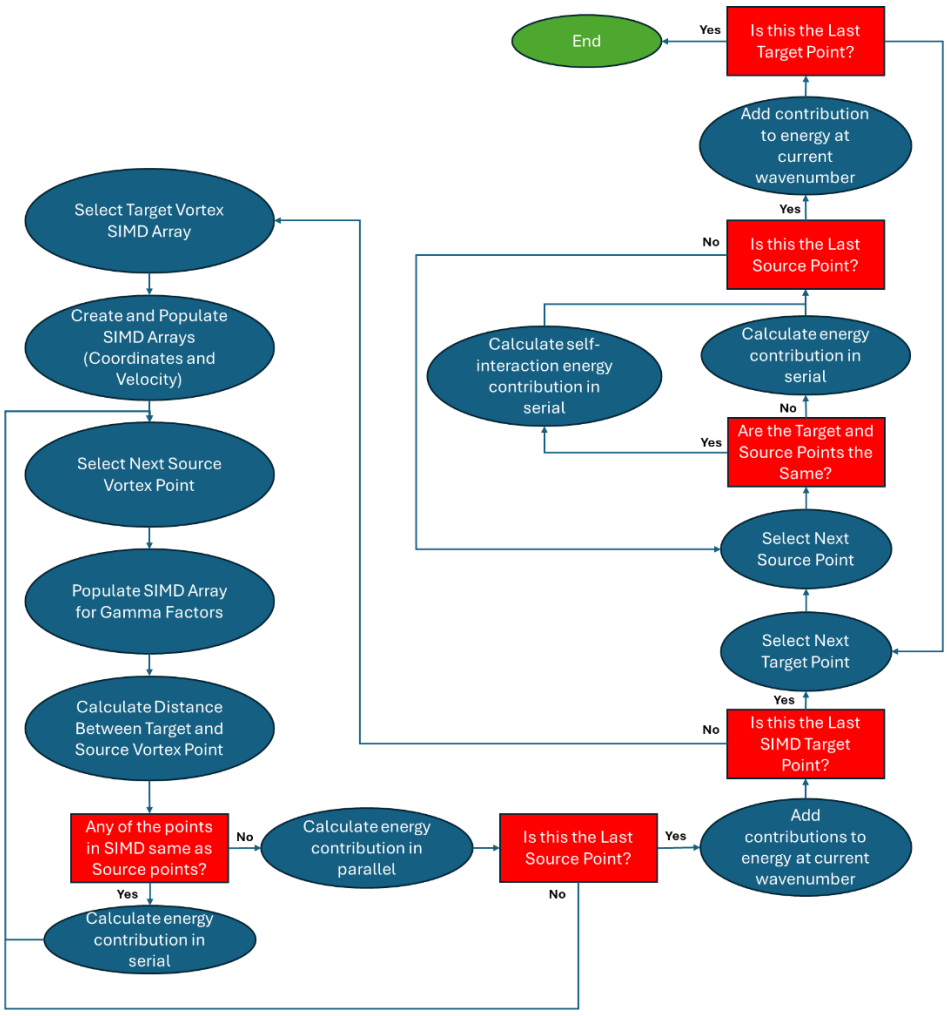

Fig. 17 - Information flow chart of the SIMD energy spectra algorithm.

4.2.6. High-Algebraic Smoothing Kernel

In order to retain numerical stability in my calculations, I had to include a smoothing kernel into my algorithms. Here, I will briefly go over the high order algebraic smoothing kernel that was used in the quantized vortex velocity algorithm in **Section 4.2.3**.

$$Q(\rho) = \frac{\left(\rho^2 + {}^5/_2\right)}{(\rho^2 + 1)^{5/2}} \tag{39}$$

Equation 35 shows the depiction of the high order Algebraic smoothing kernel by Winckelmans and Leonard in [78]. Here, ρ is defined as:

$$\rho = \frac{|\boldsymbol{X}_n - \boldsymbol{x}|}{\sqrt{\left(\sigma_{\boldsymbol{X}_n}\right)^2 + (\sigma_{\boldsymbol{x}})^2}} \tag{40}$$

Where $\boldsymbol{X}_n$ is the target vortex point, $\boldsymbol{x}$ is the source vortex point and σ is the core radius applied to the vortex filament. Note that the core radius is constant throughout the tangle length, therefore, the values of $\sigma_{\boldsymbol{X}_n}$ and $\sigma_{\boldsymbol{x}}$ are the same. Doing this applies a numerical core to the vortex filaments that smooths the results. As it was explained by Kivotides in [99], the cores that are given to the individual vortices (radial thickness σ) cannot deform and are constant throughout the entire length of the tangle. The tangle is given a numerical thickness only temporarily, which is removed once the smoothed velocity field has been calculated. This now introduces a variable in my system that must be well thought of: Too small of a smoothing core and the results would be prone to numerical instabilities, while too large of a smoothing core would remove any small-scale physics of the vortices like small Kelvin waves.

4.2.7. Gaussian Smoothing Kernel

There is another smoothing kernel that I used in the code, this time for the energy spectra calculation, called the Gaussian smoothing kernel [78]. This smoothing kernel is seen below as $Q(\rho)$:

$$Q(\rho) = \frac{1}{\rho^3}\left(\operatorname{erf}\left(\frac{\rho}{2^{1/2}}\right) - \left(\frac{2}{\pi}\right)^{1/2} \rho e^{-\rho^2/2}\right) \tag{41}$$

Here, the component "erf" is the Gauss error function, giving this way its name to the smoothing function, defined in [101]:

$$\operatorname{erf} x = \frac{2}{\sqrt{\pi}} \int_0^x e^{-t^2}\, dt \tag{42}$$

The Gaussian smoothing kernel is used for the Energy Spectra algorithm in **Section 4.2.5**, in both its serial and parallel form, and it can also be used in the serial Biot-Savart algorithm. Due to the nature of the kernel, when running in parallel and the target vortex point is the same as the source vortex point, extra steps had to be done, as shown in Fig. 17. Just like with

the High-Algebraic smoothing kernel explained above, the quantized vortices are given an artificial numerical core that is non-deformable and is constant throughout the tangle; it lasts only while the velocity field of the vortices is calculated, after which, the numerical core is removed from the system. Giving the vortices too large or too small of a smoothing core has the same effect on the results as in the High-Algebraic smoothing algorithm.

4.3. Desingularisation of the Biot-Savart Law

In the Biot-Savart equation shown in **Equation 24** you can see that there is a singularity when $\boldsymbol{X}_s = \boldsymbol{x}$, when the source point is the same as the target point, this means that the distance between the source and target vortex points becomes zero and the Biot-Savart integral diverges as the distance between the vortex points reduces. To fix this I had to use a renormalisation to calculate the local self-contribution to the vortex point's velocity, this renormalisation is mentioned by Schwarz in [42]:

$$
\begin{aligned}
V_{si_x} &= \frac{\kappa}{4\pi} ln\left(\frac{2\sqrt{(l_+ l_-)}}{a_0 e^{0.25}}\right)\left[\left(svds_y * svdds_z\right) - \left(svds_z * svdds_y\right)\right] \\
V_{si_y} &= \frac{\kappa}{4\pi} ln\left(\frac{2\sqrt{(l_+ l_-)}}{a_0 e^{0.25}}\right)\left[\left(svds_z * svdds_x\right) - \left(svds_x * svdds_z\right)\right] \\
V_{si_z} &= \frac{\kappa}{4\pi} ln\left(\frac{2\sqrt{(l_+ l_-)}}{a_0 e^{0.25}}\right)\left[\left(svds_x * svdds_y\right) - \left(svds_y * svdds_x\right)\right]
\end{aligned}
\tag{43}
$$

Where $svds$ and $svdds$ are the first and second derivatives of the curve with respect to the arc length, and subscripts x, y and z of $svds$ and $svdds$ denote the components in each respective direction. The directions of $svds$, $svdds$ and $svds \times svdds$ are tangent to the curve, normal to the curve and binormal respectively [42]; their respective magnitudes are 1, $1/R$ and $1/R$ [102] where R is the curvature radius. This is comparable to **Proposition 1.46** in Tapp's book [103], here the velocity vector $\boldsymbol{v}(t)$ is analogous to $svds$ and the acceleration vector is analogous to $svdds$. As I use arc length parametrisation, the equation in Proposition 1.46 in Tapp's book to calculate the curvature (C) of a curve is simply the cross-product between $svds$ and $svdds$:

$$
C = svds \times svdds \tag{44}
$$

This takes care of the singularity in the Biot-Savart equation, now numerical instabilities become the problem; for this I applied a finite numerical core to the quantized vortex filaments, excluding the singularity cases where the desingularisation method is used, using

either a High-Algebraic or a Gaussian smoothing kernel, these can be seen in **sections 4.2.6** and **4.2.7**. The resulting equation that is computed in my calculations can be seen below:

$$\boldsymbol{V}_s(\boldsymbol{x}) = -\frac{\kappa}{4\pi}\int_{\mathcal{L}_s} \frac{Q(\rho)}{(\sigma(\boldsymbol{X}_s)^2 + \sigma(\boldsymbol{x})^2)^{\frac{3}{2}}} d\xi \cdot \boldsymbol{X}_s' \times (\boldsymbol{X}_s - \boldsymbol{x}) \tag{45}$$

Here, $Q(\rho)$ depends on which smoothing kernel is selected, personally I used the High-Algebraic smoothing kernel for velocity calculations and the Gaussian smoothing kernel for the energy spectra calculations.

4.4. Time-step sizing

The main reason to know and understand the velocity of Kelvin waves is to decide a timestep size for the calculation. I use a condition that states that the chosen timestep needs to be able to resolve the fastest Kelvin waves; here the smallest (and therefore fastest) Kelvin waves have a wavelength equal to two times the discretisation distance of the tangles (Δx). Therefore, taking **Equation 29** and the wavelength of the smallest possible Kelvin wave gives us the expression for the timestep size (Δt):

$$\Delta t = svtires \frac{2\Delta x}{V_{wave}} \tag{46}$$

Here, $svtires$ is used to tune the timestep size for stability; in the case of all my calculations $svtires = 0.05$.

Having the information regarding how fast a Kelvin wave propagates along a vortex filament can be important in many ways; for the sake of this thesis, the Kelvin wave propagation velocity was used to determine which regime my quantized vortex simulations were, by looking at the simulation time and the propagation velocity. Kelvin waves also play an important part in the transfer of energy within vortex tangles, especially in isolated quantized vortices. I aim to study the signature of Kelvin waves in the energy spectrum, and how the energy is transferred from large scales to small scales.

4.5. Runge-Kutta Numerical Scheme

Numerical methods can be used to find approximations to the solutions of ODEs (Ordinary Differential Equations) [104], one of these numerical methods is the Runge-Kutta method, which by itself has many variations with different number of sub-steps and different coefficients which vary the accuracy and stability of the numerical method. In this section I will do a brief review of the general form of the Explicit Runge-Kutta method formula focused towards approximating a vortex point position, and the coefficients used for my research.

4.5.1. Runge-Kutta Method Generalisation

Runge-Kutta numerical methods are utilised for calculating the numerical solution of ordinary differential equations such as $\frac{dy}{dt} = f(t, y)$. They can approximate a value y_{n+1} at t_{n+1}, where $t_{n+1} = t_n + dt$, from a previous value y_n and the slope of the curve [105]. This approximation is given by **Equation 43** below:

$$y_{n+1} = y_n + dt \sum_{i=1}^{s} b_i v_i \tag{47}$$

Note that even though **Equation 43** is a generalisation for an explicit Runge-Kutta Scheme for any given number of sub-steps, the notation has been modified to fit the purpose of the research, y is the position of the vortex point in 3-dimensional space, dt is the timestep size, v is the velocity that is calculated by evaluating the Biot-Savart integrals, s is the number of Runge-Kutta sub-steps and b is a coefficient that decides the weight of each sub-step towards approximating the new vortex point position.

$$\begin{aligned} v_1 &= f(t_n, y_n) \\ v_2 &= f(t_n + c_2, y_n + (a_{21} v_1) dt) \\ v_3 &= f(t_n + c_3, y_n + (a_{31} k_1 + a_{32} k_2) dt) \end{aligned} \tag{48}$$

Note that if we limit the method to a single sub-step, the method being used would be Euler method. In our case, we do not want this as it struggles with accuracy and numerical stability.

4.5.2. Low-Storage Explicit Third-Order Runge-Kutta Method

A more efficient algorithm to integrate $\frac{dy}{dt} = f(t, y)$ was developed by Wray in [106] and it satisfies the following criteria explained by Orlandi in [107], note that I will use the notation employed in this thesis and not the original from Wray's work:

1. I need to approximate $y(t)$ for times t_0, t_1, t_2, …; these are defined as $t_1 = t_1 + dt$ and $t_2 = t_1 + dt$. The approximation of $y(t)$ to these times are called y_0, y_1, y_2,…
2. There are only two memory locations for each y.
3. $f(t, y)$ is stored in one of the memory locations.
4. If at the start of a given step n, the quantities stored at the memory locations are $a(t_n)$ and $b(t_n)$, then the memory locations must store $a(t_{n+1})$ and $b(t_{n+1})$ at the beginning of step $n + 1$ [106].

Following Criteria 1, one of the memory locations is reserved for y_n. As I am using a third order accurate Runge Kutta scheme, the scheme below is what is used to approximate the new value y_{n+1}. The scheme is structured in such a way that a separator is drawn, the variables on the left side of it are stored in the first memory location and the variables seen on the right side of the separator are stored in the second memory location. This scheme was developed by Wray in [106], but the notations have been changed slightly to accommodate the notations in this thesis.

$$\begin{aligned} & y_n \mid f_n \\ & y_{'} = y_n + a * dt * f_n \mid y_n + A * dt * f_n = y_A \\ & y_{''} = y_{'} + b * dt * f(y_A, t_n + A * dt) \mid y_{'} + B * dt * f(y_A, t_n + A * dt) = y_B \\ & y_{n+1} = y_{''} + c * dt * f(y_B, t_n + (a + B) * dt) \mid Empty \end{aligned} \tag{49}$$

4.6. Parallelisation Tests

In this section I discuss the results of parallelising the Biot-Savart integral and the energy spectra using the SIMD method discussed in **section 4.2.5**, the error introduced by this method and the acceleration achieved over the base, serial version of the code.

4.6.1. Error

It is possible that by accelerating the algorithms, both the Biot-Savart integral and the energy spectra algorithm, that some errors are introduced into the results; I have developed a small algorithm that compares the results for the same configuration at the same time in order to calculate how the parallel results deviate from the serial results. I did this in such a way that by activating an option in the input file, the algorithm would run this error test or not without the need for re-compiling.

To calculate the error being introduced I used the following simple steps. I calculate two values called p_{norm} and p_{diff}; p_{norm} is the result of adding the square of the velocity in every direction for every point, while p_{diff} is identical but taking into consideration the difference in speed between the parallel and the serial calculations.

$$p_{norm} = \sum_{i=1}^{N} v_x^2 + v_y^2 + v_z^2 \, , p_{diff} = \sum_{i=1}^{N} (v - w)_x^2 + (v - w)_y^2 + (v - w)_z^2 \tag{50}$$

Where N is the number of vortex points in the system, $v_{x,y,z}$ are the x, y and z components of the velocity calculated in serial and $w_{x,y,z}$ is the velocity computed in parallel. Now I can use these values to calculate the error.

$$Error = \sqrt{\frac{p_{diff}}{p_{norm}}} \tag{51}$$

After calculating the error for close to 90 thousand timesteps, I plotted this in a graph in order to visualize the results.

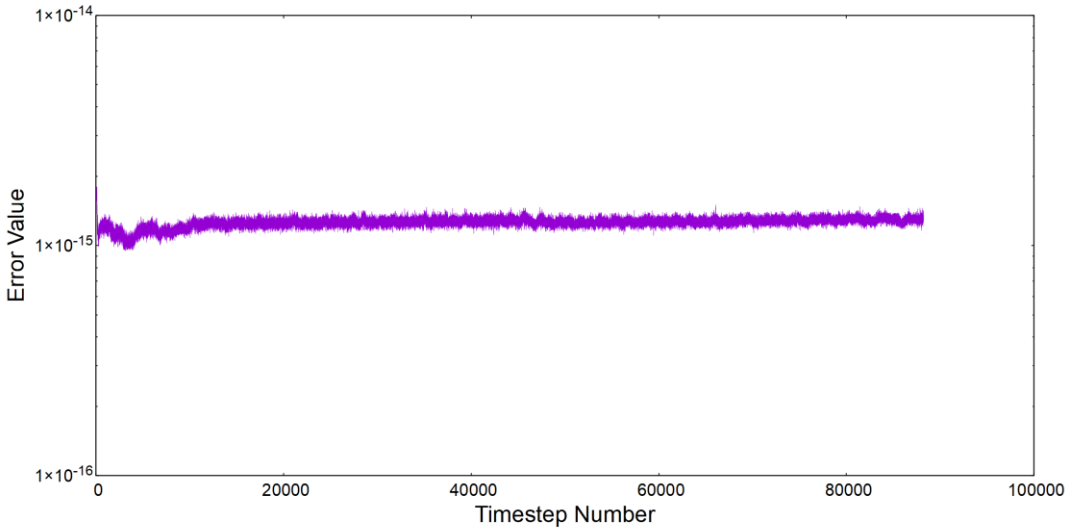

Fig. 18 - Graph showing that the error introduced by SIMD parallelisation is comparable to machine precision for a double precision decimal.

The error has a value of 10^{-15}, therefore I can say that the error introduced by my parallel algorithm is acceptable. Furthermore, I ran this error test for close to 90 thousand timesteps and throughout the entirety of the test the error value was stable, as seen in Fig. 18; therefore, I can consider that the error introduced is not of concern.

4.6.2. Acceleration Due to Parallelisation

I ran 5 different instances of the same simulation in serial and parallel varying only the number of discretisation points that define the vortices; this was done by increasing the resolution factor within the input file. I recorded the execution time for both Biot-Savart integral and energy spectra calculation independently, the results can be seen in Fig. 19.

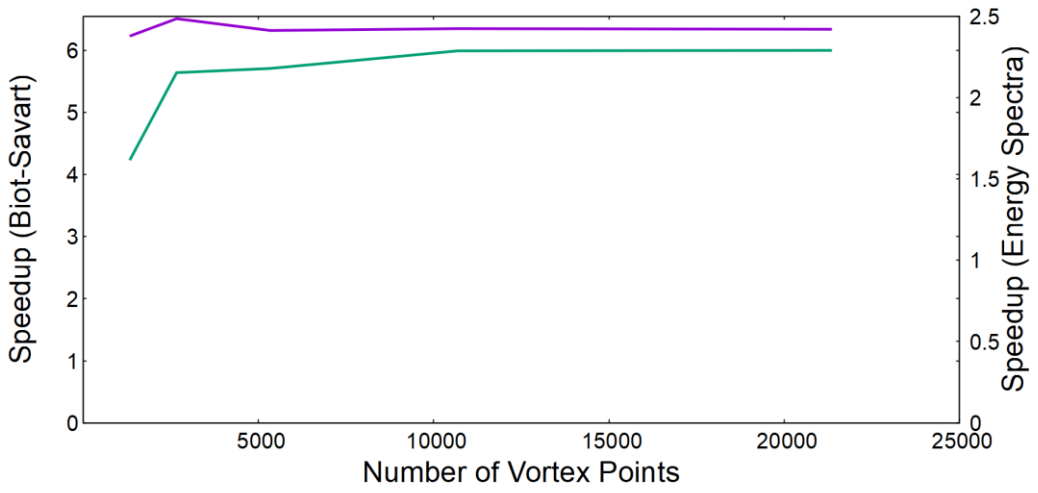

Fig. 19 - Execution acceleration from parallelising the Biot-savart (purple) and Energy spectra (green) algorithm.

Fig. 19 shows an acceleration in the algorithm execution, especially regarding the Biot-Savart algorithm. The execution acceleration achieved by parallelising the Biot-Savart algorithm is between 6.25 - 6.50. Fig. 19 also shows the acceleration in the energy spectra calculation, which is lower than the one achieved in the Biot-Savart calculation. The acceleration in the energy spectra execution stabilises at 2.3 at higher number of vortex points; the difference in acceleration in the energy spectra and Biot-Savart algorithms comes from the smoothing kernel used. The Biot-Savart algorithm uses a High-algebraic smoothing kernel, and the energy spectra algorithm uses a Gaussian smoothing kernel; these kernels are explained in **section 4.2**. Due to the difference in how they are calculated, I modified the algorithms in different ways for them to be compatible with the SIMD implementation. The Gaussian kernel involves the distance between points cubed as a denominator, therefore, extra operations were needed to correctly implement SIMD into the algorithm, this reduced the acceleration achieved.

5. Results

In this section I show the results regarding the evolution of quantized vortices and their energy spectra for isolated vortices (**section 5.1**), chaotic tangles (**section 5.2**) and vortex bundle configurations (**sections 5.3** and **5.4**) are presented.

5.1. Results for Isolated Vortices Configuration

My objective in this section is to study the energy spectra of isolated quantized vortices, spectral signature of the Kelvin wave regime and the spectral signature of energy equilibration in such a system. I know that in Navier-Stokes turbulence there is a $k^{-5/3}$ scaling in the energy spectra, which is usually associated with vortex stretching. I don't expect this law to appear in my results from this configuration because I am working with quantized vortices, and for vortex stretching to happen, there needs to be a reduction in the core thickness of the vortices; this does not happen in quantized vortices because they have a constant extremely thin core.

To study these phenomena, I generate a quantized vortex configuration consisting of 4 rings with a radius equals to 0.0415cm each and placed in such a way that each vortex ring is placed on the faces of an imaginary cube of length 0.0843cm; the vortices are placed pairwise on the cube faces in the X-Y plane and the X-Z plane. Fig. 20 shows how the vortices were generated in space. The pairwise vortices move in opposite directions which would make the vortices reconnect at 4 points; I allowed the vortices to reconnect when the distance between 2 discretisation points fell under 0.1ξ, where $\xi = 3.906 \times 10^{-4}\ cm$ is the discretisation length along the tangle. To ensure numerical stability I applied a smoothing core $\sigma = 3.3\xi$, which allowed the simulation to compute small scales while maintaining numerical stability. I carefully inspected the tangles throughout the calculation to ensure that there were no waves prior to the reconnections and that there were no waves at the grid level (zig-zag instability); therefore, even if the vortices appeared corrugated, I checked that the wiggles are physical and not numerical.

I calculate 2 characteristic times corresponding to small and large scales to scale the time. The first characteristic time involves the time at which the fastest Kelvin waves start to interact with each other, this being $t_{small} = 0.03734s$. The second characteristic time is determined by the time at which the slowest Kelvin wave does a full lap around one of the

structures that are formed after the initial reconnections; $t_{large} = 35$s. All times for this configuration will be both in characteristic times, t_{small} and t_{large} between brackets.

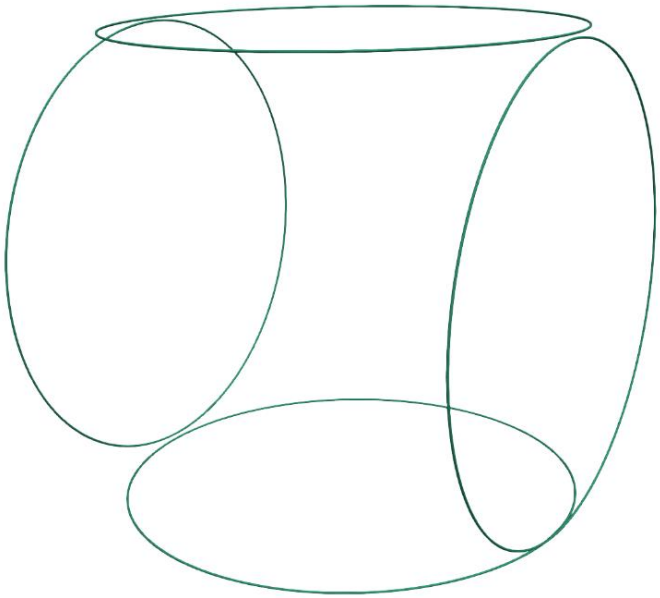

Fig. 20 - Quantized vortices in a cubic configuration at t=0

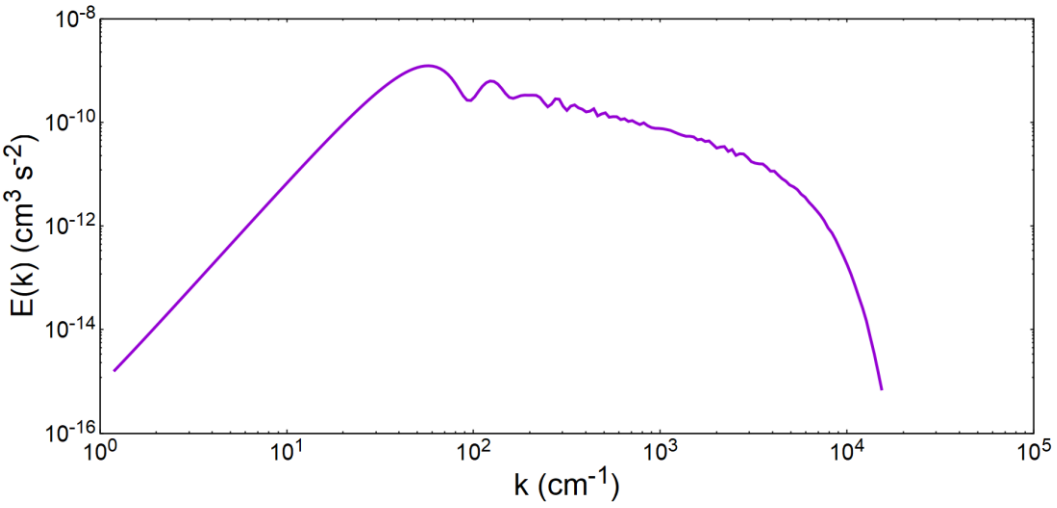

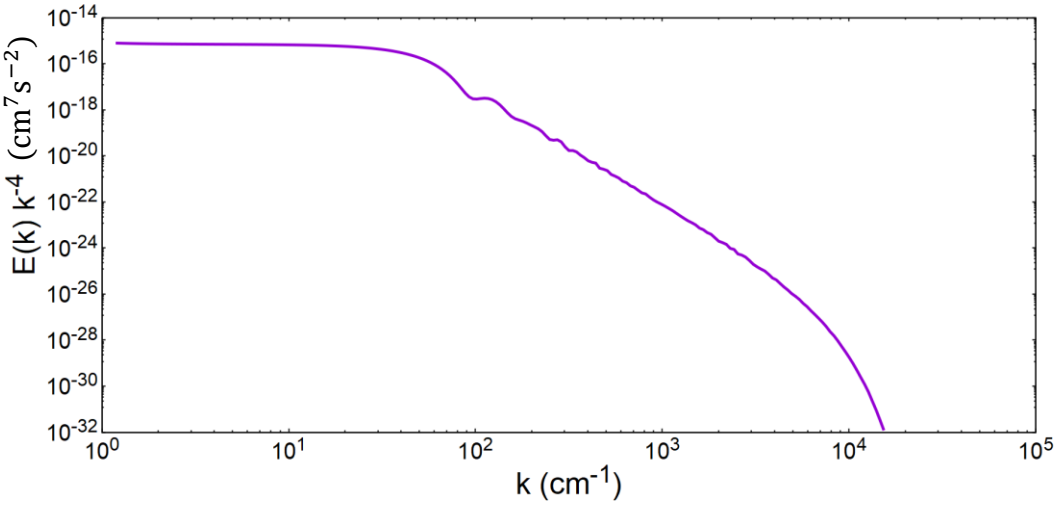

Fig. 21 - Energy spectra of the isolated tangle configuration at t=0 (top) and multiplied by k^{-4} (bottom).

Fig. 21 shows the energy spectrum of the isolated vortex tangle configuration at $t = 0$, it also shows a flat spectrum at low k-values when multiplied by k^{-4}; this means that in the initial conditions the net impulse of the rings is equal to zero, because the rings are set-up in pairs that move in opposite directions at the same velocity.

5.1.1. Kelvin wave velocities and regimes.

This vortex configuration has 4 distinct regimes, some of which are more distinguishable than others, and have their own dynamics. Before determining the different regimes in the simulation, I need to calculate the velocities of the fastest and slowest Kelvin wave. Following the equation in **Section 2.2.9**, the fastest Kelvin wave is the one with the smallest wavelength, this is equal to 2 times the discretisation length of the tangle; in this case the smallest Kelvin wave would have a wavelength equal to $7.8125 \times 10^{-4}\ cm$ and a velocity of $5.724\ cm\ s^{-1}$. On the other hand, the slowest Kelvin wave would have a wavelength equal to the perimeter of one of the structures that form after reconnection, which is approximately the circumference of 2 of the original vortex rings. This gives a wavelength equal to $0.5215\ cm$ and a velocity of $0.0148\ cm\ s^{-1}$.

Regime 1 starts at t=0.0s and ends just before the initial 4 reconnections happen between the vortices; this happens at $t = 0.6034 t_{small}$ ($6.437 \times 10^{-4} t_{large}$). In this regime, the opposite rings travel towards each other, and there should be no new waves being generated in the tangle. If this was the case, then the results would be void as there would be numerical

instabilities in the results. Fig. 22 shows that the vortex rings have deformed slightly because of the presence of the other vortices.

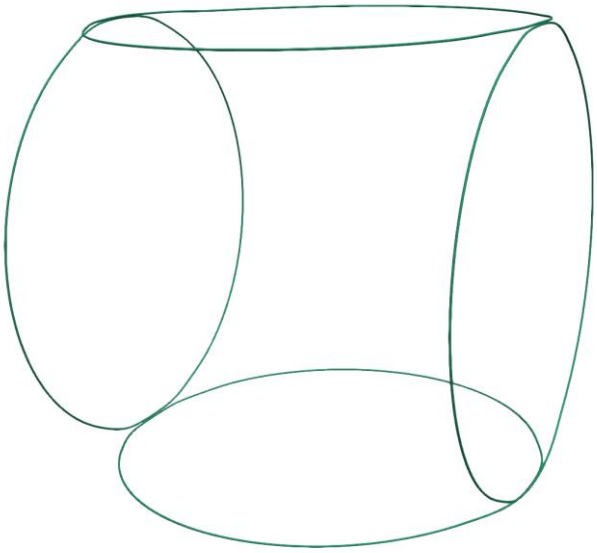

Fig. 22 - Cubic configuration at the end of regime 1.

Regime 2 starts when the vortex rings reconnect, this happens at $t = 0.6947 t_{small}$ ($7.411 \times 10^{-4} t_{large}$). These reconnections create 2 distinct structures which have 4 different regions of high curvature each, these high curvature regions generate Kelvin waves that move away from this region; this can also be seen in other papers with similar (4 reconnecting rings in a "cubic" configuration) numerical calculations, like in the work by Kivotides et al. [39], and in other numerical calculations where the configuration is not as similar, like in the work by Zhu et al. [63] where two vortex rings travel in the same direction, or in the work by Araki and Tsubota [111] where there is a collision between a vortex ring and straight line vortex. The reconnections create a high curvature region (kinks) which later generate Kelvin waves that travel along the vortex filament. This regime ends when the fastest Kelvin waves from opposite sides are about to superpose each other at the mid-point between their origins along the filament length. To approximate at what point in time this happens, I use the velocity of the fastest moving Kelvin wave and a quarter of the circumference of the original vortex rings as the length. This means that the fastest Kelvin waves are about to superpose at the same time as regime 2 ends at $t = 1 t_{small}$ ($1.067 \times 10^{-3} t_{large}$). Fig. 23 shows the state of the tangle at the start and end of regime 2.

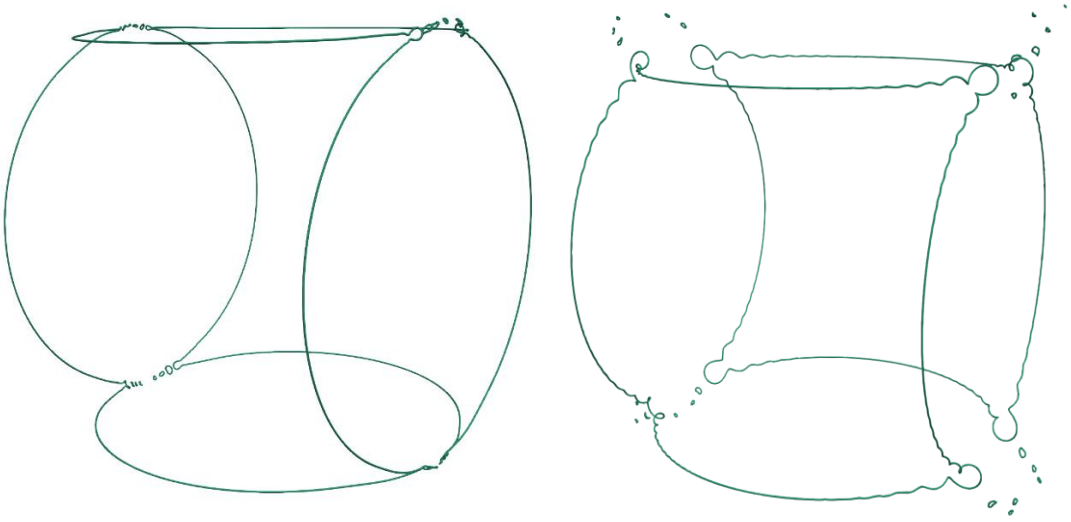

Fig. 23 – Cubic configuration at the start (left) and end (right) of regime 2.

Regime 3 starts when the Kelvin waves start to interact with each other by superposition; this happens starting approximately from $t = 1t_{small}$ $(1.067 \times 10^{-3} t_{large})$. When the Kelvin waves are superposed with each other, small scales are created and an energy transfer happens from large to small scales, this is called energy cascade; I will go into it more deeply later. This regime is characterised by the interaction and superposition between differently sized Kelvin waves and by the subsequent energy transfer to smaller scales. I define this regime to end approximately when the largest Kelvin wave travels a distance along the filament equal to twice the perimeter of one of the structures (or the total tangle length of the 4 vortex rings at initial conditions). Therefore regime 3 would end approximately at $t = 1874.67t_{small}$ $(2t_{large})$.

Regime 4 starts when regime 3 ends and continues in time indefinitely. In this regime energy in the large and small scales is equilibrated, this involves many interactions of the slowest Kelvin waves. This is a process that requires an extensive amount of time to reach the last regime. I can stop the calculation when I see energy equilibration; this could require approximately half a dozen of the slowest Kelvin wave times. I have results up to a point in time within regime 3, but these results are enough to show a clear Kelvin wave cascade and a portion of the spectral signature of the energy equilibration.

5.1.2. Energy spectra in regimes 1 and 2.

Here I will study the energy spectra at t=0.0s, at the end of regime 1 (prior to reconnections), at the start of regime 2 (just after reconnections) and at the end of regime 2 (prior to Kelvin

wave interactions) and see if the reconnections and generation of Kelvin waves affect the shape of the energy spectra.

Prior to this I will investigate the shape of the energy spectra of this configuration (4 rings at opposite faces of an imaginary cube) at the initial conditions (t=0s).

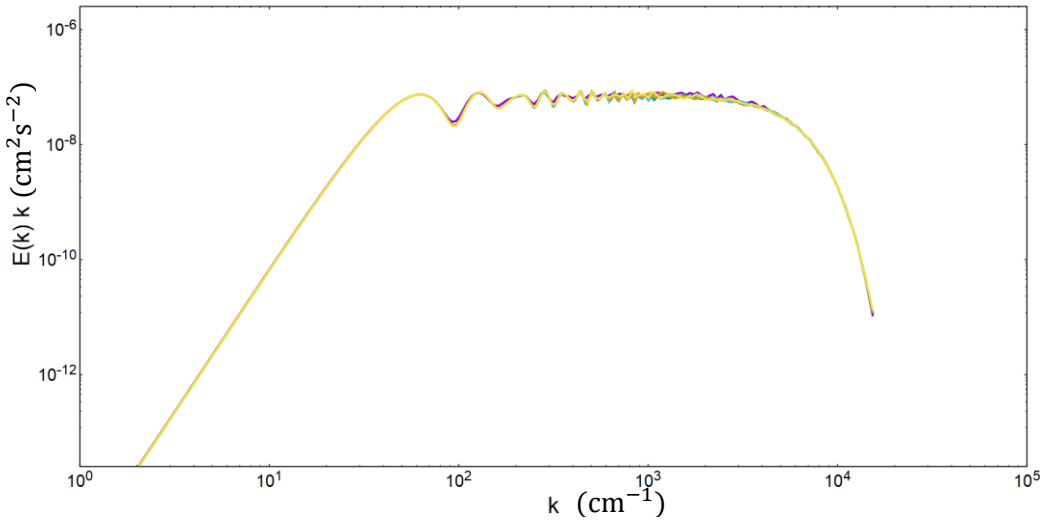

Fig. 24 - Energy spectra of the cubic configuration at t=0 (purple), t=0.9322 (green), t=1.0054 (blue), t=1.0967 (orange) and t=1.2775 (yellow). All show a k^{-1} scaling at intermediate values of k. These times correspond to regimes 1 and 2.

Fig. 24 shows the energy spectra at different times within regime 1 and regime 2. I show the energy spectra at initial conditions as well as right after the reconnections happen, as Kelvin waves propagate along the tangle and just before the Kelvin waves superpose. Therefore, these results correspond solely to the effect of the initial reconnection and not the Kelvin wave cascade. At all times, the spectra have have a k^{-1} scaling at intermediate and large wavenumbers, this suggests that the initial reconnections and the Kelvin wave cascade do not have an effect on the energy spectra scaling and have a k^{-1} spectrum; this is consistent with the results of Kivotides et al. shown in [39].

5.1.3. Energy cascade.

In this section I study the effect of Kelvin waves colliding and interacting with each other; I focus solely on a portion of regime 3. I will show many energy spectra plots and their corresponding vortex tangle configurations to compare how the corrugation of the tangle is displayed on the energy spectra plot. For these energy spectra calculations, I used a diagnostic core $\sigma_{diag} = 0.5\xi$ to get an insight into the energy at small scales.

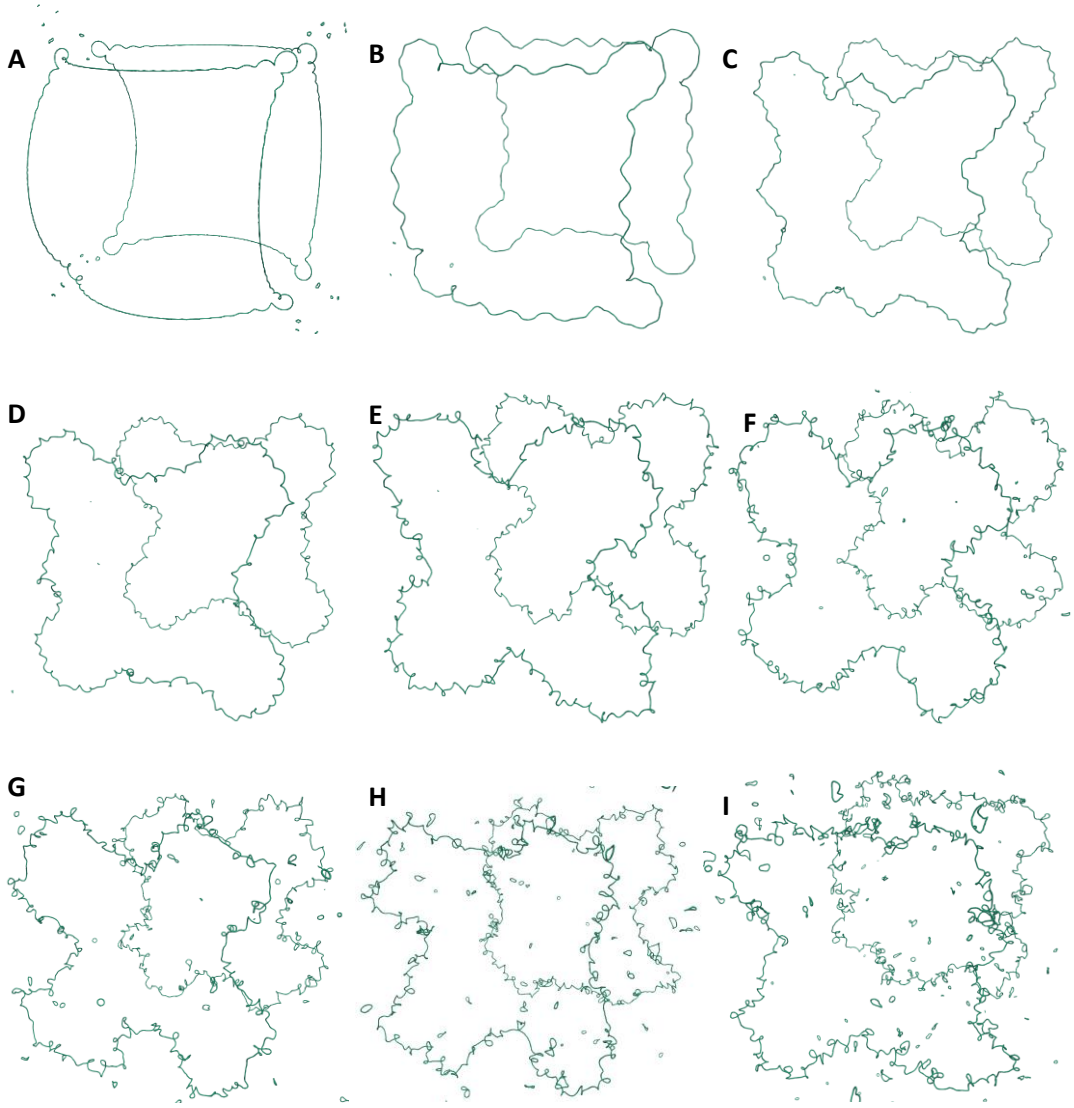

Fig. 25 - Cubic configuration at t=1.0970 (A), t=2.7397 (B), t=5.4847 (C), t=8.0442 (D), t=12.2491 (E), t=17.1853 (F), t=20.1106 (G), t=26.1437 (H), t=36.3818 (I).

Fig. 25 shows the quantized vortex tangle at 9 different times within regime 3. The Kelvin waves generated from the initial reconnections propagate along the vortex tangle and superpose with other Kelvin waves. This creates smaller waves (smaller scales) that also go on to superpose with the other Kelvin waves, creating even smaller waves; this continues until it reaches the scale of the fastest Kelvin waves due to the resolution constraint. The vortex tangle eventually becomes very corrugated, as seen in Fig. 25 (I), this is because in my model there is no normal fluid and therefore no mutual friction to dampen the Kelvin Waves; this agrees with Kivotides et al., Tsubota et al. work [39,97]. These small scales on the tangle can make it reconnect with itself, generating small rings. I will present the effect of small rings on the energy spectra in the next section. Again, I want to stress that even though the tangles

are visibly corrugated, I have checked the tangles thoroughly and no numerical instabilities (zig-zag instabilities) were present.

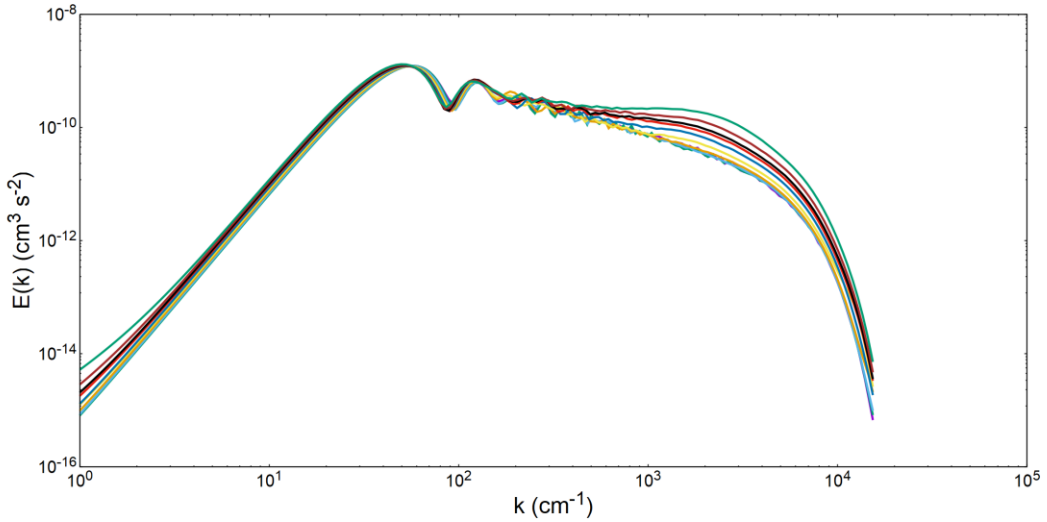

Fig. 26 - Energy spectra at t=0 (purple) t=1.0970 (green), t=2.7397 (light blue), t=5.4847 (orange), t=8.0442 (yellow), t=12.2491 (dark blue), t=17.1853 (red), t=20.1106 (black), t=26.1437 (brown), t=36.3818 (dark green)

Here I compare the energy spectra at $t = 0$ with all the times shown in Fig. 26. At $t = 1.097\ t_{small}$ ($0.001168\ t_{large}$) when scaled with large scale characteristic time) and $t = 2.740\ t_{small}$($0.002923\ t_{large}$), the energy spectra shape does not vary much from the initial conditions; this is understandable because when checking their corresponding tangles, the interaction between Kelvin waves has not created many small scales on the tangle (corrugation) and therefore not much energy has been transferred to said small scales. On the other hand, if we check the later times (both on the energy spectra and tangle snapshots), as corrugation and smaller scales start to appear on the tangle, there is a progressive energy transfer to smaller scales (energy cascade), changing the energy spectra shape; this transfer of energy from large scales (small k) to small scales (large k) is also mentioned by Araki and Tsubota [111].

5.1.4. Effect of small rings on the spectra.

Before trying to find out the spectral signature of energy equilibration in the tangle, I want to discuss the possible effects of the generation of small vortex rings on the energy spectra. To do this I compare the energy spectra of two similar cubic configurations, the only difference between them is that one configuration allows all reconnections to happen, while the other

one allows only the initial 4 reconnections that happen at the start of regime 2. In this case I used a diagnostic core $\sigma_{diag} = 0.25\xi$, this time I used a smaller diagnostic core because I wanted to have information about the energy at even smaller scales to check if small rings had any effect on it.

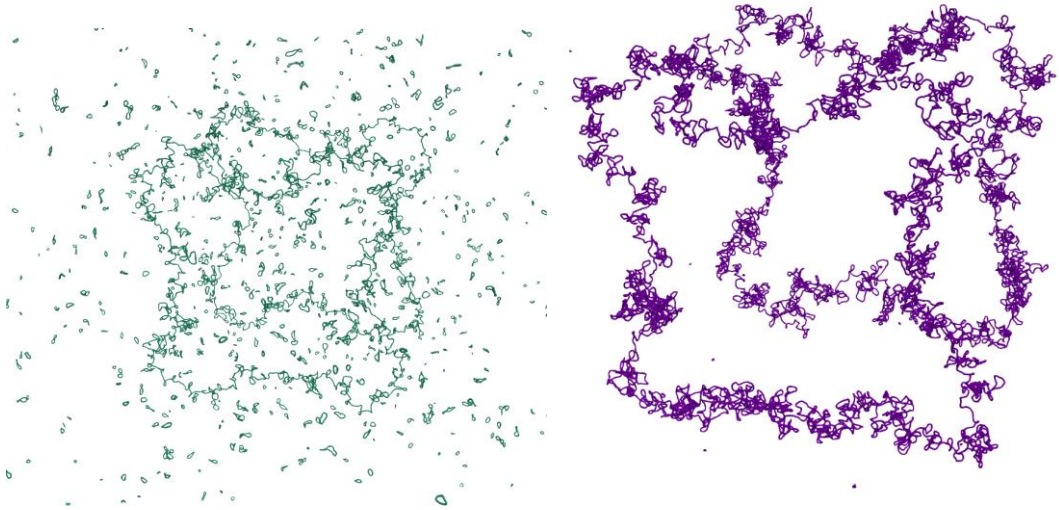

Fig. 27 - Cubic tangle configuration at t=20.11 when reconnections are allowed (left) and disallowed (right).

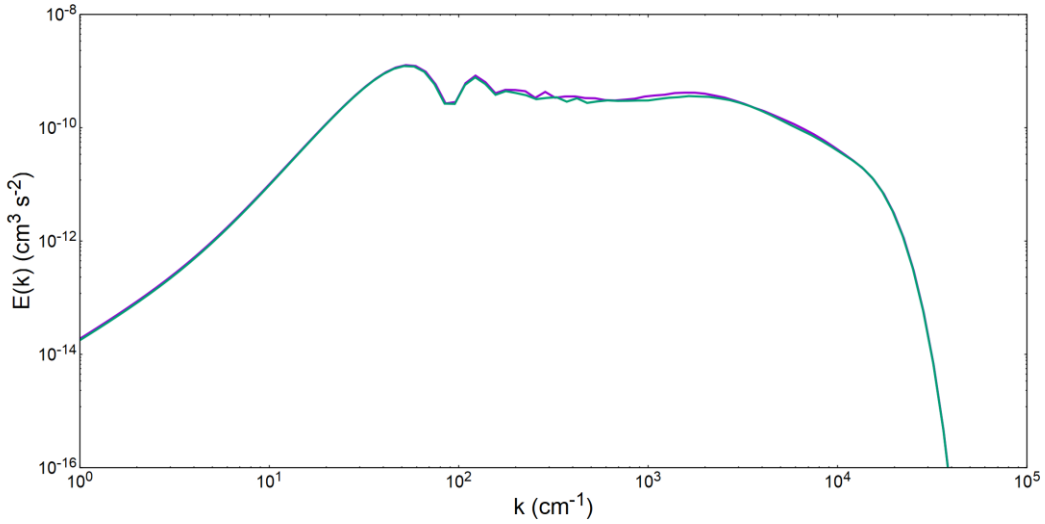

Fig. 28 - Energy spectra at t=20.11 for allowed reconnections (green) and disallowed reconnections (purple).

Fig. 27 (left) shows the tangle at t= $20.11\, t_{small}$ ($0.02145\, t_{large}$) with allowed reconnections when discretisation points came closer than 0.1ξ; Fig. 27 (right) shows the tangle at the same point in time but with the reconnections disallowed. There is a considerable difference between the tangles just from the fact that one allows reconnections, and the other does not; the reason for this is that the self-reconnections generate small rings

that remove the small scales from the tangle itself, making it smoother. This is why the tangle in Fig. 27 (right) is much more perturbed than Fig. 27 (left), where the tangle is much smoother. Now the question that arises is, will these small rings affect the shape of the energy spectra?

Fig. 28 shows the energy spectra for both cases (allowed/disallowed reconnections) and it shows that there is relatively no discernible difference between the shape of the spectra of the two cases. One could even say that there is a slightly more pronounced energy transfer to small scales when reconnections were disallowed. This suggests that the generation of small rings from reconnections of a larger system has close to no effect on the energy spectra shape; this could probably be because the small rings are like small scale Kelvin waves, so when they reconnect and leave the main tangle they cannot equilibrate. This result will become more important in **section 5.1.5**.

5.1.5. Energy equilibration.

The question now is, if the quantized vortices are allowed to develop further, what would the shape of the energy spectrum be, or what would it tend towards? As time progresses the vortices equilibrate the energy by transferring it to small scales, this is done by the large number of waves at small scales that are on the tangle at this point in time; this is shown in Fig. 29.

Each wavenumber k corresponds to a sphere in harmonic space, with surface area $A = 4\pi k^2$, and according to the definition of the energy calculation that I use, the energy is the integral over the sphere's surface of a particular wavenumber. If energy completely equilibrates, the energy per unit area on the spheres' surface is equal for all values of k. Therefore, for larger k (larger surface area), the value of total energy is higher and for smaller k (smaller surface area), the value of total energy is lower; but energy per unit surface area across all values of k are equal.

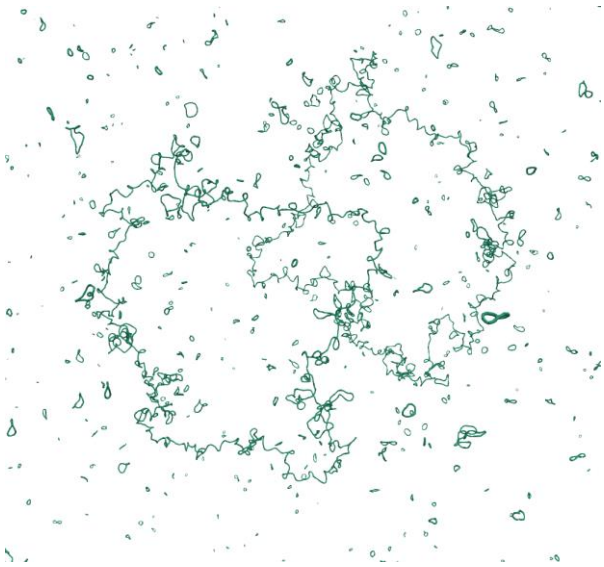

Fig. 29 - Cubic tangle configuration at t=82.82 showing many small rings together with small scales on the large tangle.

When I let the quantized vortices develop further, the vortex tangle becomes more corrugated, as shown in Fig. 29. I calculated the energy spectra for progressively increasing times to see the effect of energy equilibration on the shape of the spectra, this is shown in Fig. 30.

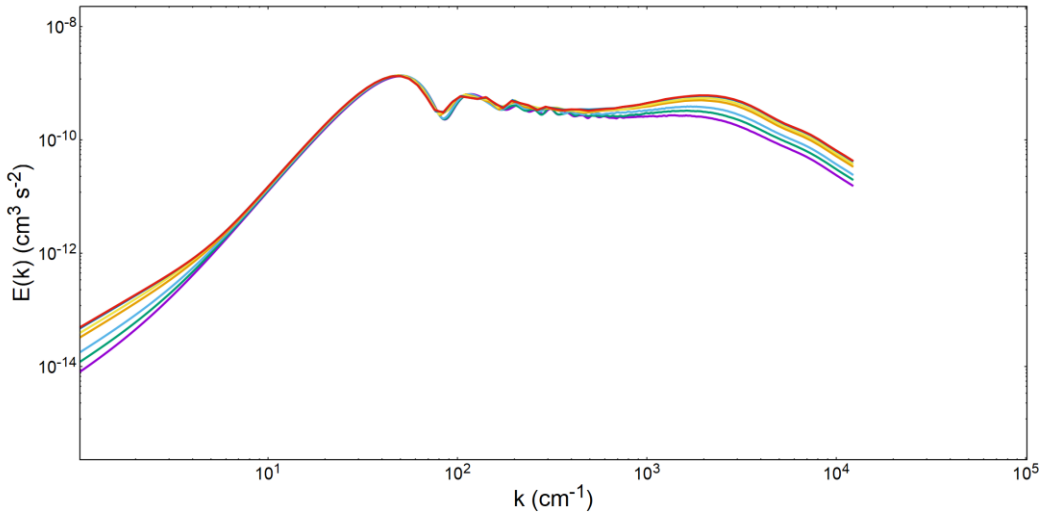

Fig. 30 - Energy spectra of the cubic tangle configuration at t=43.51 (purple), t=51.01 (green), t=58.32 (blue), t=71.48 (orange), t=76.24 (yellow), t=81.54 (dark blue) ,t=82.82 (red).

Fig. 30 shows how as time passes, the continuous transfer of energy to small scales makes the spectra shape to surpass the flatness found in Fig. 26. This increase in the "bump" shows no symptoms of stopping, but it is a very slow process. The shape of the spectra at t= $82.82\ t_{small}$ ($0.089\ t_{large}$) presents a scaling of $k^{0.6}$, as seen in Fig. 31; this is not the k^2

scaling that was described earlier, but this result suggests that when energy is equilibrating, the energy spectra scaling, rather than staying flat, continues increasing towards k^2.

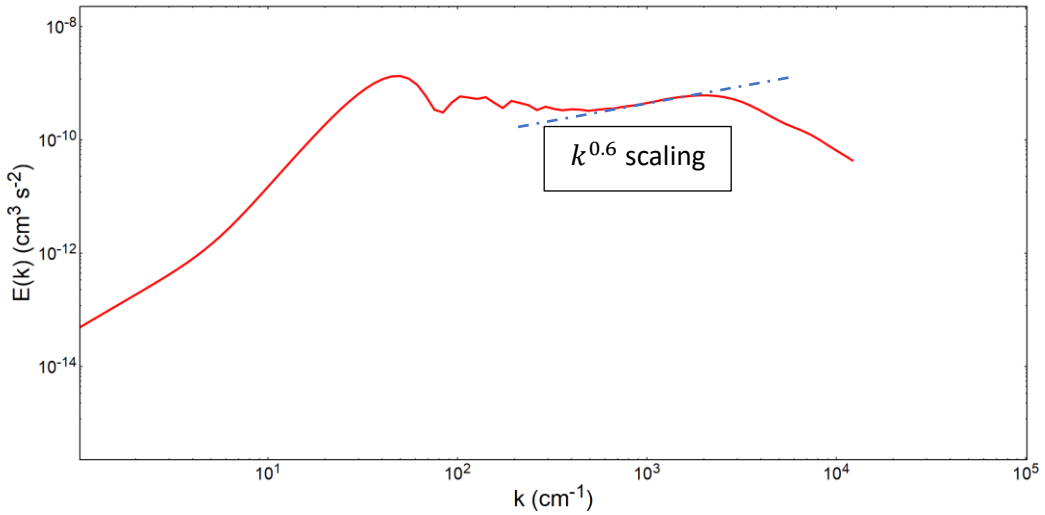

Fig. 31 - Energy spectra of the cubic tangle configuration at t=82.82 showing a $k^{0.6}$ scaling at intermediate to large values of k.

One could argue that the increase in energy at larger values of k comes from the small rings being generated by vortex reconnections, but as discussed in **section 5.1.4**, the small rings hinder the process of equilibration, so I can attribute the increase in the scaling to the process of energy equilibration.

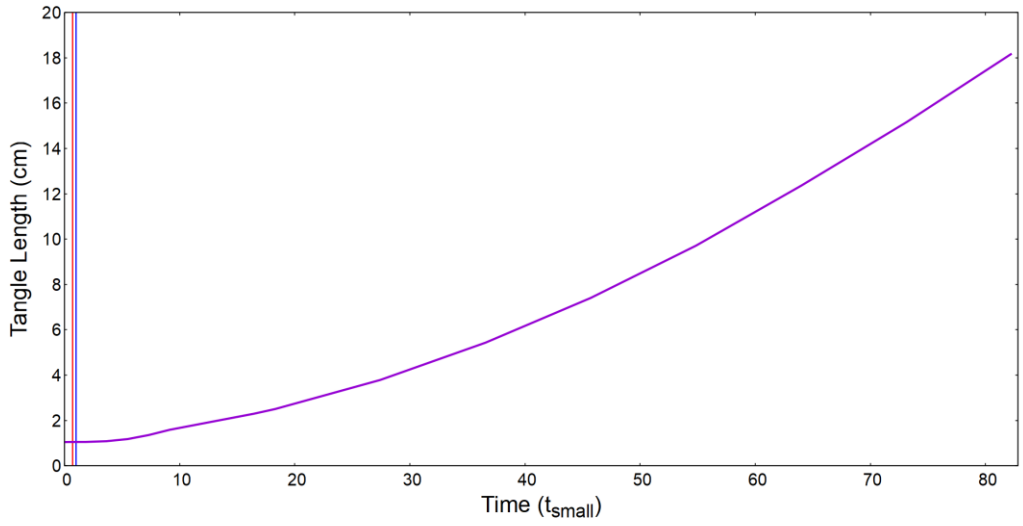

Fig. 32 – Graph showing the total tangle length against time scaled with t_{small}. The red line depicts the start of regime 2 (and therefore the end of regime 1) at t=0.6947 t_{small} and the blue line depicts the start of regime 3 (and therefore the end of regime 2) at t=1 t_{small}.

Fig. 32 depicts the total tangle length plotted against scaled time and shows that the total tangle length continuously grows throughout the entire calculation. This continuous growth of the tangle length (and a consequent addition of vortex points into the tangle when the separation between neighbouring vortex points increases over a set value) is due to the fact that fluid particles, even if they were neighbours, separate as the motion inside the fluid continues, as explained by Tsinober in [112].

5.2. Results for Chaotic Tangle Configuration

I know that the energy spectra is the integral over the surface of spherical shells in harmonic space with radius k [77], where k is the wavenumber defined as $k = 1/l$ and l is a length scale. As the surface area of a sphere in proportional to the square of its radius, it is hypothesised that as energy is being transferred to small scales, there is a process of energy equilibration, and that once the energy is completely equilibrated, the shape of the energy spectra would have a scaling of k^2. The energy equilibrates because at long times the energy cascade generates a bottleneck at high wavenumbers which later "spills" into a $k^{-5/3}$ pipeline related to the local-interaction regime; the reason behind the bottleneck is that the capacity of the $k^{-5/3}$ regime to cascade energy to small scales is smaller than that of the reconnection induced cascade. In this section my objective is to complement the results in **section 5.1** and to look for an indication that suggests energy equilibration in a system regarding a number of quantized vortex rings randomly oriented and positioned in space, but also to see if the presence of many rings affects the conclusion of the isolated vortices calculation.

The vortex configuration in this section consists of 100 quantized vortex rings placed and oriented randomly in 3D space inside a periodic box with size 0.1cm. This is a different boundary condition compared to the other configuration in this thesis; here when a vortex point exits the box on one side, it appears at the opposite side of the box. All rings have a random radius size between $0.99 * 0.02 = 0.0198cm$ and $0.75 * 0.02 = 0.015cm$, this gives an average vortex ring radius size equal to $0.0174cm$. The quantized vortices are discretised in such a way that the discretisation length is $\xi = 7.8125 \times 10^{-4}cm$ which results in a total number of 13875 vortex points; Fig. 33 shows the initial position of the quantized vortex rings in 3D space. To ensure the numerical stability of the system, I gave the quantized vortices a smoothing core radius equal to $\sigma = 2.57813 \times 10^{-3}cm$, and to ensure stability I closely checked for zig-zag instabilities and waves being generated without reconnections happening. Regarding the vortex reconnections, I allowed reconnections when vortex points

came closer than 0.3ξ, this reconnection threshold was kept constant throughout the whole calculation. I have made other calculations where the reconnections were disabled after some reconnections have happened to see the effect of this on the energy spectra.

I defined the characteristic length of the system as the average circumference of the quantized vortex rings at the initial conditions, this being $0.1093cm$. For the characteristic time for small scales t_{small}, I used the time taken for the slowest Kelvin wave to travel around the perimeter of the tangle once. This Kelvin wave has a propagation velocity of $0.0634\ cm\ s^{-1}$, this would result in a small-scale characteristic time $t_{small} = 1.724s$. I also defined a characteristic time for large scales, t_{large}, this involved the approximate time that the average sized vortex would take to travel the box from one side to the opposite two times. This makes $t_{large} = 2.743s$. All times in this chapter are in terms of both t_{small} and t_{large}, t_{large} being depicted between brackets.

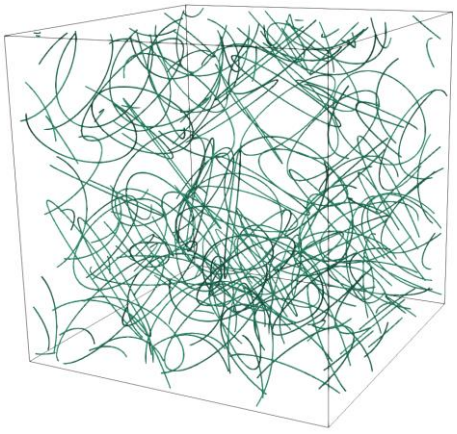

Fig. 33 - Chaotic tangle configuration at t=0.

5.2.1. Incorrect numerical core size.

In this section I am going to briefly discuss the effect of a small numerical core on the numerical stability of the quantized vortices in the same chaotic configuration described in **section 5.2**. In this case, all parameters have been kept the same except the numerical core radius, now it has a value $\sigma = 4.2969 \times 10^{-4}cm$; this value is 6 times smaller than the stable value that was used in the rest of this results section. Below is a zoomed-in section of the chaotic tangle after it was allowed to evolve.

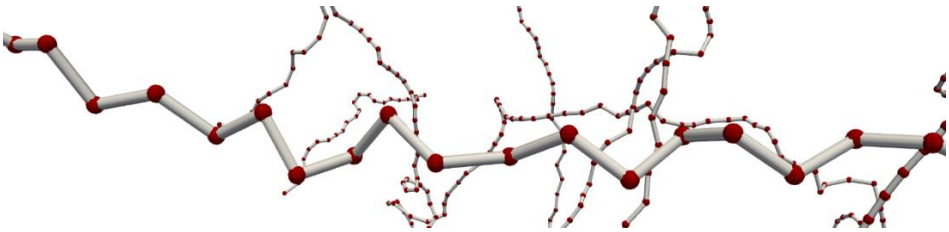

Fig. 34 - Numerical instability in the form of a zig-zag instability at the scale of the discretisation of the vortex tangle. This is due to the smoothing core being too small.

The image shows that there are waves at the level of the discretisation grid, these are called zig-zag instabilities, and these are symptoms of a numerically unstable calculation. Therefore, all the results extracted from this configuration are void and deemed unphysical. For the rest of the calculations, I thoroughly inspected the tangles to make sure that this zig-zag instability was not present at any time.

5.2.2. Energy cascade.

In this section I study the effect of the Kelvin waves (making sure that all the waves in the system are due to reconnections) interacting with each other on the energy spectra; very much like in **section 5.1**, but in this case the number of reconnections is much higher due to the position of the vortices and the nature of the configuration. To start, let's see the energy spectra shape of the initial conditions; here I used a diagnostic core radius $\sigma_{diag} = 0.25\xi$.

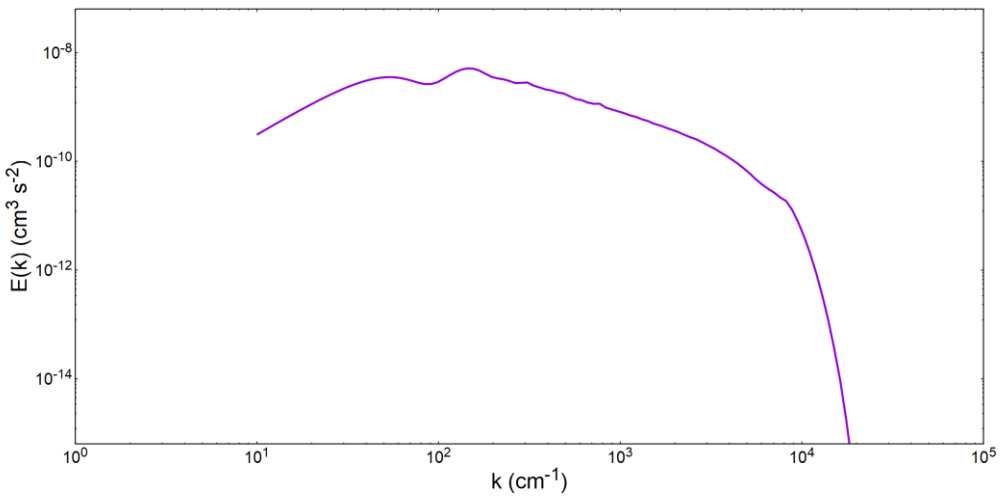

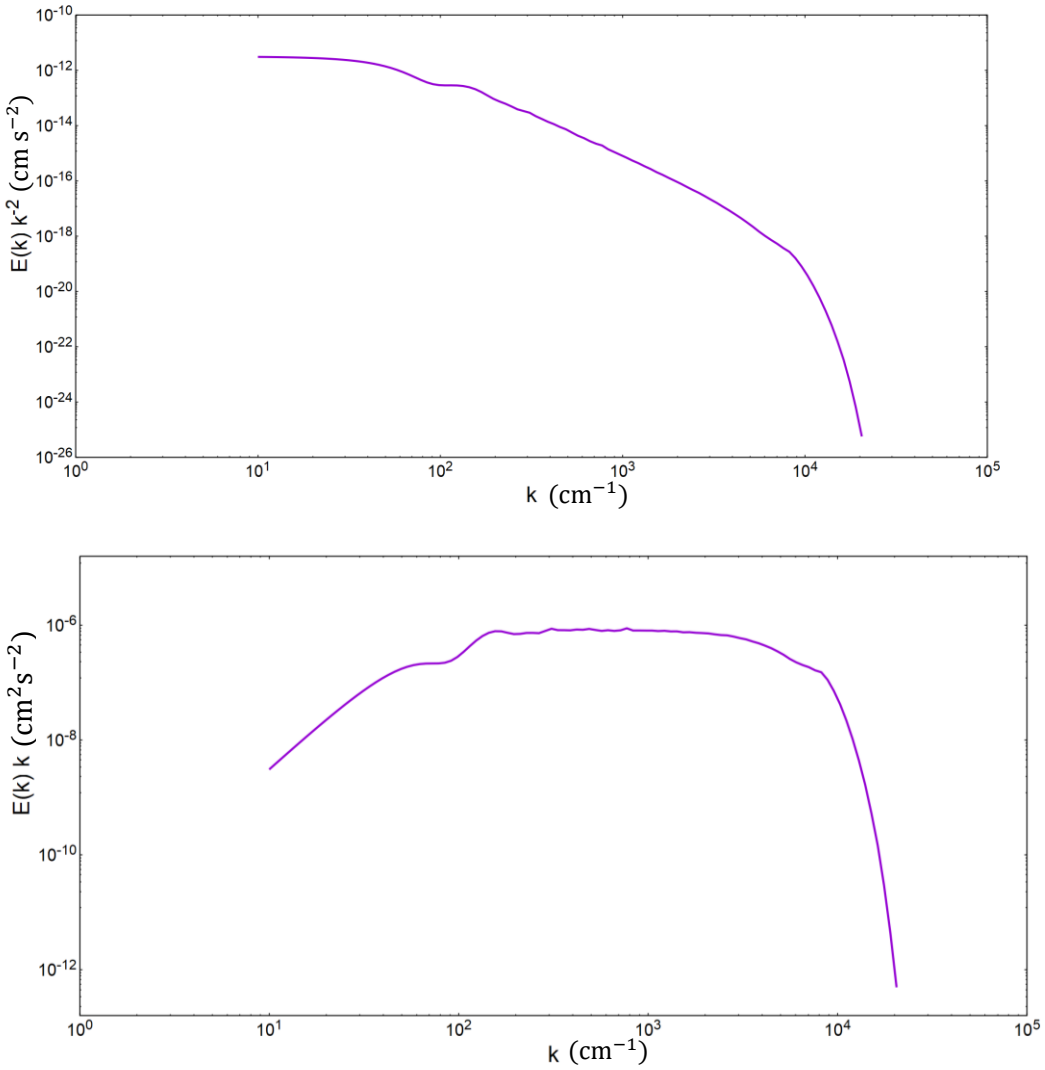

Fig. 35 - Energy spectra of the chaotic tangle configuration at t=0. I use no scaling (top), k^{-2} (middle), k (bottom) in the Y-axis.

The first thing that comes to mind is how short the small k regime of the spectra is, this is because I am using a periodic boundary condition and therefore the largest scale (smallest wavenumber) possible is the size of the periodic box. As mentioned before, the box size is 0.1cm, which corresponds to the smallest k in the spectra, $k = 10$.

From Fig. 35 (middle) you can see that the small k regime of the spectra has a k^2 scaling that comes from the linear impulse of the configuration being non-zero [77,113]. On the other hand, in Fig. 35 (bottom) you can see a clear k^{-1} scaling in the large k regime that comes from isolated vortices [77,113].

Knowing the shape of the spectra at t=0.0s, let us see how the vortex rings evolve in time, being free to reconnect with each other. Below is as series of snapshots of the tangle configuration for several times, including the last calculated time.

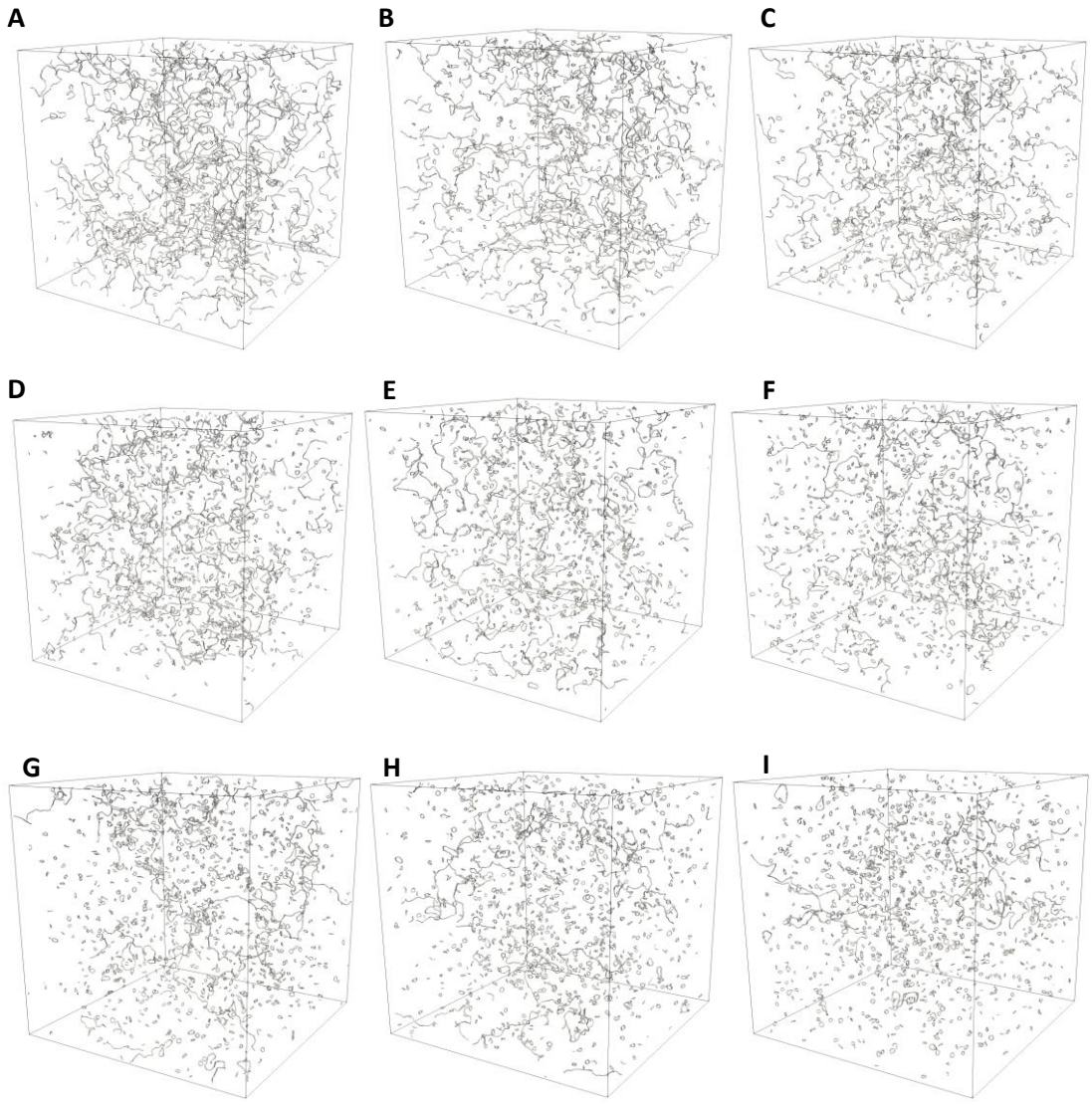

Fig. 36 - Chaotic tangle configuration at t=0.4411 (A), t=0.7351 (B), t=1.1762 (C), t=1.4703 (D), t=2.0437 (E), t=2.8964 (F), t=4.4108 (G), t=7.7042 (H), t=14.2321 (I).

You can visually detect that in this configuration there are many more reconnections happening compared to the cubic configuration; the number of reconnections as time passes is shown below in Fig. 37 (top). The reconnections early in the calculation happen more

frequently, most probably because the vortex line density is quite high, but then slows down at $t = 4\ t_{small}$. The total tangle length in the system can also be seen in Fig. 37 (bottom), the tangle length slightly increases at the beginning of the calculation but once the reconnections take over the simulation (as seen in Fig. 37 (top)) the total tangle length starts to decrease steadily. This is because when quantized vortices reconnect, they emit a sound wave, resulting in an energy loss from the tangle, therefore due to the reconnection algorithm that I use, the tangle length loss is a proxy for the energy lost at reconnection, as measured by Leadbeater et al. in [62]. Another important dissipation mechanism, and the most important, of superfluids is the sound emission due to very high k Kelvin waves (these are irrespective of vortex reconnections); this was modelled by my numerical dissipation that depends on the discretisation length ξ and the numerical core thickness σ but at a larger length scale.

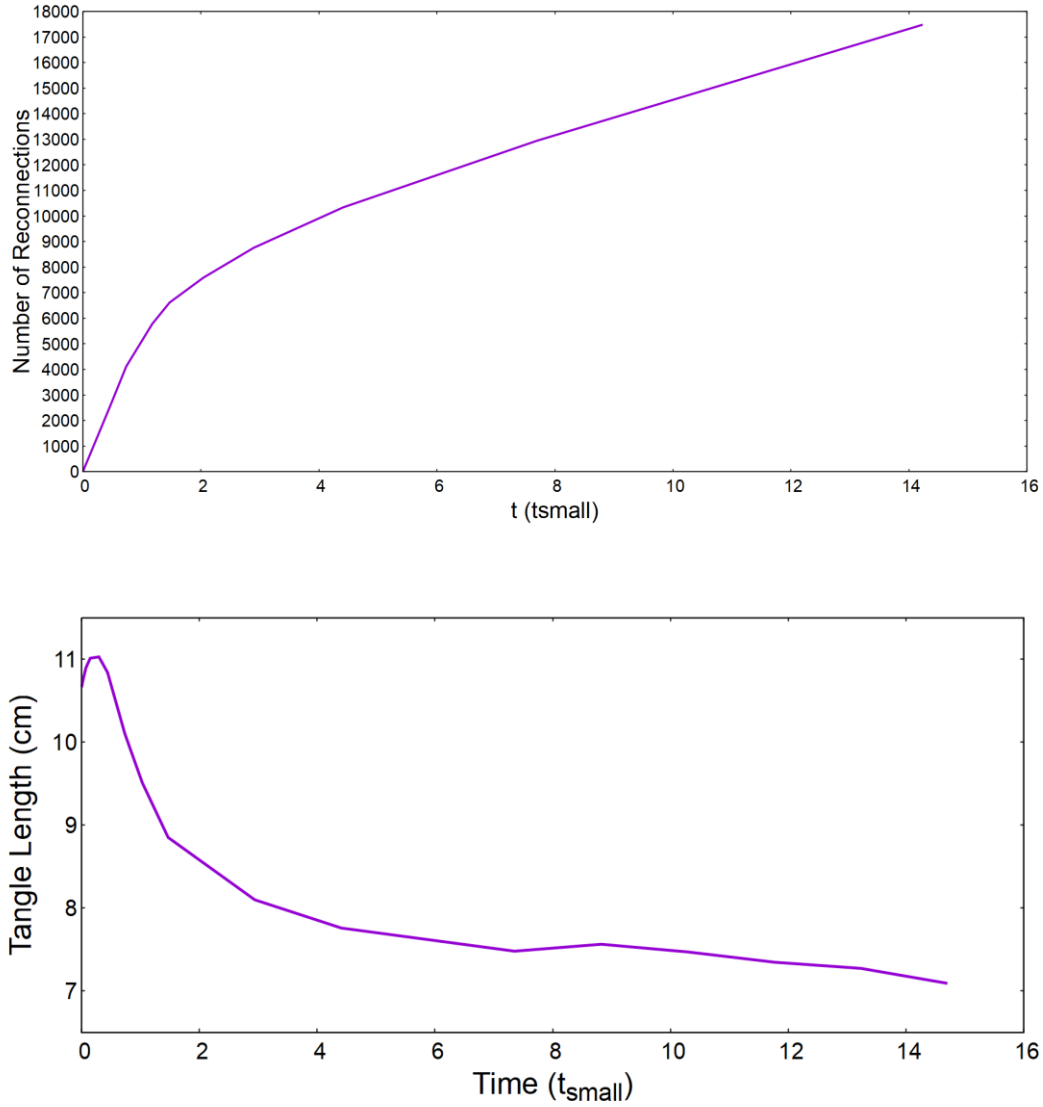

Fig. 37 - Plot showing the number of reconnections against time (top) and total tangle length against time (bottom). The total tangle length decreases as a proxy of the energy lost as sound waves when reconnections happen.

These reconnections remove the small scales from the tangle and expels them in the form of fast moving small rings; this is clear in Fig. 36, as time passes the system is populated more and more by small rings and if you look closely at the large structures (tangle), the tangles are very smooth and lack small scales unlike the tangles in Fig. 25.

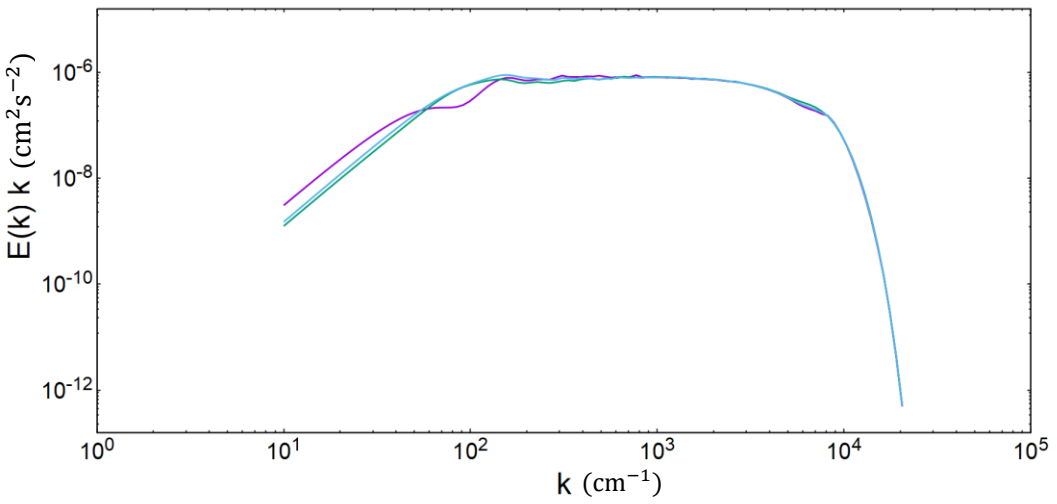

Fig. 38 - Energy spectra of the chaotic tangle configuration at t=0 (purple), t=0.0147 (blue) and t=0.0442 (green). This shows that spectral signature of the Kelvin wave cascade is k^{-1}.

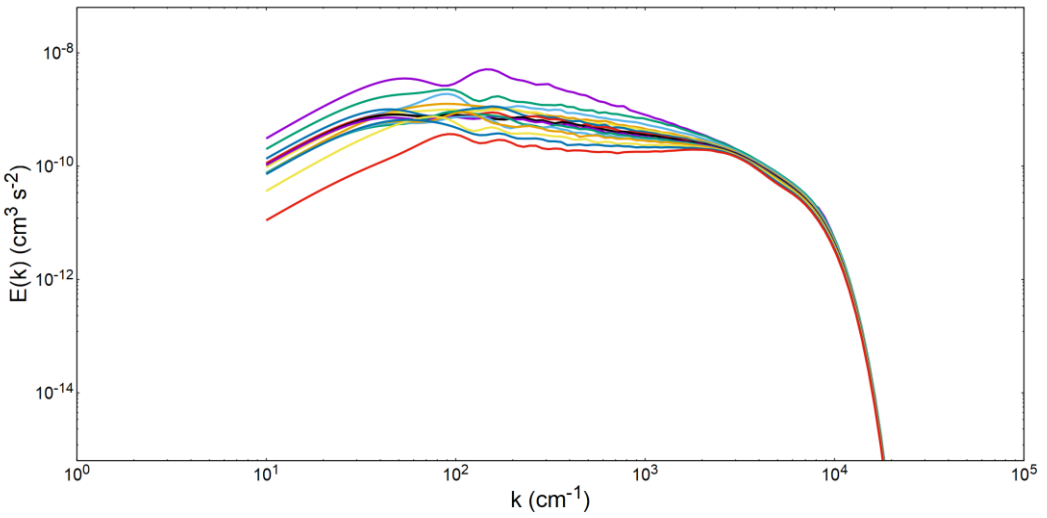

Fig. 39 - Energy spectra of the chaotic tangle configuration at t=0, t=0.4411, t=0.7351, t=1.1762, t=1.4703, t=2.0437, t=2.8964, t=4.4108, t=7.7042 and t=14.2321 (top to bottom).

The k^{-1} scaling at t=0 and at early times (prior to any interactions between Kelvin waves) shown in Fig. 38 is in agreement with the results from Baggaley in [82] regarding the randomly placed vortex rings, where also he finds a k^{-1} scaling in the spectra of the system. Fig. 39 shows the energy spectra at the times corresponding to the tangle configurations shown in Fig. 36. As time passes, and reconnections happen, the Kelvin waves transfer energy to small scales, but there is no further energy increase at small scales because there is no equilibration happening; this is due to the small rings separating from the large tangle and therefore not participating in the equilibration dynamics any longer. The expelling of small

rings after a vortex reconnection was also detected by Araki and Tsubota in [111]. Therefore, the small scales do not stay in the tangle, and once they escape, they can no longer interact with other Kelvin waves in the tangle resulting in no equilibration procedures happening. Furthermore, the way that the algorithm is set up, when small enough rings are generated (<=4 vortex points) they are removed from the system.

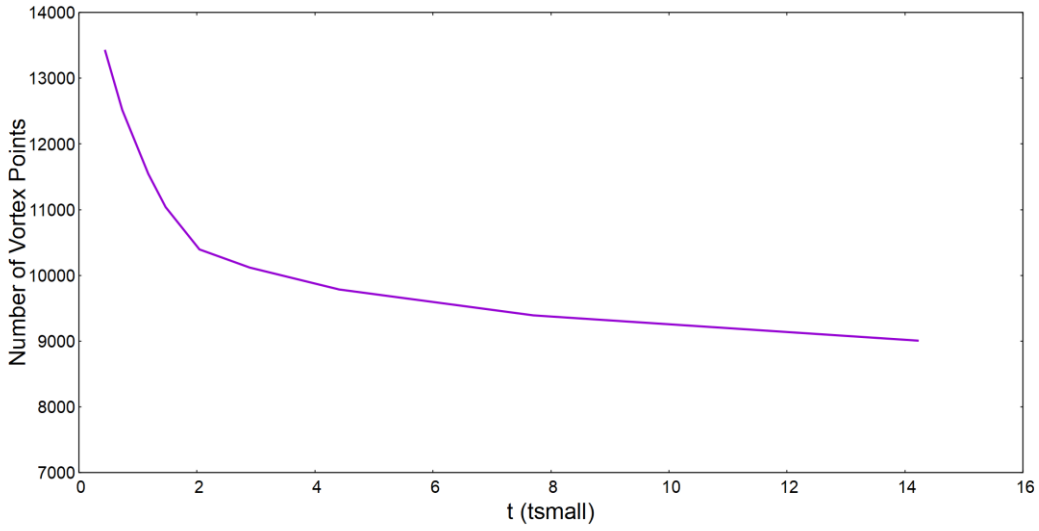

Fig. 40 - Plot showing the number of vortex points in the system against time.

The reconnections condition in this configuration did not allow any symptoms of energy equilibration to arise; the many small rings that are exiting the main vortex tangle take small-scale Kelvin waves away from it and separate them away from the collisional/superpositional interactions that happen within the tangle, therefore energy equilibration is impossible.

5.2.3. Full reconnections vs no reconnections.

In this section I do the same as with the cubic configuration: I set up two identical calculations, with the only difference being one allows all reconnections to happen and the other disallows reconnections after some have happened. This will help me understand the effects of reconnections on the spectra shape from this configuration. To do this I started a configuration identical to the one in **Section 5.2.2** and left it running until $t = 0.4411\ t_{small}$ ($t = 0.2772\ t_{large}$), this allowed the tangles to reconnect enough for sufficient Kelvin waves to be generated. After this time, I stopped the execution and ran two configurations in parallel restarting from the same time: one would allow reconnections, while the other had the reconnections disallowed. At $t = 2.0657\ t_{small}$ ($t = 1.2983\ t_{large}$), due to the disparity in reconnections, the tangles looked like the following:

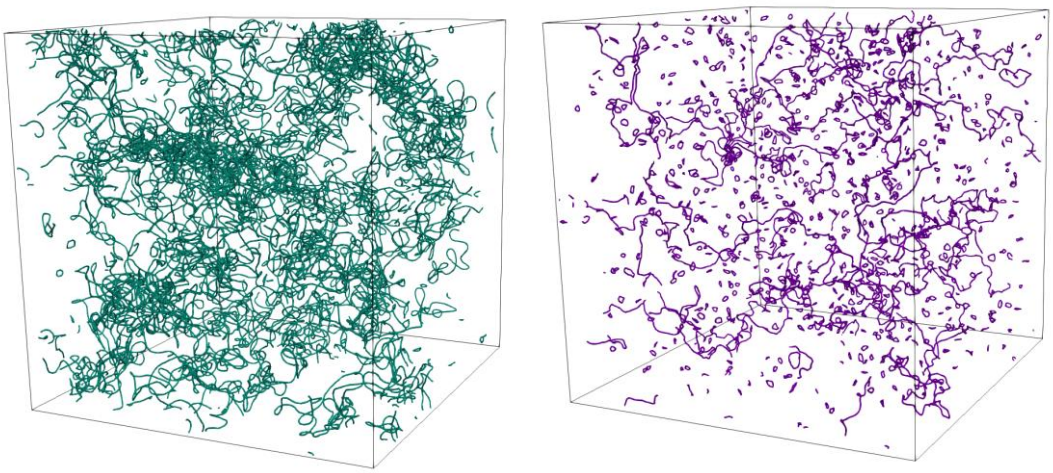

Fig. 41 - Chaotic tangle configuration at t=2.0657 with reconnections disallowed (left) and reconnections allowed (right).

Fig. 41 shows that the calculation with reconnections disallowed generated fewer small rings (the small vortex rings present are from the initial reconnections) than the calculation where the vortices were allowed to reconnect freely; it is also possible to see that there are smaller scales present on the large structures when reconnections were disallowed.

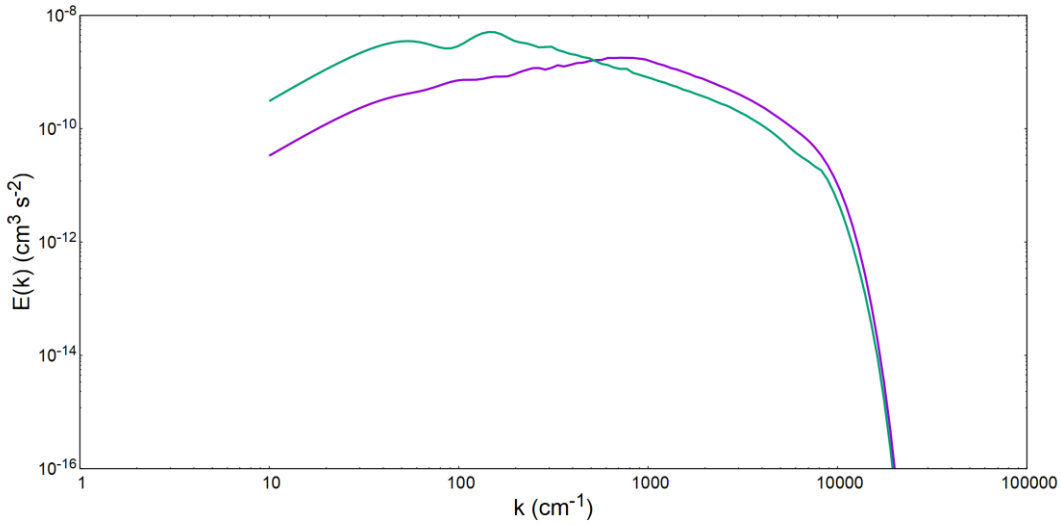

Fig. 42 - Energy spectra of the chaotic tangle configuration with reconnections disallowed at t=0 (green) and at t=2.0657 (purple), the purple line presents a $k^{0.7}$ regime at intermediate k values.

Fig. 42 shows that between $t = 0$ and $t = 2.0657\ t_{small}$ ($t = 1.2983\ t_{large}$) there has been a transfer of energy from large to small scales, this is seen as the energy at smaller k values decreased, while the energy at higher k values increased. In this case, where the reconnections have been disallowed ("turned off") to allow the Kelvin waves to interact without any resulting reconnections or self-reconnections, the energy spectra shows the

spectral signature of the interaction between different sized Kelvin waves as energy equilibration is taking place; at this point the energy spectra has a $k^{0.7}$ scaling at intermediate k values. Fig. 42 shows a clear transfer of energy from large scale to small scales that slowly happens over time; this energy transfer to smaller scales was also captured by Araki et al. in [98].

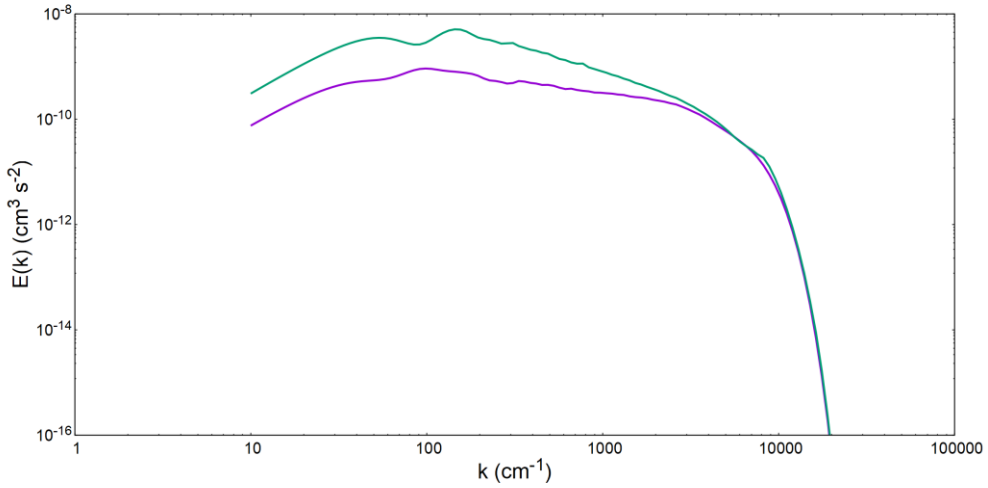

Fig. 43 - Energy spectra of the chaotic tangle configuration with reconnections allowed at t=0 (green) and at t=2.0657 (purple).

Doing the same comparison when reconnections were allowed shows a different change in energy. There is a decrease in energy at large scales but the energy at small scales has stayed the same, or even decreased at intermediate values of k. This is likely because, as smaller scales were generated from the superposition of Kelvin waves, small rings would be generated when these small scales reconnected, this would remove the small scale from the large tangle and even sometimes would disappear from the system if the small ring is small enough. This does not happen when the reconnections are disallowed because the small scales are retained in the tangle, as seen in Fig. 43.

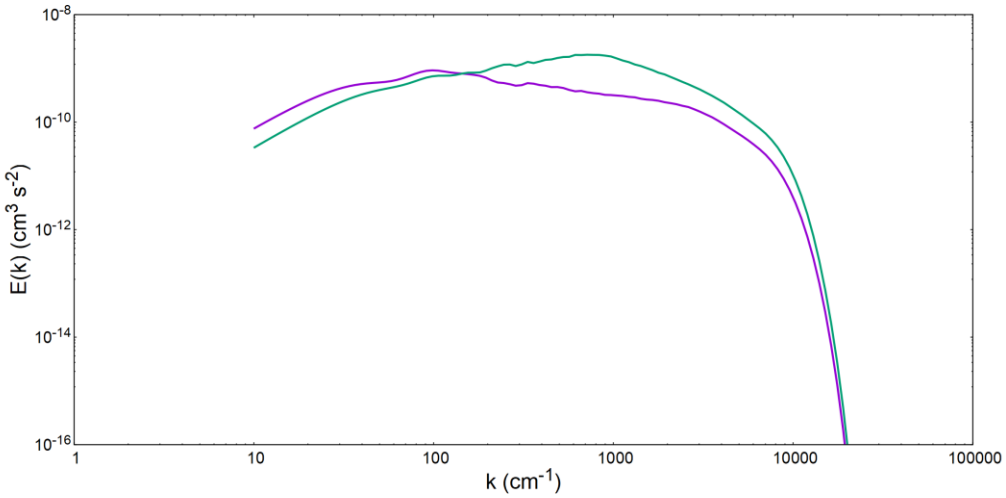

Fig. 44 - Energy spectra of the chaotic tangle configuration at t=2.0657 with reconnections disallowed (green) and reconnections allowed (purple).

When comparing the case where reconnections are disallowed against the case where they are allowed, the energy at large scales effectively stays the same, but when looking at small scales is where there is a noticeable difference. There is a higher energy at small scales when reconnections are not allowed than when they are; this is also the case in **Section 5.1.4** (but less noticeable). In the case where reconnections are disallowed, the different sized Kelvin waves are allowed to collide and superpose continuously, entering in an energy equilibration procedure that is not allowed to happen when reconnections are continuously happening.

5.3. Results for Vortex Collider Configuration

At this point I know from Navier-Stokes turbulence that there is a $k^{-5/3}$ law which people associate with vortex stretching. I want to inquire if this $k^{-5/3}$ law is true and can appear in quantized vortex dynamics. I don't expect it to be the case for isolated vortices because of their thin constant core does not allow for vortex stretching, so I will discretise a Navier-Stokes filament using quantized vortices. I can do this by placing many quantized vortices together in a polarised bundle and then investigate its energy dynamics; this is a way of connecting the two different disciplines (Navier-Stokes and quantized vortices).

5.3.1. Initial Conditions

For this vortex configuration, I set-up a calculation involving 6 bundles consisting of 49 quantized vortex rings each, with a total circulation of 0.048853 cm^2s^{-1}. The bundles are arranged in pairs with an offset in their centreline: this allows them to move towards each other without a head-on collision.

For the energy spectra computation, I gave the vortex filaments a finite core thickness for the purpose of stability in the energy spectra calculation. This had a value of $\sigma_{diag} = 1.1\xi$, where $\xi = 2.371 \times 10^{-3}$cm is the discretisation length along the vortex filaments; this would result in a vortex numerical core radius of 2.6081×10^{-3}cm. Using this value of discretisation length, results in each vortex bundle being discretised into 5363 vortex points, adding up to a total 32178 vortex points for all six vortex bundles. For the numerical stability of the evolution of the quantized vortices I use a parameter $\sigma = 1.1\xi$; in this case the same core thickness was used for both the diagnostic and numerical cores, but this is not always the case.

The characteristic time of the system is calculated using the diameter of the centreline vortex ring, and the circulation of one of the bundles. This results in a characteristic time $t_c = \frac{0.083^2}{49*9.97E-4} = 0.141s$; all times from this point onwards are in characteristic time, t_c, units. I have also calculated a large-scale characteristic time, defined as the time needed for one vortex bundle to travel from one side of the domain box to the opposite side. The domain box has a size $L = 0.1cm$ and the propagation velocity of the vortex bundle is approximately $V_{bundle} = 0.3221cm\ s^{-1}$. The large-scale characteristic time is therefore given as $t_{large} = 0.3105s$.

To generate the vortex bundles, I used the algorithm developed by Winckelmans and Leonard in [78], which discretises a vortex tube into several vortex filaments, creating a vortex bundle. It starts with a vortex filament running though the centreline of the vortex tube's body and then generates layers of vortex filaments that radiate outwards; the number of layers depends on how well the vortex tube is to be discretised, as show in Fig. 45 (left). The number of vortices per layer depends on the layer, following the relation: $N_v(n) = 8\,n$, where N_v is the number of vortices for a given layer, and n is the layer number (1, 2,3, …, n_c). The distance between the vortex rings layers and the central filament ring is calculated by: $r_c(n) = rl\frac{(1+12(n^2))}{6n}$, where rl is the radius of the area assigned to each vortex.

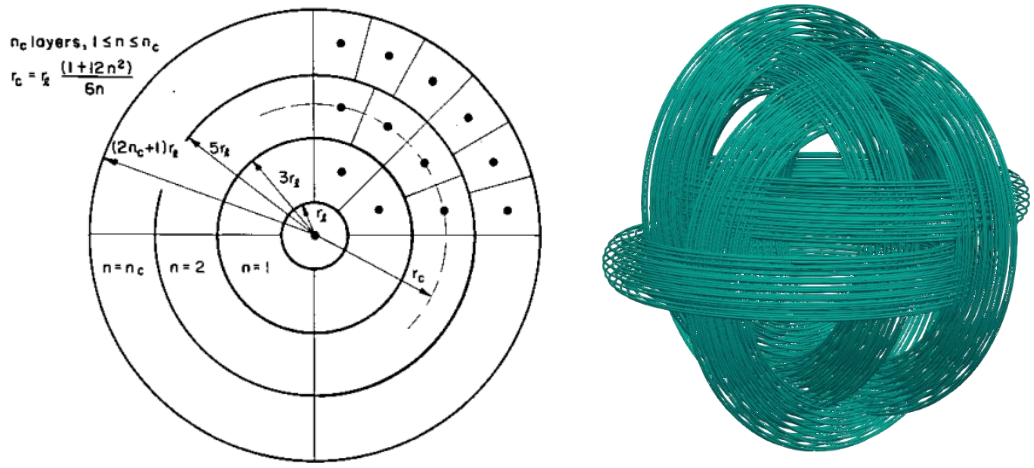

Fig. 45 - Method to discretise a vortex tube into vortex filaments [78] *(left) and the result of running said method to generate bundles of quantized vortex rings in a vortex collider configuration(right).*

In this case the bundle cores are resolved into 49 vortex rings (1+8+16+24), resulting in a bundle core thickness of 0.0166cm in diameter; the geometry resulting from this algorithm can be seen in Fig. 45 (right).

The bundles are arranged in parallel pairs, one pair is placed parallel to the X-Y plane and the other two pairs are parallel to the X-Z plane and Y-Z plane respectively. The bundle pair placed in the X-Y plane are displaced in the +Z and -Z direction to create a gap between them so they can evolve dynamically prior to colliding with each other. They are then offset in the +Y and -Y direction to make the bundles not collide head on with each other and allow for more vortex stretching to happen. For this bundle pair, their centreline has not been offset from the X-axis, only from the Y and Z-axis. This bundle pair move in the +Z and -Z direction, towards each other.

For the bundles parallel to the X-Z plane, they are displaced in the +Y and -Y direction by an amount set in the input file. Then, to avoid a head-on collision these bundles were offset in the +X and -X direction and move towards each other, +Y and -Y direction.

The last pair of bundles are parallel to the Y-Z plane and have been displaced to have a distance between them in the +X and -X direction. They have also been offset in the +Z and -Z direction to allow for an offset collision and they move towards each other, in the +X and -X direction.

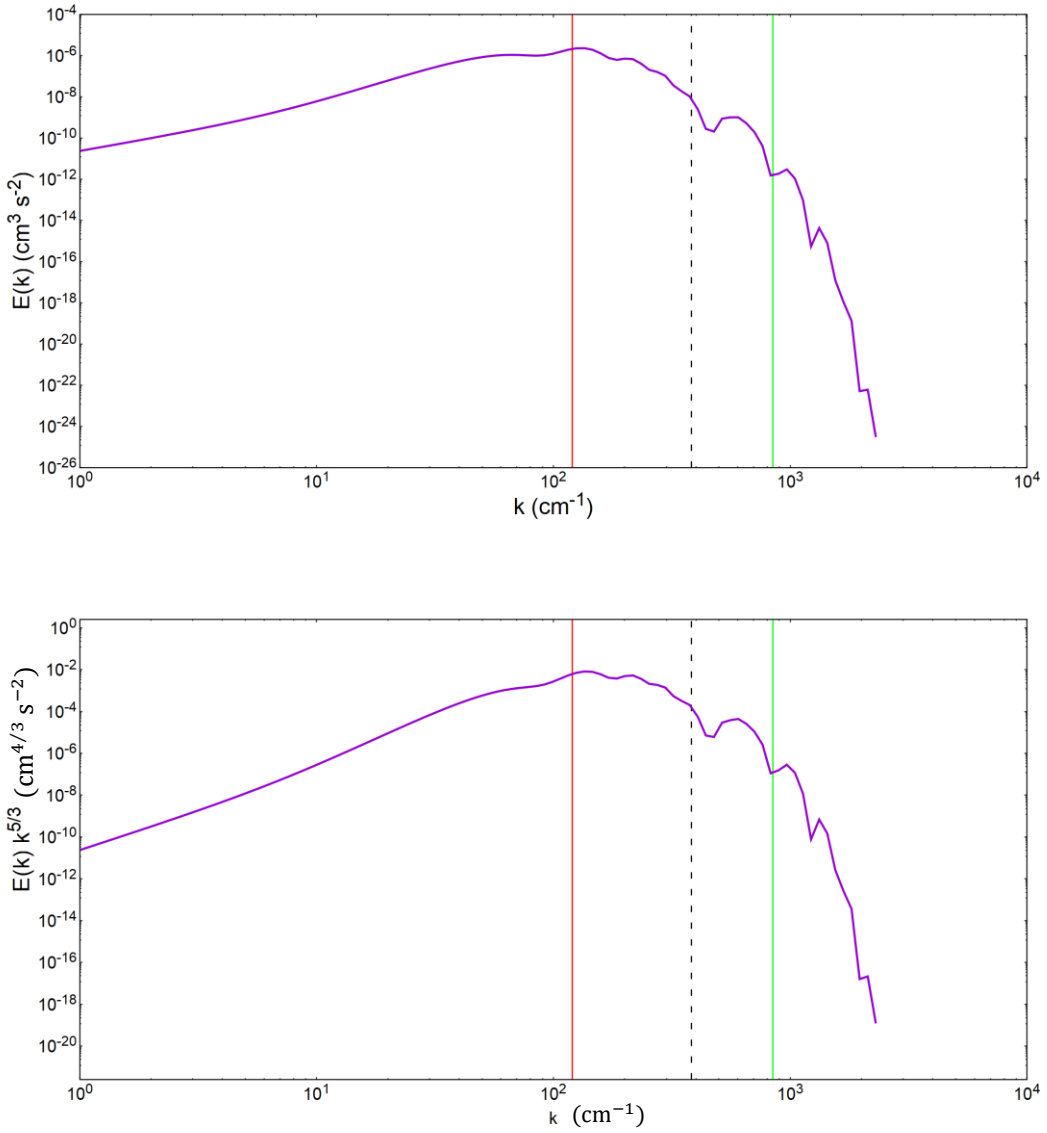

Fig. 46 - Energy spectra graph (top) and multiplied by $k^{5/3}$ (bottom) showing no sign of a k-5/3 regime at t=0.

Fig. 46 shows the energy spectra plot for t=0 of the vortex configuration shown in Fig. 45 (right); note that there is no $k^{-5/3}$ at any range of wavenumber k, as seen in Fig. 46 (bottom). In these plots I have represented different length scales as wavenumbers. The red line marks the peak energy of the plot, and it corresponds to the quantized vortex bundle core radius. The green line represents the intervortex distance and the dashed black line represents the diagnostic core radius.

5.3.2. Energy cascade with no $k^{-5/3}$ regime.

As time passes, the line vortices within the bundles interact with each other, deform and experience core torsion. This is accompanied by an energy cascade from large scales to small scales, which can be seen in Fig. 47.

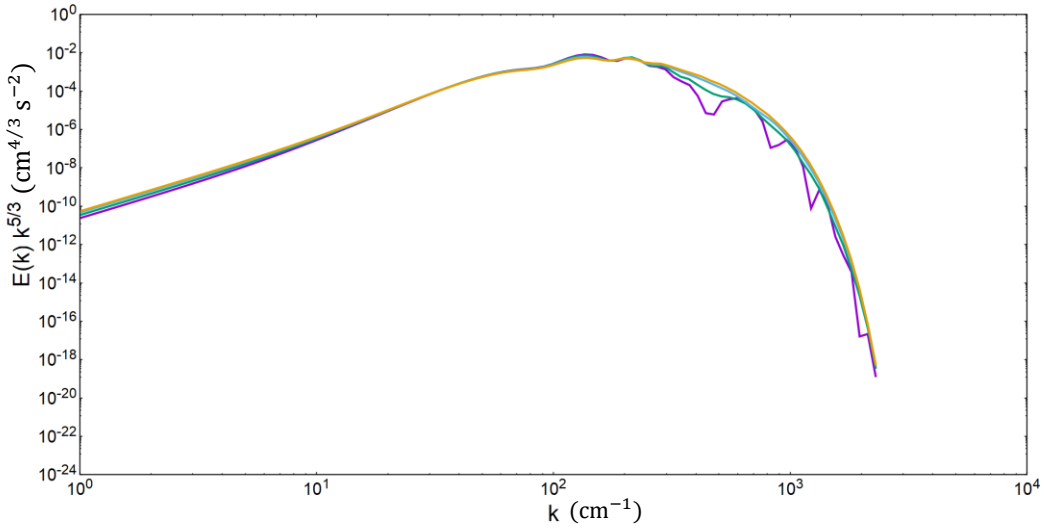

Fig. 47 - Energy spectra of the quantized vortex tangle at t=0 (purple), t=0.0466 (green), t=0.0891 (blue) and t=0.1188 (yellow) with no $k^{-5/3}$ regime.

In Fig. 47 you can see that an energy transfer from large scales to small scales has happened at t=0.0446, this energy transfer becomes greater and more obvious when looking at the energy spectra at t=0.0891. The energy at smaller scales has increased and the energy at the highest energy point has decreased (a small change in large scales brings a larger change at smaller scales). This continues happening through to t=0.1188. It is important that this continuous transfer of energy from large scales to small scales shows a clear energy cascade and is not associated with a discernible $k^{-5/3}$ regime.

5.3.3. Formation of a Kolmogorov Spectrum by Vortex Stretching.

As time passes, the vortex rings stretch because the rings were configured to form a series of bundles; as the length of the vortex rings increases, the bundle core thickness decreases in size, just like it happens with Navier-Stokes filaments. For this to happen with quantized vortices they need to be set-up in a bundle configuration like in Fig. 45 (right), because if we consider a quantized vortex as an example of a vortex line, the quantized vortex bundles can be thought of as a discrete version of a Navier-Stokes filament. When the vortices in the bundle stretch, the bundle core thickness is reduced, mimicking the core dynamics of classical

vortices. As isolated quantized vortices are topological defects, when they stretch they simply increase their length, but as their core is quasi-infinitely thin, there are no core dynamics in contrast with Navier-Stokes vortices. Moreover, there is no vorticity distribution in the core, so there can be no enstrophy amplification either.

Fig. 48 – Quantized vortex tangle at t=0.1486 (top) and zoomed in section of a bundle front view (left) and side view (right).

At t=0.1486 the bundles have deformed while still retaining their bundle structure, as seen in Fig. 48 (top). As seen in Fig. 48 (left), the bundle appears to have stretched considerably lengthwise while the core shrunk in the radial direction, agreeing with Chorin in [4], pulling the quantized vortices closer together. Fig. 48 (right) shows a side view of the stretched bundle core, and it reveals that the bundle has experienced sheetification, with the vortices

being flattened together; this makes the bundle lose its cylindrical geometry. This flattening behaviour was also detected by Kerr in [114] and Melander and Hussain in [14], where colliding vortices deform and collapse into vortex sheets; the collapsing of vortices in Kerr's work is associated with vortex reconnections, while my bundle sheetification is due to pure vortex stretching (i.e. without the presence of reconnections). Furthermore, McKeown et al. in [115] detect vortex flattening experimentally, with a consequent vortex sheet forming during the collision between 2 vortex rings.

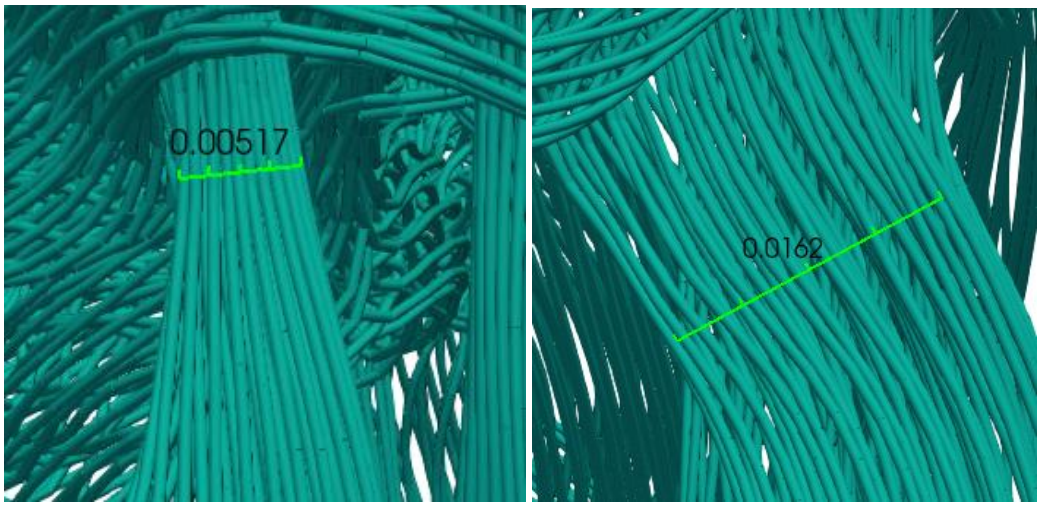

Fig. 49 - Front (left) and side view (right) sizes of a bundle of quantized vortices at t=0.1486.

The bundle core was measured in two perpendicular directions, these sizes were approximated to be 0.00517cm and 0.0162cm as shown in Fig. 49.

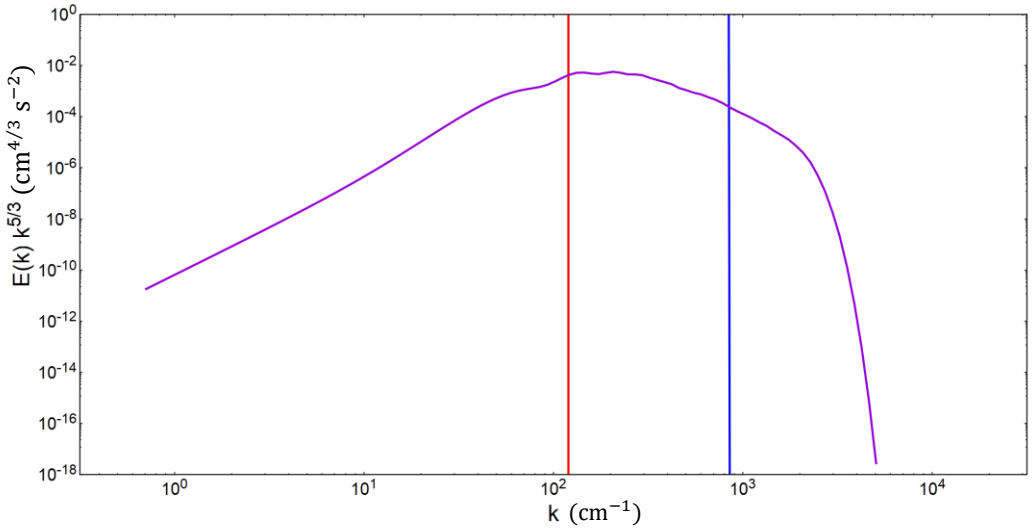

Fig. 50 - Energy spectra at t=0.1486 showing a $k^{-5/3}$ regime first appearing. Half-distance between bundle core's centrelines (red) and diagnostic core radius (blue).

The energy spectra for t=0.1486 shows a $k^{-5/3}$ regime first appearing, with a short span of approximately 200 wavenumbers; however, this $k^{-5/3}$ is insufficient to draw conclusions.

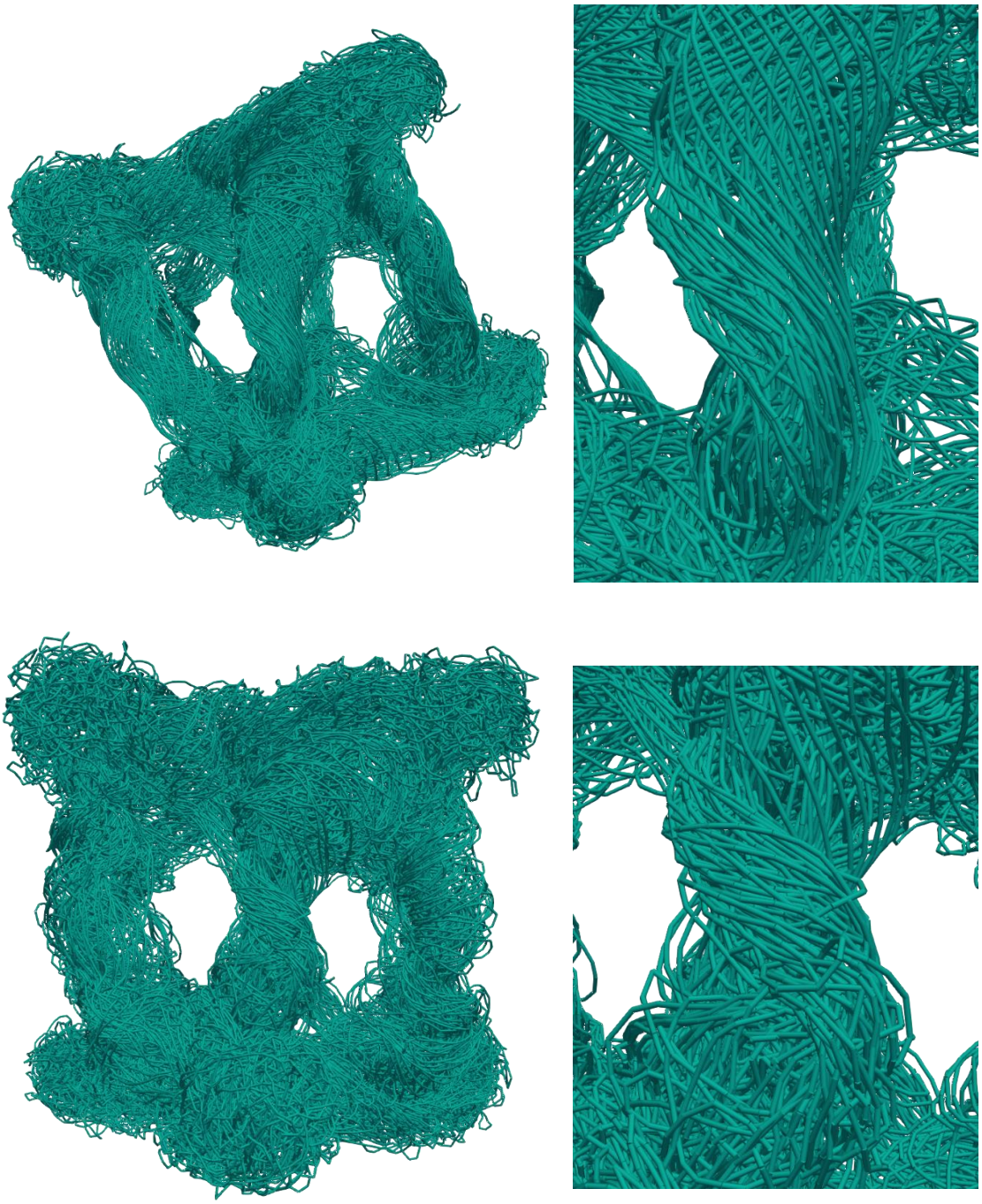

Fig. 51 - Quantized vortex tangle at t=0.4457 (top left), zoomed in to centre bundle (top right), quantized vortex tangle at t=0.5942 (bottom left) and zoomed in to centre bundle (bottom right).

At t=0.4457 the bundles have stretched lengthwise, and their cores have decreased in diameter, they also have undergone core torsion to some extent while still retaining their

bundle structure: this can be seen in Fig. 51 (top left). The zoomed in section in Fig. 51 (top right) shows how the individual quantized vortex rings that make up the bundle cores have become helical due to core torsion and have moved closer together concentrating their vorticity at a smaller scale.

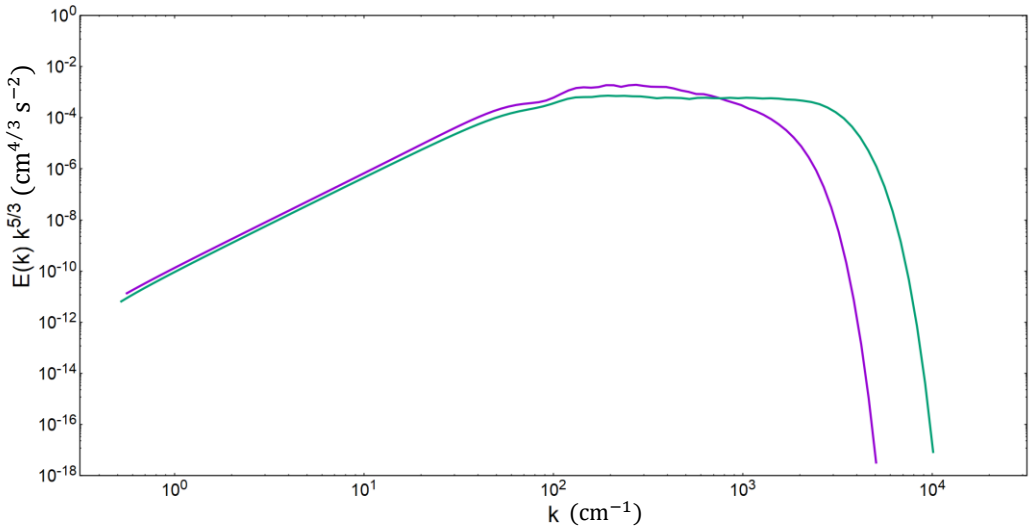

Fig. 52 - Energy spectra graph showing $k^{-5/3}$ regimes at t=0.4457 (purple) and t=0.5942 (green). A smaller diagnostic core was used for t=0.5942 to ensure the $k^{-5/3}$ regime is captured.

Fig. 52 (purple) shows a $k^{-5/3}$ regime approximately in the wavenumber range 120 – 500 and a subsequent cut-off due to the smoothing vortex core thickness applied. The extension of the $k^{-5/3}$ regime in the purple plot in Fig. 52 (purple) is insufficient to prove the arising of a $k^{-5/3}$ scaling from a system where this regime was non-existent at the initial conditions; therefore, I continued calculating the dynamics of this quantized vortex bundles configuration until the extension of the $k^{-5/3}$ regime was sufficient to prove its existence.

Fig. 51 (bottom left) shows the quantized vortex bundle geometry at t=0.5942, and it is clear from it that even though the chaos in the system has increased, the structure of the bundles is still being preserved. Fig. 51 (bottom right) shows that the individual vortex lines have moved even closer together from Fig. 51 (top right) concentrating the vorticity at even smaller scales; the torsion experienced by the bundle core shown in Fig. 51 (bottom right) has increased from Fig. 51 (top right). This continued stretching and torsion of the bundle core is accompanied by an extension of the $k^{-5/3}$ regime for approximately wavenumber range 120 – 1700 as seen in Fig. 52 (green).

For t=0.5942 I experimented by reducing the diagnostic core to $\sigma_{diag} = 0.25\xi$ to ensure I can capture the extension of the $k^{-5/3}$ regime while still preserving the stability of the energy spectra calculation. I calculated the diagnostic core to have a wavenumber $k = 1686\, cm^{-1}$, represented by a vertical blue line in Fig. 53, which aligns with the end of the $k^{-5/3}$ regime.

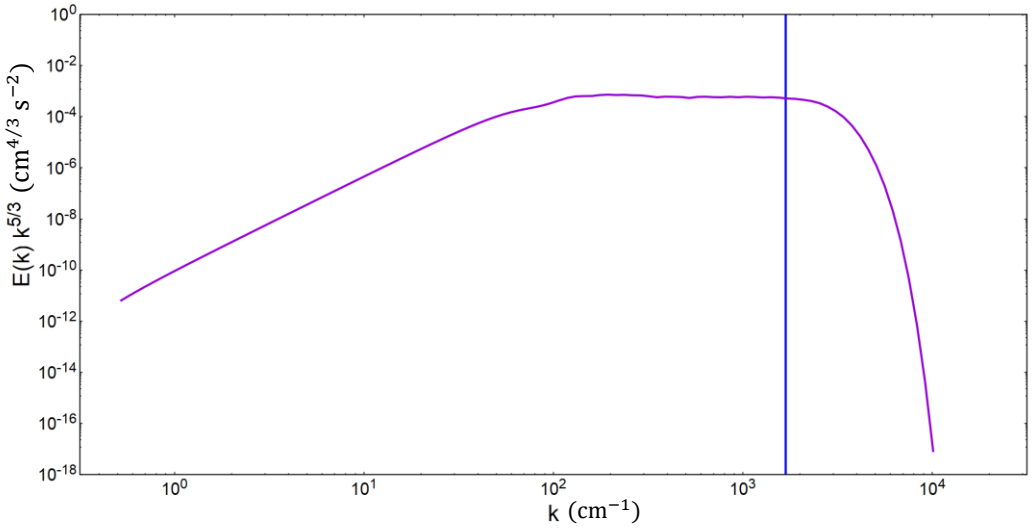

Fig. 53 - Energy spectra at t=0.5942 showing a $k^{-5/3}$ regime ending approximately at the scale of the diagnostic core radius (blue line).

Fig. 53 show a clear and extensive $k^{-5/3}$ regime that appears due to the combination of vortex stretching and core torsion in bundles of polarised quantized vortices; this now poses the question as to whether core torsion is necessary for the appearance of a $k^{-5/3}$ regime.

5.3.4. Kinematic vortex stretching.

Now I want to see the effect of concentrating vorticity in smaller scales without the effect of core torsion and see if this results in a $k^{-5/3}$ spectrum. This was done by kinematically stretching the initial quantized vortex bundles from the previously described configuration. I stretched the vortex bundles by reducing the bundle core thickness and increasing the bundle radius accordingly, to maintain the bundle volume constant. Doing this would result in the quantized vortices being closer together, with the absence of physical instabilities and vortex bundle torsion.

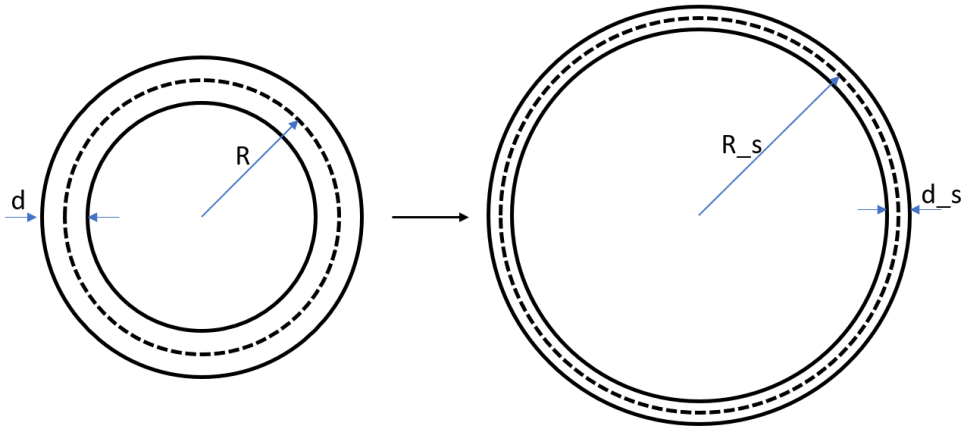

Fig. 54 - Kinematic vortex stretching diagram. R and d are the bundle radius and the core diameter respectively. "_s" corresponds to the same sizes when the bundle was kinematically stretched.

Fig. 54 shows how the bundles were kinematically stretched, decreasing the bundle thickness but increasing the bundle radius; this conserved the bundle volume after the stretching. I stretched the bundles from the original configuration enough to have 0.85, 0.75 and 0.5 of the original bundle thickness, with their respective increase in the bundle radius to keep their volume constant. For each of these three configurations, the energy spectra was calculated to see the effect of the concentration of vorticity to smaller scales on the shape of the energy spectra of the system. For the sake quantification, I define a ratio of the diameter of the bundle core to the diameter of the bundle as $r_D = D_C/D_B$.

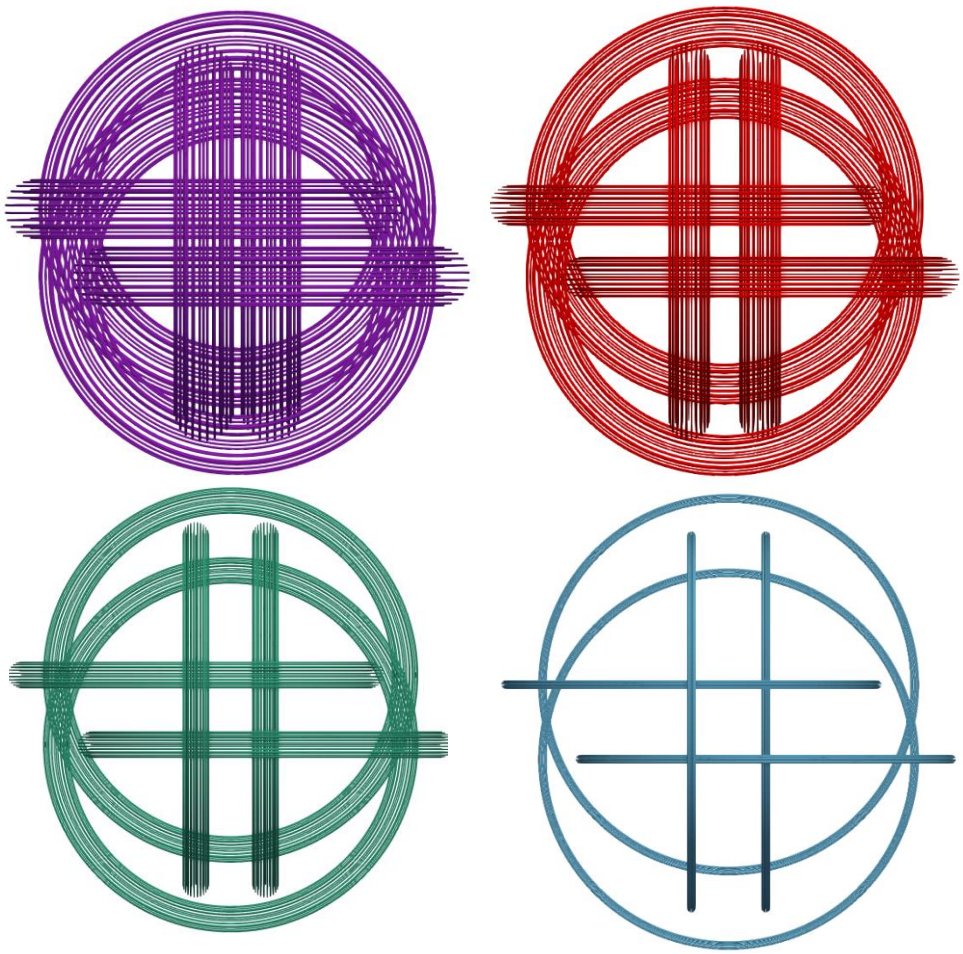

Fig. 55 - Bundle configuration with their original size (top left [purple]), 15% core reduction (top right [red]),25% core reduction (bottom left [green]) and 50% core reduction (bottom right [blue]).

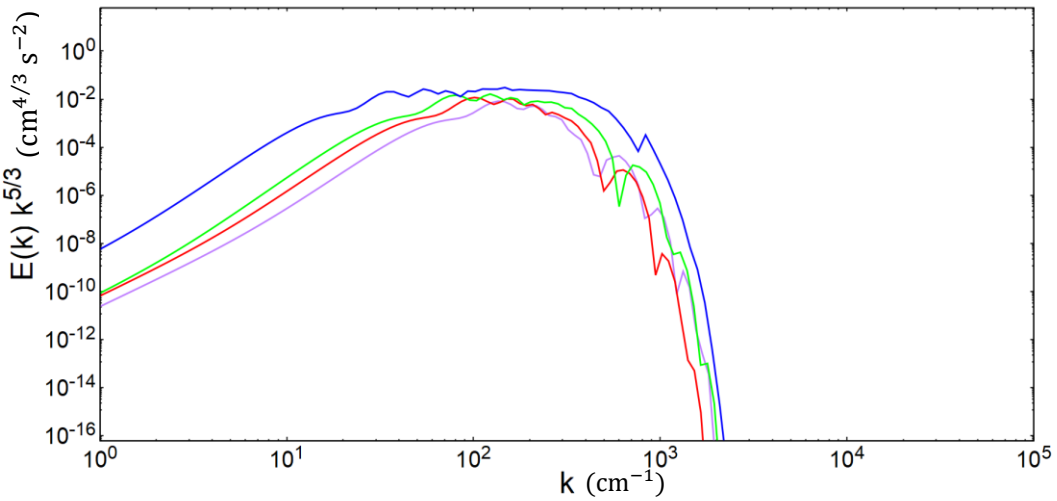

Fig. 56 - Energy spectra for original core size (purple), 15% core reduction (red), 25% core reduction (green) and 50% core reduction (blue) showing a growing $k^{-5/3}$ regime. The $k^{-5/3}$ regime first appears when the core has been reduced by 15%, and as the core is continuously reduced, the range of the $k^{-5/3}$ regime grows.

Fig. 56 shows that the original sized bundles with a radius of 0.0415cm and a bundle core diameter equal to 0. 0166cm (purple plot) have no $k^{-5/3}$ scaling; here $r_D = 0.2$. Firstly, I kinematically stretched the bundles to have a core diameter of 0.01411cm (0.85 of the original core size), this made the bundles increase to a bundle radius equal to 0.05744cm. At this stretching amount, the ratio $r_D = 0.1228$. Approximately at this diameter ratio is when I first detect a $k^{-5/3}$ regime, although this regime approximately spans only 100 wavenumbers, as shown in the red plot in Fig. 56.

When the bundles are stretched to have a bundle core diameter of 0.0125cm (0.75 of the original core size), their radius increase to 0.0738cm and the ratio $r_D = 0.0844$; this results in an energy spectra with a $k^{-5/3}$ regime that spans approximately from $k = 68cm^{-1}$ to $k = 383cm^{-1}$ (315 wavenumbers). The expansion of the $k^{-5/3}$ regime without any dynamic transfer of energy shows that it is possible that it can be attributed to the concentration of vorticity at smaller scales. This $k^{-5/3}$ scaling was also found by Kivotides and Leonard in [90], where they work with Navier-Stokes vortices with dynamic cores and quantized circulation but without any vortex core torsion; here the $k^{-5/3}$ appeared as a result of the exclusively filamentary vorticity in the system.

To further prove this, I stretched the bundles even further to have a bundle core diameter of 0.0083cm and a bundle radius of 0.166cm; this would be a bundle core thickness of 50% of the original size and a ratio $r_D = 0.025$. This bundle configuration can be seen in Fig. 55 (bottom right) and its corresponding energy spectrum is shown in the blue plot in Fig. 56. It is important to note that the peaks and dips that appear in the spectra on the other "less-stretched" configurations are not present in this plot, this is because as the quantized vortices are pulled closer together due to the stretching, the discretisation becomes finer. Again, following my argument that the $k^{-5/3}$ regime is related to the focusing of vorticity at smaller scales, the $k^{-5/3}$ regime in the spectra has increased in range and now spans for 353 wavenumbers, approximately from $k = 30cm^{-1}$ to $k = 383cm^{-1}$. This result suggests that the $k^{-5/3}$ regime is related to the focusing of vorticity at smaller scales, and that the flattening of the bundles and core torsion are not needed for such spectrum to appear. The reason that the energy from one configuration to another is not conserved and increases is that I force the configuration to maintain a constant geometry while being stretched, not allowing for any vortex folding; this means that there is no reason for the energy to be conserved. Therefore,

this is just a special arrangement whose purpose is to look at spectra scaling, not to conserve energy.

5.3.5. $k^{-5/3}$ regime at initial conditions.

There are several elements present when talking about bundles of quantized vortices: these include vortex stretching, energy transfer, vortex torsion, instabilities, vorticity concentration and $k^{-5/3}$ law. My argument is that the appearance of a $k^{-5/3}$ law is related to the concentration of vorticity at small scales; to further prove this argument I present results of a $k^{-5/3}$ regime at the initial timestep of the previously described configuration. I present different versions of the same configuration with varying bundle core thicknesses and constant number of quantized vortices per bundle, and their respective energy spectra; these include bundle core diameters equal to 0.0166cm, 0.0125cm and 0.00623cm. In this case, the vortex radii were kept constant, unlike in **Section 5.3.4**.

The three different bundle configurations used can be seen in Fig. 57, showing how the quantized vortices were configured to have different concentrations of vorticity. The energy spectra calculations done for these three configurations correspond to the initial condition only, and therefore exclude any energy transfers from large to small scales.

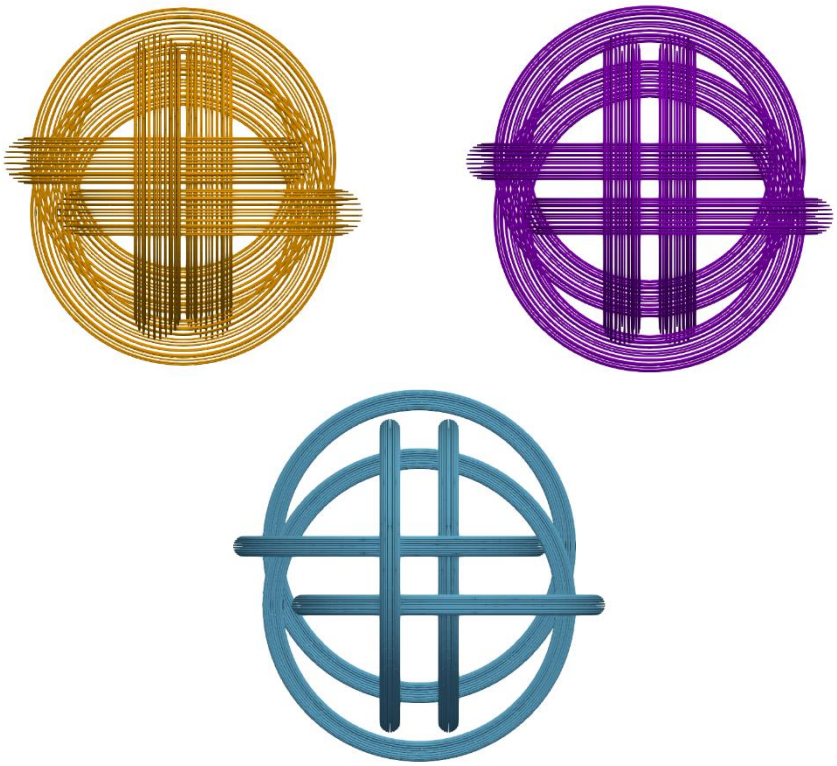

Fig. 57 - Bundle configuration with their original size (top left), 25% original core reduction (top right) and 62.5% original core reduction (bottom).

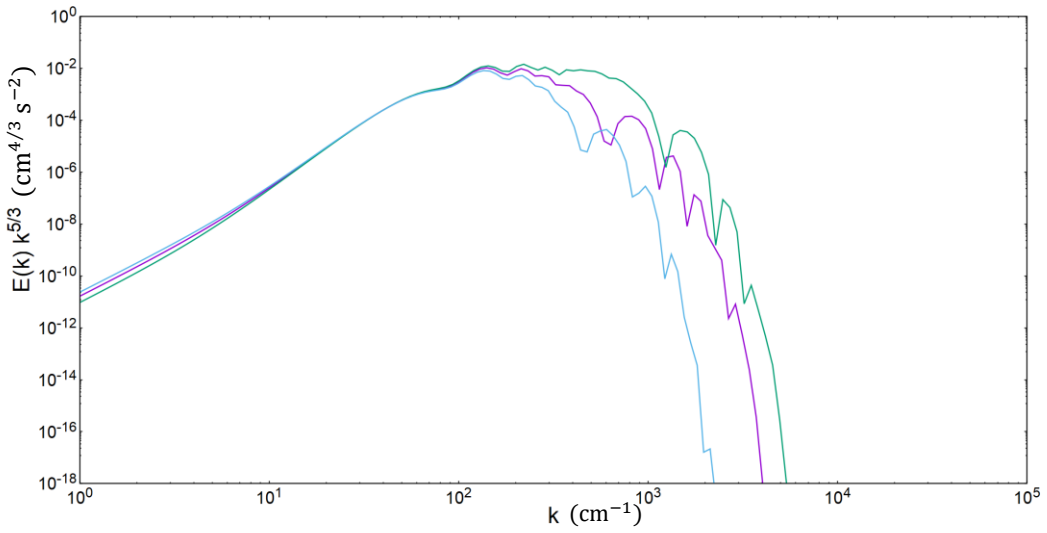

Fig. 58 - Energy spectra for original core size (left), 25% core reduction (middle) and 62.5% core reduction (right) showing a growing $k^{-5/3}$ regime.

Fig. 58 shows the energy spectra for each of the four configurations shown in Fig. 57. The orange bundle corresponds to the original configuration where the bundle core thickness is 0.0166cm in diameter. In this plot you can see that there is no $k^{-5/3}$ regime present as the separation between individual quantized vortices is too large (blue plot in Fig. 58). In this case, the ratio of the core diameter to the bundle diameter is given as $r_D = 0.2$.

For the next bundle configuration, I reduced the bundle core size by 25% to have a value of 0.0125cm. This corresponds to the purple bundle configuration in Fig. 57 and its corresponding energy spectra is seen in Fig. 58 as a purple plot. The purple plot in Fig. 58 shows a very small $k^{-5/3}$ regime has developed at intermediate wavenumbers, this is the first time that the $k^{-5/3}$ regime appears and it does at a core diameter to bundle diameter ratio $r_D = 0.1506$.

I reduced the bundle core thickness once more by 62.5% from the original bundle configuration to 0.00623cm; this corresponds to the blue bundle configuration in Fig. 57 (bottom) and the green energy spectra plot in Fig. 58 (right) . This reduction in bundle core thickness results in a decrease in the core diameter to bundle diameter ratio $r_D = 0.0751$ and an expansion of the $k^{-5/3}$ regime: now it spans for approximately 780 wavenumbers, approximately from $k = 120cm^{-1}$ to $k = 900cm^{-1}$. As the energy spectra calculated for these bundle configurations were only the initial conditions, the effect of elements like energy transfer, vortex torsion or physical instabilities were removed from the problem. Therefore,

the $k^{-5/3}$ regime that appears in these calculations is only attributed to the concentration of vorticity that happens when arranging the quantized vortices close to each other. A possible interpretation of this is that the $k^{-5/3}$ law is a result from the vorticity concentration that comes from vortex stretching, rather than energy transfer and that the $k^{-5/3}$ regime first appears and expands as the ratio between the core diameter and the bundle diameter r_D decreases.

5.4. Results for Hopf Link Configuration

In this chapter I want to prove that a $k^{-5/3}$ regime in the energy spectra of a quantized vortex bundle configuration is related to the concentration of vorticity that arises from vortex stretching, using a different vortex configuration. This was shown in the previous chapter, but I will confirm my findings with the new configuration discussed in this chapter, Hopf Link. I will also discuss the effects of secondary instabilities appearing in the vortex tangle and will compare the results to those found for the vortex collider configuration. The advantage of this method is that because there is no viscosity, the results are indicative of high Reynolds number phenomena; with this method not only can I study vortex stretching involving quantized vortices, but also study physics that original Navier-Stokes solvers cannot.

I set-up a calculation involving 2 bundles, 0.0415cm radius, defined by 49 quantized vortices each, with a total circulation of 0.048853 $cm^2 s^{-1}$. Just like in the previous chapter, for the energy spectra calculation I gave the vortex filaments a thickness value, $\sigma_{diag} = 1.1\xi$, where $\xi = 2.37143 \times 10^{-3} cm$ is the discretisation length along the vortex filaments.

The characteristic time of the system is calculated using the diameter of the centreline vortex ring and the circulation of one of the bundles. Therefore, the characteristic time $t_c = \frac{0.083^2}{49*9.97E-4} = 0.141s$; all times mentioned in this chapter are in characteristic time, t_c, units. I have also calculated a large-scale characteristic time defined as the time needed for one vortex bundle to travel from one side of the domain box to the opposite side. The domain box has a size $L = 0.1cm$ and the propagation velocity of the vortex bundle is approximately $V_{bundle} = 0.3221cm\, s^{-1}$. The large-scale characteristic time is therefore given as $t_{large} = 0.3105s$.

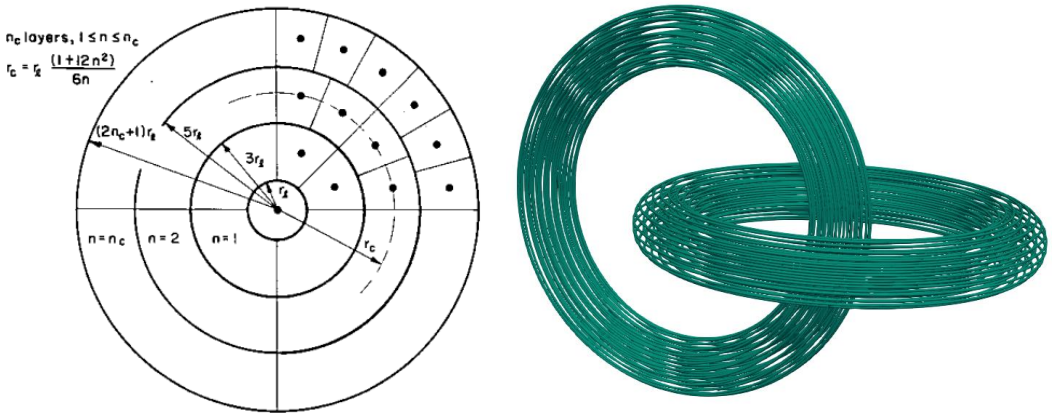

Fig. 59 - Method to discretise a vortex tube into vortex filaments [31] (left) and the result of running said method to generate bundles of quantized vortex rings in a Hopf-Link configuration (right).

To generate the vortex bundles, I used the same algorithm explained in the vortex collider configuration chapter, but this time I used different input parameters to generate only two vortex bundles with 49 quantized vortices each. For this configuration, the bundle was divided into 3 different layers: these layers contained 8, 16 and 24 filaments in radial order plus the filament running through the middle of the bundle core, making the bundle core have a diameter of 0.0166cm.

The first of the quantized vortex bundles is placed parallel to the XY-plane and is displaced in the +X direction only; the other bundle was rotated 90° around the X-axis and displaced in the -X direction so its centreline crossed the centre of the other bundle, making a Hopf-Link. The geometry resulting from the algorithm is shown in Fig. 59. The bundle parallel to the XY-plane moves in the -Z direction and the bundle parallel to the XZ-plane moves in the +Y direction.

5.4.1. Vortex stretching in Hopf-Link.

I let the vortices evolve with their induced velocities, bending and stretching as the vorticity field mandates. The bundles start twisting towards each other and start creating a “bridge” with two antiparallel bundle portions, this is seen in Fig. 60 (left). In Fig. 60 (right) this bridge is formed but still there are no physical instabilities on the bridge.

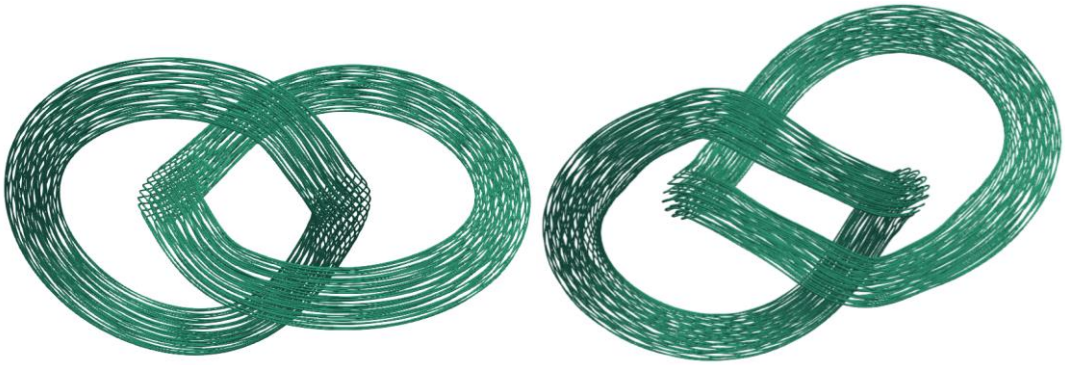

Fig. 60 – Quantized vortex bundles in a Hopf-link configuration at t=0.4454 (left) and t=0.7426 (right) showing the generation of a bridge of anti-parallel vortex bundle portions. This bridge does not present any evidence of physical instabilities having appeared.

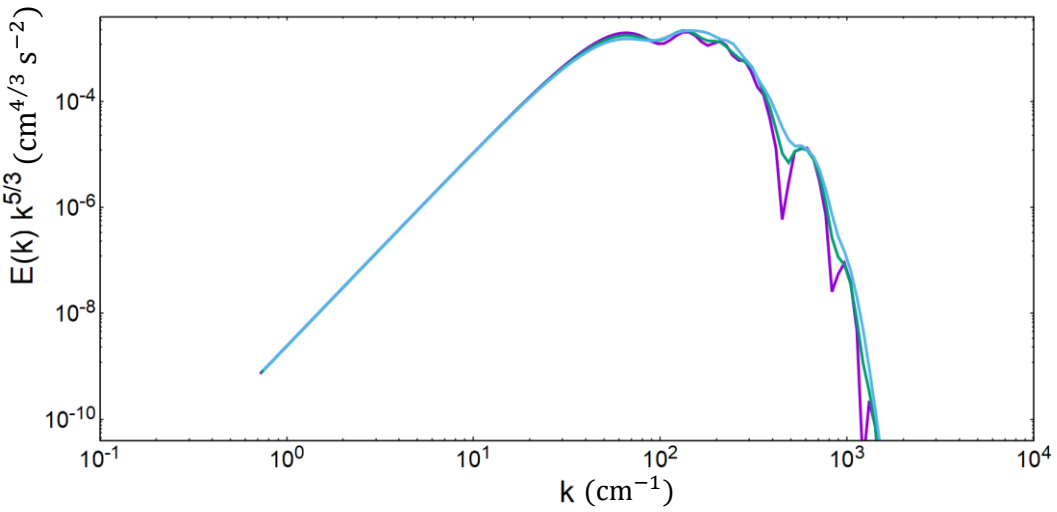

Fig. 61 - Energy spectra multiplied by $k^{5/3}$ of the Hopf-link configuration forming a bridge at times t=0 (purple), t=0.4454 (green) and t=0.7426 (blue). The plot shows no discernible $k^{-5/3}$ scaling, only a small transfer of energy from large to small scales.

Fig. 61 shows the energy spectra plots at $t = 0$ (purple), $t = 0.4454$ (green), $t = 0.7426$ (blue) where there is no appreciable $k^{-5/3}$ regime; this could be because the bundle cores have not been stretched much. Therefore, the small deformation that has happened turning portions of the bundles towards each other has transferred a small amount of energy towards smaller wavenumbers, as can be seen when comparing the purple and blue plot in Fig. 61. There is a clear progressive energy transfer from large to small scale, but the energy spectra shows that the generation of the bridge does not have a clear spectral signature.

Fig. 62 - Quantized vortex bundles in a Hopf link configuration at t=1.0397 (left) and t=1.1879 (right) showing the appearance and grown of a sinusoidal instability on the bridge.

At t=1.0397 the straight "bridge" starts to develop some secondary instabilities in the form of waves. In Fig. 62 (right), the secondary instabilities have grown enough to the point that the waves have joined into one and nearly wrap around the combined vortex bundle.

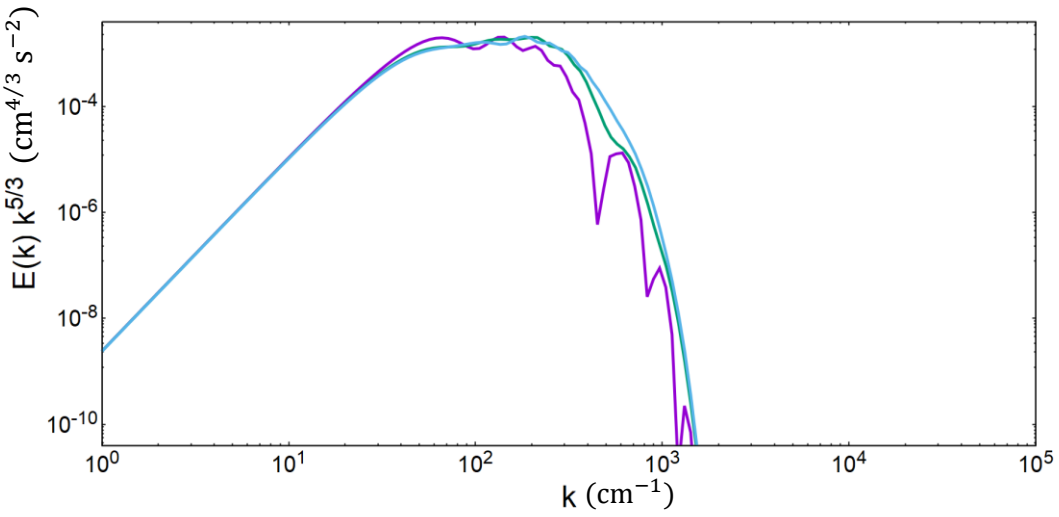

Fig. 63 – Energy spectra multiplied by $k^{5/3}$ of the Hopf-link configuration experiencing sinusoidal instability generation at t=1.0397 (green) and the growth of said generation at t=1.1879 (blue); for reference t=0 is plot in purple.

Fig. 63 shows an energy transfer from large to small scales, but the energy spectra shows that the appearance of the secondary instabilities does not have a clear spectral signature. The instabilities are not very pronounced in Fig. 62 (right) probably because the strength of the bundles (directly correlated to the number of quantized vortices that define its core) is not

high enough. I try this in a following section by increasing the number of quantized vortex rings per bundle.

5.4.2. Comparison with vortex collider configuration.

As I am dealing with vortex stretching in quantized vortex bundles, it is useful to compare the Hopf link configuration with the Vortex Collider.

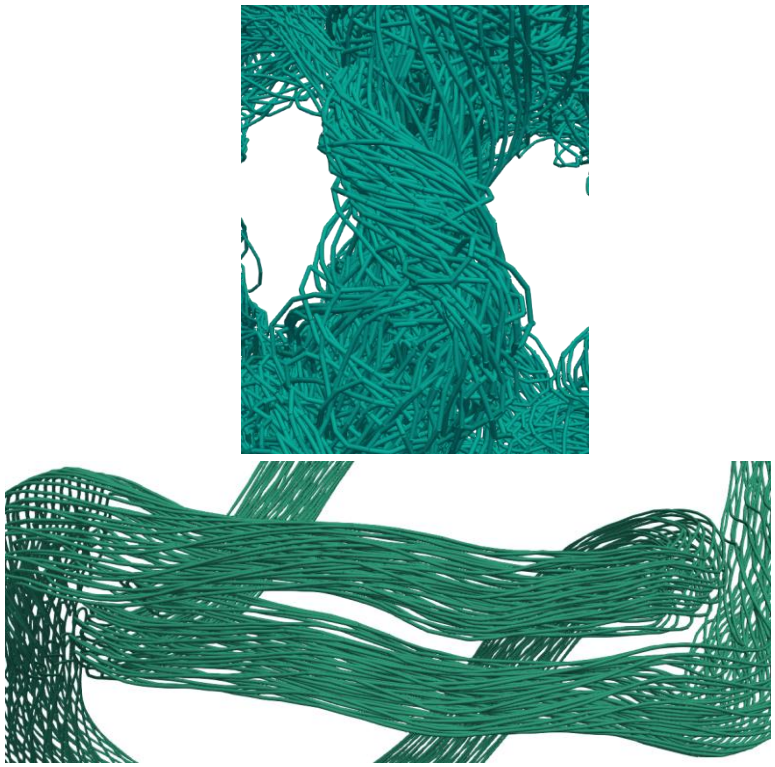

Fig. 64 - Tangle configuration for Vortex Collider at t= t=0.5942 (top) and Hopf-Link at t= 1.0397(bottom).

From Fig. 64, the vortex filaments that make up the bundles are much closer together in the vortex collider configuration (top) than the Hopf-Link configuration (bottom); this is even considering that the time vortex collider configuration snapshot is at $t = 0.5942$ and the Hopf link configuration snapshot is at $t = 1.0397$. As the bundles of these cases are identical in radius, bundle core thickness and strength (number of vortex rings defining the bundle), the only way they differ is in how the bundles are placed in 3D space. Comparing their energy spectra graph in Fig. 65 shows the differences between these two configurations. Firstly, the energy spectra of the Hopf link configuration is “shifted” towards smaller k, this is because the bundles are placed in such a way that the two most distant vortex points are further apart than in the vortex collider configuration. The greatest difference between the plots is the existence of a $k^{-5/3}$ regime in the vortex collider configuration, while there is none in the Hopf link; this together with Fig. 64 shows that the potential for vortex stretching of the new

vortex collider configuration is much greater than that of the Hopf link configuration, even though both bundle configurations have exactly the same circulation, ring diameter and bundle core thickness in the initial conditions.

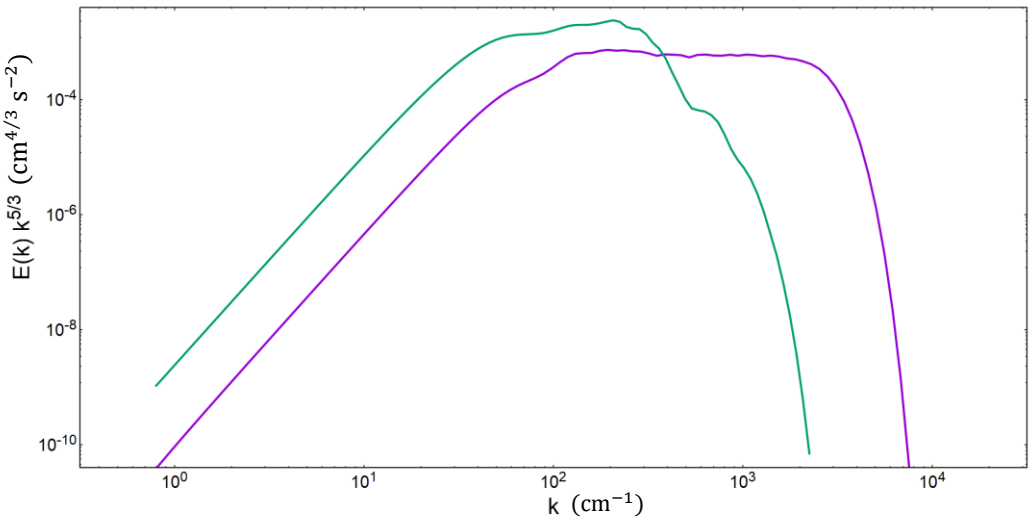

Fig. 65 - Energy spectra of the Vortex Collider configuration (purple) and the Hopf-Link configuration (green).

5.4.3. Secondary instabilities.

To better understand the secondary instabilities that appear on the "bridge", and their effect on the energy spectra, I ran one more calculation. This calculation uses the same parameters in terms of bundle diameter (0.083cm) and core thickness radius (0.0083cm) as well as discretisation length, the only difference is the strength of the bundles; I increased the number of quantized vortex rings per bundle from 49 to 81, this increases the total circulation per bundle to $0.080757\ cm^2s^{-1}$. In the Navier-Stokes vortex analogue, this would increase the Reynolds number, which would in turn increase the inertial effects in the flow. As the total circulation per bundle has changed in this configuration from the one explained in **section 5.4**, I recalculated the characteristic time and used it to scale all times in this sub-section. Therefore, the new characteristic time $t_c = \frac{0.083^2}{81*9.97E-4} = 0.0853s$ and all times mentioned in this chapter are in characteristic time, t_c, units. Given that the number of quantized vortices per bundle has increased but the bundle core thickness has been kept constant, I lowered the numerical core for the energy spectra to $\sigma_{diag} = 0.5\xi$ which equals $1.1857 \times 10^{-3}cm$.

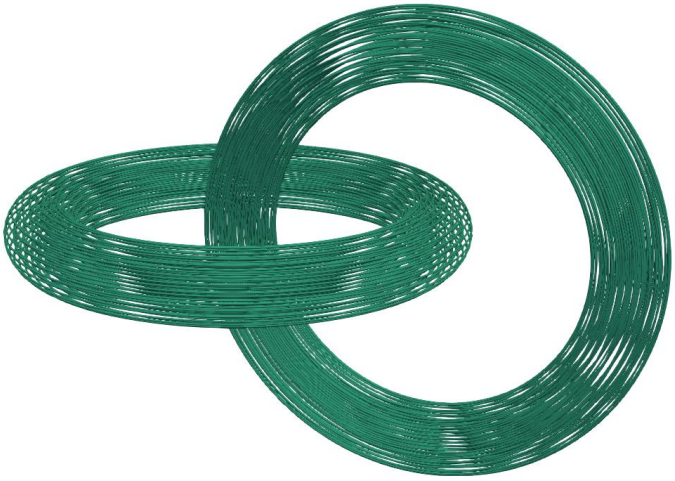

Fig. 66 - Quantized vortices forming 2 bundles in a Hopf-Link configuration. Each bundle is formed by 81 quantized vortex rings.

As the bundles move and the bridge is formed again, the tangle forms a bridge as seen in Fig. 67. The arrows represent the direction of vorticity, which shows that the parallel portion of the bundles are anti-parallel because the vorticity have opposite directions.

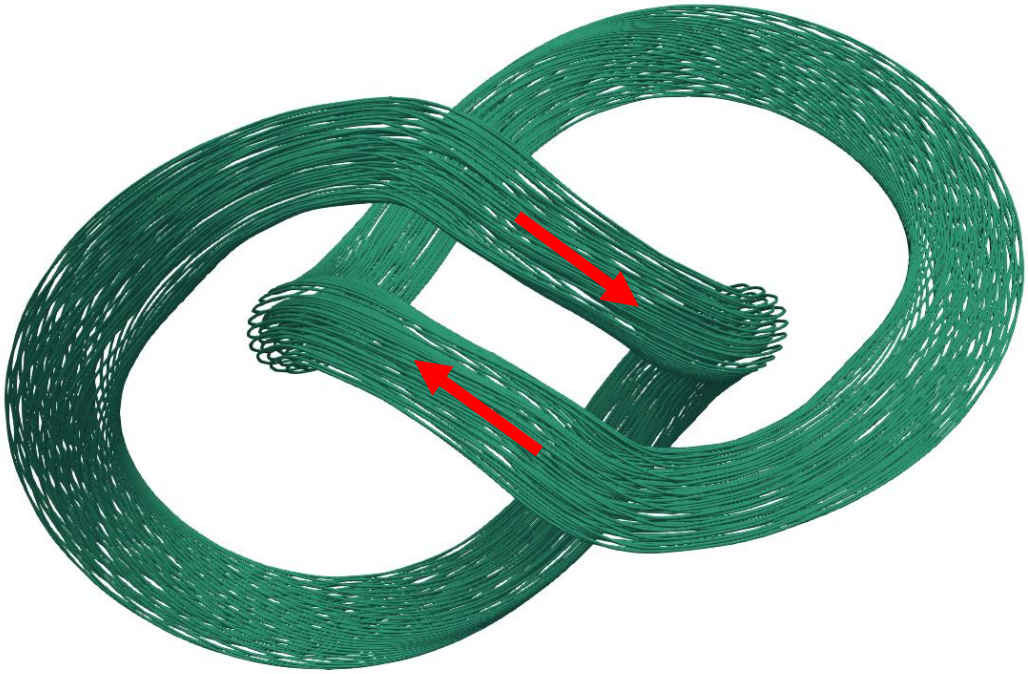

Fig. 67 - Vortex bundles in a Hopf-Link configuration at t=0.7605, showing a "bridge" formed by two anti-parallel bundle portions. The red arrows represent the direction of vorticity in each bundle portion.

As the bundles keep evolving, small sinusoidal instabilities appear on the bridge portion of the bundle and start growing in amplitude, these come from their counter-rotating nature

(anti-parallel); these instabilities were first discovered by Crow in [65] and further studied in an astrophysical manner by Wadas et al. in [67]. Chatelain et al. in [88] also present the Crow instability on a pair of vortices, my Hopf-Link configuration results also exhibit this instability, as seen in Fig. 68 and Fig. 69.

Fig. 68 - Crow instability generated and growing on the bridge portion of the Hopf-Link configuration at t=1.0647 (A), t=1.1408 (B), t=1.2168 (C) and t=1.3689 (D). At D, the instabilities have clumped up into a "secondary" bundle structure.

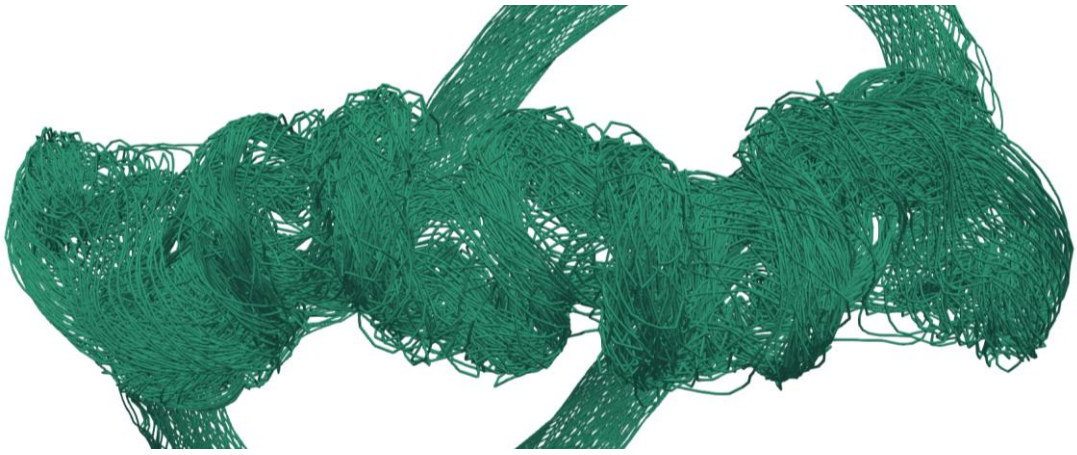

Fig. 69 – Zoomed in Hopf link configuration at t=1.3689 showing a sinusoidal instability that has grown enough to nearly wrap around the entire bundle core. This instability can be seen that has clumped up into a tight bundle.

Fig. 68 shows the progression of how the instability continuously grows and starts enveloping the original bundle structure. At t=1.3689, the instabilities have nearly wrapped around the entire bundle core and have grouped up in a tightly packed bundle. Now that I see that my configuration can capture the Crow instability, it would be interesting to see how this instability affects the energy spectra of the system, especially at the time where the Crow instability created secondary filamentary structures that are capable of their own self-vortex stretching.

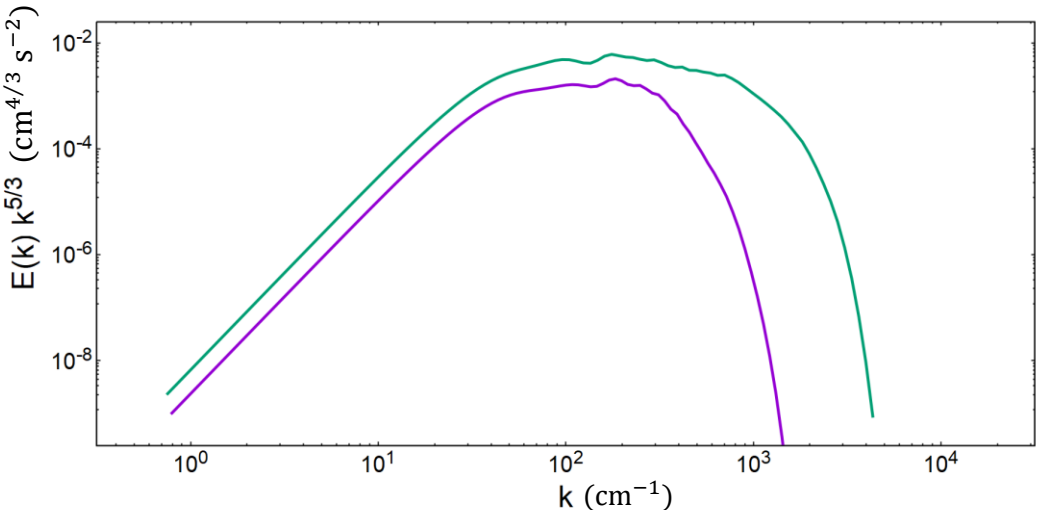

Fig. 70 - Energy spectra of the Hopf-link configuration at t=1.3689 for the 81-ring Hopf-link (green) showing a $k^{-5/3}$ regime in intermediate to large values of k arising from the tight clumping of Crow instability, and the energy spectra of the Hopf-link configuration at t=0.7426 for the 49-ring Hopf-link (purple) showing a very small $k^{-5/3}$ regime.

Fig. 70 shows a $k^{-5/3}$ regime for intermediate to large values of wavenumber k for the stronger, 81-ring case compared to the 49-ring case. This shows that even though the Hopf link configuration does not have as much of a vortex stretching potential as the vortex collider configuration, making the bundles stronger by giving them a higher number of quantized vortices (changing from 49 to 81 rings), results in the creation of tight secondary structures via the Crow instability. These instabilities then grow and group up into tight bundles giving way to the $k^{-5/3}$ regime present in Fig. 70; this results in the larger $k^{-5/3}$ regime that appears on the stronger (green plot showing 81-ring Hopf-link) configuration than on the weaker (purple plot showing 49 -ring Hopf-link) configuration. The generation of an instability and secondary vortex structures was also found by Mckeown et al. in [115] on the anti-parallel portions of two classical vortex rings that collide; in their case, the secondary vortex filaments fuel the cascade, while mine result in a $k^{-5/3}$ spectra and an energy transfer to high k.

Chatelain et al. in [93] also detect the formation of secondary vortex structures when colliding classical vortex rings when moving in opposite and same directions, and even using the same Hopf link configuration as me. They find that these secondary structures also transfer energy to small scales (high k).

An alternative to adding more rings to the bundles could be increasing the quantum of circulation of the individual quantized vortices to achieve a stronger total circulation of the bundle, and then try to detect the $k^{-5/3}$ regime. This way it would not require adding more discretisation points to the system but would require a larger numerical core for the vortex dynamics calculation.

6. Conclusions

In my thesis I wanted to understand different physics regarding several quantized vortex configurations: Individual quantized vortices and quantized vortex bundles, each of which had a different physics focus. For the case of the individual quantized vortices, the aim was to capture the Kelvin wave cascade generated after vortex reconnection and then the possible energy equilibration that comes from the continuous interaction between different sized Kelvin waves. The quantized vortex bundle configurations were focused on studying vortex stretching in Navier-Stokes turbulence via discretised filament models through energy spectra dynamics.

6.1. Individual Quantized Vortices Conclusions

The individual quantized vortices results were separated into two cases that were focused on the same physics (Kelvin wave cascade and long-term energy dynamics). The first configuration consisted of 4 quantized vortex rings placed on the opposite faces of an imaginary cube and they moved in such a way that they reconnected at 4 distinct points. After the first 4 reconnections, the regions of high curvature on the vortex tangle relaxed and sent Kelvin waves along the tangle; this relaxation generated the Kelvin wave cascade, this regime was well defined in time between the first 4 reconnections and the moment the fastest Kelvin waves start to interact/superpose. I found that the energy spectrum scaling associated with the Kelvin wave cascade is k^{-1}. After the Kelvin wave cascade regime ended, the Kelvin waves started to interact with other Kelvin waves of different sizes, this marked the beginning of the energy equilibration regime. The energy was transferred from large to small scales through the creation of Kelvin waves and their interaction (Kelvin-wave cascade). By allowing the system to evolve beyond the Kelvin wave cascade regime, I found evidence for the equilibration of the Kelvin waves energy spectrum. In particular, the spectrum became first flat and then with positive exponent $k^{0.6}$ when time t =82.82 small characteristic times (time taken for the fastest Kelvin waves to interact with each other); this could suggest that the spectra scaling will continue to grow until the energy is equilibrated when the scaling reaches k^2 (where the energy per unit area in Harmonic space is the same at all wavenumber values).

The same physics were checked using the fully developed turbulence configuration. When the vortices inevitably reconnected, the high curvature regions relaxed, creating Kelvin waves that travelled the tangle length. This generated a series of Kelvin waves in a similar manner

to the previously explained configuration; this time the vortices were much smaller, so the Kelvin wave cascade regime (prior to the interaction between Kelvin waves) was much shorter in time, also in this configuration there were many more reconnections, so it made it more difficult to isolate the Kelvin wave cascade. I found a k^{-1} energy spectra scaling corresponding to the Kelvin wave cascade. After the Kelvin waves started to interact with each other, the energy spectra started to show a slow transfer of energy from large to small scales; this resulted in the energy spectra shape changing from a k^{-1} to a flat scaling that is due to the presence of reconnection induced small rings. I found that the reconnections, by creating small rings and new Kelvin wave cascades, do not allow the system to equilibrate. A thought experiment calculation, based on disallowing reconnections, brought forward the equilibration process which changed the spectrum to flat and then with a positive exponent $k^{0.7}$ when time $t = 1.298$ large characteristic times (time taken for a vortex ring to propagate twice from one side to the opposite of the computational box).

6.2. Quantized Vortex Bundles Conclusions

The simulations involving quantized vortex bundles were separated into two different configurations, these were focused on understanding the dynamics of Navier-Stokes vortices and on studying vortex stretching via energy spectra dynamics. The first quantized vortex bundle configuration was a vortex collider, and it regarded 3 pairs of vortex bundles moving in opposite directions on a collision course, but their propagation axis was offset. The dynamics of this configuration distorted the vortex bundle before they started to reconnect; this distortion made the bundles experience vortex stretching and core torsion, which would be impossible if they were individual quantized vortices because of their fixed core size. The energy spectra throughout the vortex stretching and core torsion revealed firstly that there was an energy transfer from large to small scales without a $k^{-5/3}$ spectrum; later, with continued vortex stretching, a $k^{-5/3}$ spectrum was found. This shows that bundles of quantized vortices can in fact have a $k^{-5/3}$ scaling. I found that by kinematically stretching the bundles, the energy spectra presented a $k^{-5/3}$ regime in the absence of bundle core torsion and energy transfer. This suggests that solely kinematically stretching the bundles, and therefore concentrating vorticity at smaller scales, is sufficient for a $k^{-5/3}$ law to appear on the energy spectra. To further prove this, instead of kinematically stretching the vortex bundles, I reduced the bundle core size without increasing the bundle size (not maintaining the initial bundle core volume), this would also result in a concentration of vorticity at smaller

scales. The energy spectra of this configuration also revealed a $k^{-5/3}$ regime that appeared due to the concentration of vorticity at smaller scales, without any bundle core torsion or energy transfer.

The second quantized vortex bundle configuration consisted of two bundles forming a Hopf link. The bundle cores experienced Crow instability, which distorted them while forming an anti-parallel bridge; this was not enough to stretch the bundle cores and concentrate vorticity at smaller scales, so the spectra at this stage did not have a $k^{-5/3}$ scaling. Letting the vortices evolve freely resulted in the sinusoidal instability growing on the core. The Crow instability eventually completely engulfed the entirety of the two bundle cores that formed the bridge, and it formed secondary structures that were tightly packed, concentrating vorticity at smaller scales. Checking the energy spectra at this time showed that the appearance of the secondary structures, due to the sinusoidal instability, generated a $k^{-5/3}$ regime on the energy spectra.

The results regarding the quantized vortex bundles suggested that they can capture physics characteristic of Navier-Stokes fluid vortices, like vortex stretching or core torsion. More importantly, the quantized vortex bundle configurations suggested that the $k^{-5/3}$ scaling is due to the confinement of vorticity to small filamentary volumes, which can happen through vortex stretching, and that energy transfer or core torsion are not needed.

6.3. Future Work

The algorithm acceleration method that I used in my thesis, SIMD acceleration, gave me the possibility to reach longer simulation times to find new physics, like the appearance of secondary structures due to the growth of sinusoidal instabilities, but it would be interesting to research the effect of having stronger vortex in the Hopf link configuration on the appearance of secondary vortex structures. Improving the discretisation of the Navier-Stokes vortices increases the number vortex points to be calculated; this hinders the execution speed of the algorithms used since the calculations have a $O(N^2)$ complexity. Future work to build upon the physics on this thesis would start by implementing a more advanced acceleration method of the algorithms, this includes the implementation of a Fast Multipole Method (FMM). A correct implementation of this method would potentially improve the complexity of the computations from $O(N^2)$ to $O(N)$, and it would unlock the ability to feasibly compute the dynamics and energy spectra of extremely dense vortex tangles, it would also allow for longer times to see energy equilibration better.

7. References

1. Davidson P. Turbulence: An Introduction for Scientists and Engineers [Internet]. 2nd ed. Oxford University Press; 2015. Available from: https://academic.oup.com/book/27867

2. Bailly C, Comte-Bellot G. Turbulence. 2nd ed. Merzkirch W, Rockwell D, Tropea C, editors. Springer; 2015.

3. Moffatt HK, Kida S, Ohkitani K. Stretched vortices – the sinews of turbulence; large-Reynolds-number asymptotics. J Fluid Mech. 1994 May 10;266:371–371.

4. Chorin AJ. Vorticity and Turbulence [Internet]. New York, NY: Springer New York; 1994. 93–94 p. (Applied Mathematical Sciences; vol. 103). Available from: http://link.springer.com/10.1007/978-1-4419-8728-0

5. Wu J zhi, Ma HY, Zhou MD. Vorticity and Vortex Dynamics. 1st ed. Heidelberg: Springer Berlin Heidelberg; 2006.

6. Tennekes H, Lumley JL. A First Course in Turbulence. A First Course in Turbulence. Massachusetts: MIT Press; 1972.

7. Etna hoops it up. BBC News [Internet]. 2000 Mar 31; Available from: http://news.bbc.co.uk/1/hi/sci/tech/696953.stm

8. Mount Etna: Watch volcano blowing smoke rings in rare display. BBC Newsround [Internet]. 2024 Apr 7; Available from: https://www.bbc.co.uk/newsround/68755364

9. Watch: Mount Etna puff's "smoke rings" in rare display. BBC News [Internet]. 2024 Apr 6; Available from: https://www.bbc.co.uk/news/av/world-europe-68752290

10. Vortex rings made of water vapour rise from Italy's Mount Etna Volcano. ABC News [Internet]. 2024 Apr 8; Available from: https://www.abc.net.au/news/2024-04-08/mount-etna-volcanic-vortex-rings/103680958

11. Hanlon T. Incredible images show Mount Etna blowing vortex smoke rings in spectacular display. Mirror [Internet]. 2024 Apr 7; Available from: https://www.mirror.co.uk/news/world-news/incredible-images-show-mount-etna-32532390

12. Ashurst WT, Meiron DI. Numerical study of vortex reconnection. Phys Rev Lett [Internet]. 1987 Apr 20;58(16):1632–5. Available from: https://link.aps.org/doi/10.1103/PhysRevLett.58.1632

13. Kida S, Takaoka M. Reconnection of vortex tubes. Fluid Dyn Res [Internet]. 1988 Sep;3(1–4):257–61. Available from: https://iopscience.iop.org/article/10.1016/0169-5983(88)90075-5

14. Melander M V., Hussain F. Cross-linking of two antiparallel vortex tubes. Phys Fluids A. 1989;1(4):633–6.

15. Vinen WF. Decay of superfluid turbulence at a very low temperature: The radiation of sound from a Kelvin wave on a quantized vortex. Phys Rev B [Internet]. 2001 Sep;64(13):134520. Available from: https://link.aps.org/doi/10.1103/PhysRevB.64.134520

16. Walmsley PM, Golov AI, Hall HE, Levchenko AA, Vinen WF. Dissipation of Quantum Turbulence in the Zero Temperature Limit. Phys Rev Lett [Internet]. 2007 Dec;99(26):265302. Available from: https://link.aps.org/doi/10.1103/PhysRevLett.99.265302

17. Seyfert P, G. C. Superfluidity.pdf. Grenoble; 1989.

18. BAYM G, PETHICK C, PINES D. Superfluidity in Neutron Stars. Nature [Internet]. 1969 Nov;224(5220):673–4. Available from: http://adsabs.harvard.edu/abs/1969Natur.224..177K

19. Haskell B, Sedrakian A. Superfluidity and Superconductivity in Neutron Stars. Springer Nat. 2017 Feb 22;

20. Chamel N. Superfluidity and Superconductivity in Neutron Stars. Universe [Internet]. 2024 Feb 22;10(3):104. Available from: https://www.mdpi.com/2218-1997/10/3/104

21. Brink DM, Broglia RA. Nuclear Superfluidity [Internet]. Nuclear Superfluidity. Cambridge University Press; 2005. Available from: https://www.cambridge.org/core/product/identifier/9780511534911/type/book

22. Migdal AB, Larkin AI. Phenomenological approach to the theory of the nucleus. Nucl Phys. 1964;51(C):561–82.

23. ANDERSON PW, ITOH N. Pulsar glitches and restlessness as a hard superfluidity phenomenon. Nature [Internet]. 1975 Jul;256(5512):25–7. Available from: https://www.nature.com/articles/256025a0

24. Meissner W, Ochsenfeld R. Meissner and Ochsenfeld revisited. Eur J Phys. 1983;21:787–788.

25. Wyatt RE. Quantum Dynamics with Trajectories [Internet]. Antman SS, Marsden JE, Sirovich L, editors. Vol. 28, Interdisciplinary Applied Mathematics. Springer; 2005. 425 p. Available from: http://link.springer.com/10.1140/epjb/e2013-40570-8%5Cnhttp://arxiv.org/abs/1406.6401%5Cnhttp://arxiv.org/abs/1204.1475%5Cnhttp://link.aps.org/doi/10.1103/PhysRevLett.91.058302%5Cnhttp://arxiv.org/abs/nlin/0111059%5Cnhttp://link.aps.org/doi/10.1103/PhysRe

26. Ballentine LE. Quantum Mechanics: A Modern Development [Internet]. WORLD SCIENTIFIC; 2014. Available from: https://www.worldscientific.com/worldscibooks/10.1142/9038

27. Grössing G. On the thermodynamic origin of the quantum potential. Phys A Stat Mech its Appl. 2009;388(6):811–23.

28. Moffatt HK. A Brief Introduction to Vortex Dynamics and Turbulence. In 2011. p. 1–27.

29. Helmholtz H. LXIII. On Integrals of the hydrodynamical equations, which express vortex-motion. London, Edinburgh, Dublin Philos Mag J Sci [Internet]. 1867 Jan [cited 2023 May 8];33(226):485–512. Available from: https://www.tandfonline.com/action/journalInformation?journalCode=tphm15

30. Carbone M, Bragg AD. Is vortex stretching the main cause of the turbulent energy

cascade? J Fluid Mech [Internet]. 2019 [cited 2023 May 8];883:2. Available from: https://doi.org/10.1017/jfm.2019.923

31. Saffman PG. Vortex Dynamics [Internet]. Cambridge University Press; 1993 [cited 2021 May 8]. Available from: https://www.cambridge.org/core/product/identifier/9780511624063/type/book

32. Green SI. Fluid vortices. Fluid vortices. 1995.

33. Holton JR. An introduction to dynamic meteorology. 4th ed. Dmowska R, Holton JR, Rossby HT, editors. Elsevier. 2004. 1–532 p.

34. Gradshteyn I, Ryzhik I. Table of Integrals, Series and Products. [Internet]. 7th ed. Jeffrey A, Zwillinger D, editors. Mathematics of Computation. Elsevier; 2007. Available from: https://www.jstor.org/stable/2007757?origin=crossref

35. Thuneberg EV. Superfluidity. In: Encyclopedia of Condensed Matter Physics [Internet]. Elsevier; 2005 [cited 2021 Jul 2]. p. 128–33. Available from: https://linkinghub.elsevier.com/retrieve/pii/B0123694019007105

36. Zastenker GN, Salerno E, Buehler F, Bochsler P, Bassi M, Agafonov YN, et al. Isotopic composition and abundance of interstellar neutral helium based on direct measurements. Astrophysics. 2002;45(2):131–42.

37. Balibar S. The discovery of superfluidity. J Low Temp Phys [Internet]. 2007 Mar 13 [cited 2023 Jul 17];146(5–6):441–70. Available from: http://arxiv.org/abs/physics/0611119

38. Feynman RP. Chapter II Application of Quantum Mechanics to Liquid Helium. In: Progress in Low Temperature Physics [Internet]. 1955 [cited 2023 May 14]. p. 17–53. Available from: https://linkinghub.elsevier.com/retrieve/pii/S0079641708600773

39. Kivotides D, Vassilicos JC, Samuels DC, Barenghi CF. Kelvin Waves Cascade in Superfluid Turbulence. Phys Rev Lett [Internet]. 2001 Apr 2;86(14):3080–3. Available from: https://link.aps.org/doi/10.1103/PhysRevLett.86.3080

40. Kivotides D, Wilkin SL. Elementary vortex processes in thermal superfluid turbulence. J Low Temp Phys. 2009;156(3–6):163–81.

41. Kivotides D. Relaxation of superfluid vortex bundles via energy transfer to the normal fluid. Phys Rev B - Condens Matter Mater Phys. 2007;76(5).

42. Schwarz KW. Three-dimensional vortex dynamics in superfluid He4: Line-line and line-boundary interactions. Phys Rev B [Internet]. 1985 May 1 [cited 2023 May 13];31(9):5782–804. Available from: https://link.aps.org/doi/10.1103/PhysRevB.31.5782

43. Gudmundsson S. The Anatomy of the Wing. In: General Aviation Aircraft Design [Internet]. Elsevier; 2014. p. 299–399. Available from: https://linkinghub.elsevier.com/retrieve/pii/B9780323462945000285

44. Glegg S, Devenport W. The equations of fluid motion. In: Aeroacoustics of Low Mach Number Flows [Internet]. Elsevier; 2017. p. 9–48. Available from: https://linkinghub.elsevier.com/retrieve/pii/B9780128096512000023

45. Barenghi CF, Donnelly RJ. Vortex rings in classical and quantum systems. Fluid Dyn

Res [Internet]. 2009 Oct;41(5):051401. Available from: https://iopscience.iop.org/article/10.1088/0169-5983/41/5/051401

46. Nitsche M. Vortex Dynamics. In: Encyclopedia of Mathematical Physics [Internet]. Elsevier; 2006. p. 390–9. Available from: https://linkinghub.elsevier.com/retrieve/pii/B0125126662002546

47. SULLIVAN IS, NIEMELA JJ, HERSHBERGER RE, BOLSTER D, DONNELLY RJ. Dynamics of thin vortex rings. J Fluid Mech [Internet]. 2008 Aug 25 [cited 2021 May 10];609:319–47. Available from: https://www.cambridge.org/core/product/identifier/S0022112008002292/type/journal_article

48. Ogawa S ichiro, Tsubota M, Hattori Y. Study of Reconnection and Acoustic Emission of Quantized Vortices in Superfluid by the Numerical Analysis of the Gross–Pitaevskii Equation. J Phys Soc Japan [Internet]. 2002 Mar 15;71(3):813–21. Available from: http://arxiv.org/abs/cond-mat/0104255%0Ahttp://dx.doi.org/10.1143/JPSJ.71.813

49. Shariff K, Leonard A. Vortex rings. Annu Rev Fluid Mech. 1992;24(1):235–79.

50. Saffman PG. The Velocity of Viscous Vortex Rings. Stud Appl Math [Internet]. 1970 Dec 28;49(4):371–80. Available from: https://onlinelibrary.wiley.com/doi/10.1002/sapm1970494371

51. Kaplanski F, Rudi U. Dynamics of a Viscous Vortex Ring. Int J Fluid Mech Res [Internet]. 1999;26(5–6):618–30. Available from: http://www.dl.begellhouse.com/journals/71cb29ca5b40f8f8,5e12a65502d5a022,73e1111467f626e3.html

52. Danaila I, Kaplanski F, Sazhin SS. Viscous Vortex Rings [Internet]. Vortex Ring Models. Cham: Springer International Publishing; 2021. 51–86 p. Available from: https://doi.org/10.1007/978-3-030-68150-0_3

53. CATER JE, SORIA J, LIM TT. The interaction of the piston vortex with a piston-generated vortex ring. J Fluid Mech [Internet]. 2004 Jan 25;499:327–43. Available from: http://www.journals.cambridge.org/abstract_S0022112003006980

54. Weigand A, Gharib M. On the evolution of laminar vortex rings. Exp Fluids [Internet]. 1997 Apr;22(6):447–57. Available from: http://link.springer.com/10.1007/s003480050071

55. Van Dyke M. An Album of Fluid Motion.pdf. 4th ed. California: The Parabolic Press; 1982. 1–177 p.

56. Enciso A, Peralta-Salas D. Vortex reconnections in classical and quantum fluids. SeMA J [Internet]. 2022;79(1):127–37. Available from: https://doi.org/10.1007/s40324-021-00277-8

57. Kleckner D, Kauffman LH, Irvine WTM. How superfluid vortex knots untie. Nat Phys. 2016;12(7):650–5.

58. Bewley GP, Paoletti MS, Sreenivasan KR, Lathrop DP. Characterization of reconnecting vortices in superfluid helium. Proc Natl Acad Sci U S A. 2008;105(37):13707–10.

59. Nazarenko S, West R. Analytical solution for nonlinear Schrodinger vortex reconnection. J Low Temp Phys. 2003;132(July):1–10.

60. Villois A, Proment D, Krstulovic G. Universal and nonuniversal aspects of vortex reconnections in superfluids. Phys Rev Fluids. 2017;2(4):1–17.

61. de Waele A, Aarts R. Route to vortex reconnection. Phys Rev Lett [Internet]. 1994 Jan 24;72(4):482–5. Available from: https://link.aps.org/doi/10.1103/PhysRevLett.72.482

62. Leadbeater M, Winiecki T, Samuels DC, Barenghi CF, Adams CS. Sound emission due to superfluid vortex reconnections. Phys Rev Lett. 2001;86(8):1410–3.

63. Zhu T, Evans ML, Brown RA, Walmsley PM, Golov AI. Interactions between unidirectional quantized vortex rings. Phys Rev Fluids [Internet]. 2016 Aug 8;1(4):044502. Available from: https://link.aps.org/doi/10.1103/PhysRevFluids.1.044502

64. Weißmann S, Pinkall U. Filament-based smoke with vortex shedding and variational reconnection. In: ACM SIGGRAPH 2010 papers [Internet]. New York, NY, USA: ACM; 2010. p. 1–12. Available from: https://dl.acm.org/doi/10.1145/1833349.1778852

65. Crow SC. Stability theory for a pair of trailing vortices. AIAA J. 1970;8(12):2172–9.

66. Leweke T, Williamson CHK. Experiments on long-wavelength instability and reconnection of a vortex pair. Phys Fluids [Internet]. 2011 Feb 1;23(2):1–15. Available from: https://pubs.aip.org/pof/article/23/2/024101/257154/Experiments-on-long-wavelength-instability-and

67. Wadas MJ, White WJ, LeFevre HJ, Kuranz CC, Towne A, Johnsen E. Hydrodynamic Mechanism for Clumping along the Equatorial Rings of SN1987A and Other Stars. Phys Rev Lett [Internet]. 2024 Mar 13;132(11):111201. Available from: https://doi.org/10.1103/PhysRevLett.132.111201

68. Zuccher S, Caliari M, Baggaley AW, Barenghi CF. Quantum vortex reconnections. Phys Fluids [Internet]. 2012 Dec 1;24(12). Available from: https://pubs.aip.org/pof/article/24/12/125108/257652/Quantum-vortex-reconnections

69. Simula TP. Crow instability in trapped Bose-Einstein condensates. Phys Rev A [Internet]. 2011 Aug 17;84(2):021603. Available from: https://link.aps.org/doi/10.1103/PhysRevA.84.021603

70. Thomson W. XXIV. Vibrations of a columnar vortex. London, Edinburgh, Dublin Philos Mag J Sci [Internet]. 1880 Sep 8;10(61):155–68. Available from: https://www.tandfonline.com/doi/full/10.1080/14786448008626912

71. Hall HE. An Experimental and theoretical study of torsional oscillations in uniformly rotating liquid helium II. Proc R Soc London Ser A Math Phys Sci [Internet]. 1958 Jul 8;245(1243):546–61. Available from: https://royalsocietypublishing.org/doi/10.1098/rspa.1958.0100

72. Svistunov B V. Superfluid turbulence in the low-temperature limit. Phys Rev B [Internet]. 1995 Aug 1;52(5):3647–53. Available from: https://link.aps.org/doi/10.1103/PhysRevB.52.3647

73. Samuels DC, Kivotides D. A Damping Length Scale for Superfluid Turbulence. Phys Rev Lett. 1999;83(25):5306–9.

74. Vinen WF, Tsubota M, Mitani A. Kelvin-Wave Cascade on a Vortex in Superfluid 4He at a Very Low Temperature. Phys Rev Lett [Internet]. 2003 Sep 25;91(13):135301. Available from: https://link.aps.org/doi/10.1103/PhysRevLett.91.135301

75. Paoletti MS, Lathrop DP. Quantum Turbulence. Annu Rev Condens Matter Phys [Internet]. 2011 Mar 1;2(1):213–34. Available from: https://www.annualreviews.org/doi/10.1146/annurev-conmatphys-062910-140533

76. Narita Y, Baumjohann W. Lessons on collisionless reconnection from quantum fluids. Front Phys [Internet]. 2014 Dec 15;2(December):1–11. Available from: http://journal.frontiersin.org/article/10.3389/fphy.2014.00076/abstract

77. Kivotides D, Leonard A. Physics of superfluid helium-4 vortex tangles in normal-fluid strain fields. Phys Rev Fluids [Internet]. 2021 Apr 21 [cited 2021 May 9];6(4):044702. Available from: https://link.aps.org/doi/10.1103/PhysRevFluids.6.044702

78. Winckelmans GS, Leonard A. Contributions to Vortex Particle Methods for the Computation of Three-Dimensional Incompressible Unsteady Flows. J Comput Phys [Internet]. 1993 Dec [cited 2022 May 20];109(2):247–73. Available from: https://linkinghub.elsevier.com/retrieve/pii/S0021999183712167

79. Baggaley AW, Barenghi CF, Shukurov A, Sergeev YA. Coherent vortex structures in quantum turbulence. EPL (Europhysics Lett [Internet]. 2012 Apr 1;98(2):26002. Available from: https://iopscience.iop.org/article/10.1209/0295-5075/98/26002

80. Rusaouen E, Rousset B, Roche PE. Detection of vortex coherent structures in superfluid turbulence. EPL (Europhysics Lett [Internet]. 2017 Apr 1;118(1):14005. Available from: https://iopscience.iop.org/article/10.1209/0295-5075/118/14005

81. Diribarne P, Bon Mardion M, Girard A, Moro JP, Rousset B, Chilla F, et al. Investigation of properties of superfluid He 4 turbulence using a hot-wire signal. Phys Rev Fluids. 2021;6(9):1–16.

82. Baggaley AW. The importance of vortex bundles in quantum turbulence at absolute zero. Phys Fluids. 2012;24(5).

83. Kozik E, Svistunov B. Kolmogorov and Kelvin-wave cascades of superfluid turbulence at T=0 : What lies between. Phys Rev B [Internet]. 2008 Feb 8;77(6):060502. Available from: https://link.aps.org/doi/10.1103/PhysRevB.77.060502

84. Kivotides D. Energy spectra of finite temperature superfluid helium-4 turbulence. Phys Fluids [Internet]. 2014;26(10). Available from: http://dx.doi.org/10.1063/1.4898666

85. Kivotides D. Coherent Structure Formation in Turbulent Thermal Superfluids. Phys Rev Lett [Internet]. 2006 May 3;96(17):175301. Available from: https://link.aps.org/doi/10.1103/PhysRevLett.96.175301

86. Kivotides D. Interactions between normal-fluid and superfluid vortex rings in helium-4. EPL (Europhysics Lett [Internet]. 2015 Nov 1;112(3):36005. Available from: https://iopscience.iop.org/article/10.1209/0295-5075/112/36005

87. Wacks DH, Baggaley AW, Barenghi CF. Coherent laminar and turbulent motion of toroidal vortex bundles. Phys Fluids [Internet]. 2014 Feb 1;26(2). Available from: https://pubs.aip.org/pof/article/26/2/027102/259293/Coherent-laminar-and-turbulent-motion-of-toroidal

88. Chatelain P, Curioni A, Bergdorf M, Rossinelli D, Andreoni W, Koumoutsakos P. Billion vortex particle direct numerical simulations of aircraft wakes. Comput Methods Appl Mech Eng [Internet]. 2008 Feb;197(13–16):1296–304. Available from: https://linkinghub.elsevier.com/retrieve/pii/S0045782507004574

89. Sbalzarini IF, Walther JH, Bergdorf M, Hieber SE, Kotsalis EM, Koumoutsakos P. PPM – A highly efficient parallel particle–mesh library for the simulation of continuum systems. J Comput Phys [Internet]. 2006 Jul;215(2):566–88. Available from: https://linkinghub.elsevier.com/retrieve/pii/S002199910500505X

90. Kivotides D, Leonard A. Quantized Turbulence Physics. Phys Rev Lett [Internet]. 2003 Jun 13;90(23):234503. Available from: https://link.aps.org/doi/10.1103/PhysRevLett.90.234503

91. Alamri SZ, Youd AJ, Barenghi CF. Reconnection of superfluid vortex bundles. Phys Rev Lett. 2008;101(21).

92. Tabak EG. Vortex stretching in incompressible and compressible fluids. Spring. 2002. 1–10 p.

93. Chatelain P, Kivotides D, Leonard A. Reconnection of Colliding Vortex Rings. Phys Rev Lett [Internet]. 2003 Feb;90(5):54501. Available from: https://link.aps.org/doi/10.1103/PhysRevLett.90.054501

94. Leonard A. Nonlocal theory of area-varying waves on axisymmetric vortex tubes. Phys Fluids [Internet]. 1994;6(2):765–77. Available from: https://doi.org/10.1063/1.868315

95. Roberts PH, Berloff NG. The Nonlinear Schrödinger Equation as a Model of Superfluidity. In: Quantized Vortex Dynamics and Superfluid Turbulence [Internet]. Berlin, Heidelberg: Springer Berlin Heidelberg; 2001. p. 235–57. Available from: http://link.springer.com/10.1007/3-540-45542-6_23

96. Barenghi CF. Introduction to Superfluid Vortices and Turbulence. In: Quantized Vortex Dynamics and Superfluid Turbulence [Internet]. Berlin, Heidelberg: Springer Berlin Heidelberg; 2001. p. 3–14. Available from: http://link.springer.com/10.1007/3-540-45542-6_1

97. Tsubota M, Araki T, Nemirovskii SK. Vortex Tangle Dynamics Without Mutual Friction in Superfluid 4He. In: Quantized Vortex Dynamics and Superfluid Turbulence [Internet]. Berlin, Heidelberg: Springer Berlin Heidelberg; 2001. p. 198–204. Available from: http://link.springer.com/10.1007/3-540-45542-6_18

98. Araki T, Tsubota M, Nemirovskii SK. Energy Spectrum of Superfluid Turbulence with No Normal-Fluid Component. Phys Rev Lett [Internet]. 2002 Sep 16;89(14):145301. Available from: https://link.aps.org/doi/10.1103/PhysRevLett.89.145301

99. Kivotides D, Leonard A. Helicity spectra and topological dynamics of vortex links at high Reynolds numbers. J Fluid Mech [Internet]. 2021 Mar 25;911:A25. Available

from:
https://www.cambridge.org/core/product/identifier/S0022112020010034/type/journal_article

100. Wang T, Yokota R, Barba L. ExaFMM: a high-performance fast multipole method library with C++ and Python interfaces. J Open Source Softw [Internet]. 2021 May 30 [cited 2023 Aug 1];6(61):3145. Available from: https://joss.theoj.org/papers/10.21105/joss.03145

101. Andrews LC. Special Functions of Mathematics for Engineers [Internet]. Special Functions of Mathematics for Engineers. 1000 20th Street, Bellingham, WA 98227-0010 USA: SPIE; 1997 [cited 2023 Jul 13]. Available from: http://ebooks.spiedigitallibrary.org/book.aspx?doi=10.1117/3.270709

102. Donnelly RJ. Quantized Vortices and Turbulence in Helium II. Annu Rev Fluid Mech [Internet]. 1993 Jan;25(1):325–71. Available from: https://www.annualreviews.org/doi/10.1146/annurev.fl.25.010193.001545

103. Tapp K. Differential geometry of curves and surfaces [Internet]. Springer. Springer; 2016. 42 p. Available from: https://www.cambridge.org/core/product/identifier/CBO9781139523967A025/type/book_part

104. Zheng L, Zhang X. Numerical Methods. In: Modeling and Analysis of Modern Fluid Problems [Internet]. Academic Press; 2017 [cited 2023 Jul 23]. p. 361–455. Available from: https://linkinghub.elsevier.com/retrieve/pii/B9780128117538000086

105. Hairer E (Ernst), Lubich C, Roche M. The numerical solution of differential-algebraic systems by Runge-Kutta methods [Internet]. 1989. 139 p. Available from: https://link.springer.com/book/10.1007/BFb0093947

106. Wray AA. Minimal storage time-advancement schemes for spectral methods [Internet]. 1991. Available from: https://www.researchgate.net/publication/246830945_Minimal_storage_time-advancement_schemes_for_spectral_methods

107. Orlandi P. Fluid flow phenomena: A numerical toolkit [Internet]. Orlandi P, editor. Fluid Mechanics and its Applications. Rome: Springer; 2000. 1–369 p. (Fluid Mechanics and Its Applications; vol. 55). Available from: http://link.springer.com/10.1007/978-94-011-4281-6

108. Souza P, Borges L, Andreolli C, Thierry P. Portable Explicit Vectorization Intrinsics. In: High Performance Parallelism Pearls: Multicore and Many-core Programming Approaches. 2015. p. 463–85.

109. Cardoso JMP, Coutinho JGF, Diniz PC. High-performance embedded computing. In: Embedded Computing for High Performance [Internet]. 2017 [cited 2023 Aug 17]. p. 17–56. Available from: http://dx.doi.org/10.1016/B978-0-12-804189-5.00002-8

110. Martinsson PG. Fast Multipole Methods. In: Engquist B, editor. Encyclopedia of Applied and Computational Mathematics [Internet]. Berlin, Heidelberg: Springer Berlin Heidelberg; 2015. p. 498–508. Available from: https://link.springer.com/10.1007/978-3-540-70529-1

111. Araki T, Tsubota M. Cascade Process of Vortex Tangle Dynamics in Superfluid 4He without Mutual Friction. J Low Temp Phys. 2000;121(5–6):405–10.

112. Tsinober A. 4.2. Kinematic/Lagrangian chaos/advection. In: Moreau R, MADYLAM, editors. An Informal Introduction to Turbulence [Internet]. 2nd ed. Dordrecht: Springer Netherlands; 2009. p. 85–9. (Fluid Mechanics and Its Applications; vol. 92). Available from: http://link.springer.com/10.1007/978-90-481-3174-7

113. Nemirovskii SK. Energy spectrum of the quantum vortices configurations. Low Temp Phys [Internet]. 2015 Jun 1;41(6):478–83. Available from: http://dx.doi.org/10.1063/1.4922103

114. Kerr RM. Velocity and scaling of collapsing Euler vortices. Phys Fluids [Internet]. 2005 Jul 1;17(7):1–11. Available from: https://pubs.aip.org/pof/article/17/7/075103/908128/Velocity-and-scaling-of-collapsing-Euler-vortices

115. McKeown R, Ostilla-Mónico R, Pumir A, Brenner MP, Rubinstein SM. Cascade leading to the emergence of small structures in vortex ring collisions. Phys Rev Fluids [Internet]. 2018 Dec 17;3(12):124702. Available from: https://link.aps.org/doi/10.1103/PhysRevFluids.3.124702